

Ansatz-Independent Variational Quantum Classifier

Hideyuki Miyahara^{1,*} and Vwani Roychowdhury^{1,†}

¹*Department of Electrical and Computer Engineering, Samueli School of Engineering,
University of California, Los Angeles, California 90095*

(Dated: February 4, 2021)

The paradigm of variational quantum classifiers (VQCs) encodes *classical information* as quantum states, followed by quantum processing and then measurements to generate classical predictions. VQCs are promising candidates for efficient utilization of a near-term quantum device: classifiers involving M -dimensional datasets can be implemented with only $\lceil \log_2 M \rceil$ qubits by using an amplitude encoding. A general framework for designing and training VQCs, however, has not been proposed, and a fundamental understanding of its power and analytical relationships with classical classifiers are not well understood. An encouraging specific embodiment of VQCs, quantum circuit learning (QCL), utilizes an ansatz: it expresses the quantum evolution operator as a circuit with a predetermined topology and parametrized gates; training involves learning the gate parameters through optimization. In this letter, we first address the open questions about VQCs and then show that they, including QCL, fit inside the well-known kernel method. Based on such correspondence, we devise a design framework of efficient ansatz-independent VQCs, which we call the unitary kernel method (UKM): it directly optimizes the unitary evolution operator in a VQC. Thus, we show that the performance of QCL is bounded from above by the UKM. Next, we propose a variational circuit realization (VCR) for designing efficient quantum circuits for a given unitary operator. By combining the UKM with the VCR, we establish an efficient framework for constructing high-performing circuits. We finally benchmark the relatively superior performance of the UKM and the VCR via extensive numerical simulations on multiple datasets.

Introduction.— Since the discovery of Shor’s algorithm [1], much effort has been devoted to the development of quantum algorithms and quantum computers [2]. To exploit a near-term quantum device, several variational quantum algorithms [3] have been proposed, including the quantum approximate optimization algorithm [4] and the variational quantum eigensolver [5]. Then, quantum circuit learning (QCL) was proposed in Refs. [6, 7] and is now considered to be a promising candidate to utilize a near-term quantum device efficiently for application. QCL itself, however, is a special case of a larger set of hybrid quantum-classical classifiers – a class that we refer to as variational quantum classifiers (VQCs) – since it assumes an ansatz, where the circuit topology is fixed and only the gates are parameterized; See Fig. 1. Thus, several questions remain unanswered, including (i) can one get better performance than QCL by systematically designing an ansatz-independent VQC, and (ii) given that a VQC and QCL perform end-to-end classical machine learning (ML) tasks, are they related to any well-known classical ML algorithms and if the classical counterparts can perform better.

In this letter, we first discuss the correspondence between a VQC and the well-known kernel method [8, 9]. Then we propose an ansatz-independent VQC, which we call the unitary kernel method (UKM). By using the UKM, we show that the performance of QCL is bounded from above by the UKM.

To effectively use the unitary operator obtained by the

UKM, we propose a unitary decomposition method to create a circuit geometry, which we call the variational circuit realization (VCR). By combining the UKM and the VCR, we can efficiently construct a circuit geometry that works well for classification problems.

Fig. 1 presents a schematic of a general VQC, introduces and compares QCL and the UKM and explains the role of the VCR.

Variational quantum classifier.— We first introduce an analytical formalism for a VQC. Suppose that we are given a n -qubit system and a classical dataset $\mathcal{D} := \{x_i, y_i\}_{i=1}^N$, where $x_i \in \mathbb{R}^M$ is a feature vector and $y_i \in \{1, -1\}$ is the corresponding label for $i = 1, 2, \dots, N$. In this letter, we consider the amplitude encoding [7]; thus we fix $n = \lceil \log_2 M \rceil$. As mentioned in the discussions, one can embed x_i into a higher dimensional vector $\phi(x_i) \in \mathbb{R}^L$ with $L = \mathcal{O}(M^c)$ and then use the rest of the framework; the number of qubits n will still be $\mathcal{O}(\log M)$, thus retaining any potential quantum advantage. Here, $\mathcal{O}(\cdot)$ is the big-O notation and c is a certain constant. In this letter, however, we stick to the amplitude encoding case. A schematic of a VQC with amplitude encoding of x_i ’s is shown in Fig. 1(a). Let us consider making a prediction on y_i by the following function:

$$f_{\text{pred}}(x_i; \hat{U}, \theta_b) := \sum_{j=1}^Q \xi_j \langle \hat{O}_j \rangle_{x_i, \hat{U}} + \theta_b, \quad (1)$$

where $|\psi^{\text{in}}(x_i)\rangle := \hat{S}(x_i)|\text{init}\rangle$, $|\psi^{\text{out}}(x_i; \hat{U})\rangle := \hat{U}|\psi^{\text{in}}(x_i)\rangle$, and $\langle \hat{O}_j \rangle_{x_i, \hat{U}} := \langle \psi^{\text{out}}(x_i; \hat{U}) | \hat{O}_j | \psi^{\text{out}}(x_i; \hat{U}) \rangle$. While $\{\xi_j\}_{j=1}^Q$ can also be learned and optimized, the convention in [6, 7] is to treat them a fixed parameter and θ_b is a bias term to be estimated.

* miyahara@g.ucla.edu, hmiyahara512@gmail.com

† vwani@g.ucla.edu

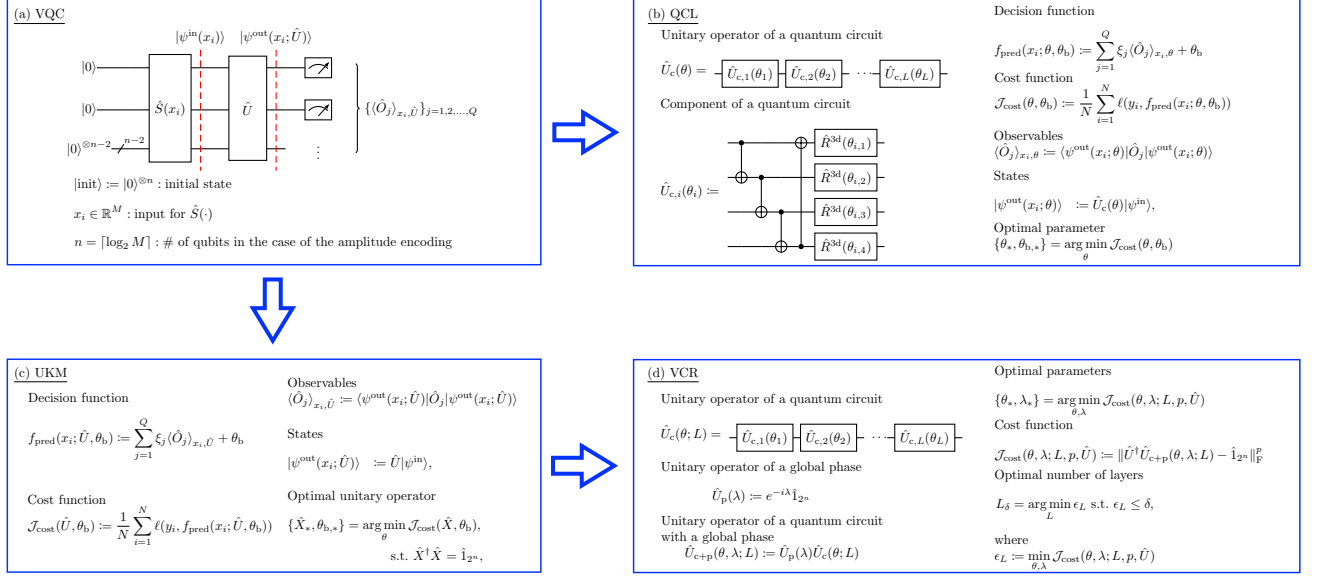


FIG. 1: Schematic of the algorithms discussed in this letter: (a) A general form of a hybrid quantum-classical classifier, which we refer to as a VQC, (b) QCL, (c) UKM, and (d) VCR. (a) In the architecture of a VQC, the initial state is $|\text{init}\rangle := |0\rangle^{\otimes n}$. We first encode a given classical vector x_i : $|\psi^{\text{in}}(x_i)\rangle := \hat{S}(x_i)|\text{init}\rangle$. As mentioned in the discussions, one can embed x_i into a higher dimensional vector $\phi(x_i) \in \mathbb{R}^L$ with $L = \mathcal{O}(M^c)$ and then use the rest of the framework; the number of qubits n will still be $\mathcal{O}(\log M)$, thus retaining any potential quantum advantage. Second, we apply \hat{U} : $|\psi^{\text{out}}(x_i; \hat{U})\rangle := \hat{U}|\psi^{\text{in}}(x_i)\rangle$. Third, we perform measurements with respect to $\{\hat{O}_j\}_{j=1,2,\dots,Q}$. Finally, we make a prediction on the label of x_i by using the outputs of the measurements. (b) In QCL, we assume a circuit geometry parameterized by θ for \hat{U} : $\hat{U}_c(\theta)$. In most cases, a circuit used for QCL is composed of single- and two-qubit operators and has a layered structure. A typical example is shown. (c) In the UKM, we directly optimize \hat{U} . (d) In the VCR, we decompose a unitary operator into a quantum circuit by assuming a layered structure for a quantum circuit. For a circuit realization, a simpler circuit is preferable; so, we explicitly denote the number of layers L .

In a VQC, we estimate \hat{U} and θ_b in Eq. (1) imposing the unitarity constraint on \hat{U} as follows:

$$\begin{aligned} \{\hat{U}_*, \theta_{b,*}\} &= \arg \min_{\hat{U}, \theta_b} \mathcal{J}_{\text{cost}}(\hat{U}, \theta_b), \\ &\text{subject to } \hat{U}^\dagger \hat{U} = \hat{I}_{2^n}, \end{aligned} \quad (2)$$

where

$$\mathcal{J}_{\text{cost}}(\hat{U}, \theta_b) := \frac{1}{N} \sum_{i=1}^N \ell(y_i, f_{\text{pred}}(x_i; \hat{U}, \theta_b)). \quad (3)$$

Here, $\ell(\cdot, \cdot)$ is a loss function, such as the mean-squared error function or the hinge function [8, 9], and \hat{I}_n is the n -dimensional identity operator. As explained later, we consider a parameterized unitary operator and optimize it in QCL and we directly optimize the unitary operator in the UKM.

Correspondence between a VQC and the kernel method.— Next, we discuss the relationship between a VQC and the kernel method [8, 9]. Introducing $\psi_l^{\text{in}}(x_i) := \langle l | \psi^{\text{in}}(x_i) \rangle$, $O_j^{k,l} := \langle k | \hat{O}_j | l \rangle$, and $u_{k,l} := \langle k | \hat{U} | l \rangle$

for $k, l = 1, 2, \dots, 2^n$, $\langle \hat{O}_j \rangle_{x_i, \hat{U}}$ is rewritten as

$$\langle \hat{O}_j \rangle_{x_i, \hat{U}} = \sum_{\substack{k_1, k_2, \\ k_3, k_4}} [\psi_{k_1}^{\text{in}}(x_i)]^* u_{k_1, k_2}^* O_j^{k_2, k_3} u_{k_3, k_4} \psi_{k_4}^{\text{in}}(x_i). \quad (4)$$

Then, by using the penalty method [10, 11], we can rewrite a VQC as

$$\lim_{\lambda \rightarrow \infty} \min_{\{u_{k,l}\}_{k,l=1,2^n, \theta_b}} \mathcal{J}_{\text{pm}}(\{u_{k,l}\}_{k,l=1,2^n, \theta_b; \lambda}), \quad (5)$$

where

$$\begin{aligned} \mathcal{J}_{\text{pm}}(\{u_{k,l}\}_{k,l=1,2^n, \theta_b; \lambda}) &:= \frac{1}{N} \sum_{i=1}^N \ell \left(y_i, \sum_{j=1}^Q \xi_j \tilde{O}_j(\{u_{k,l}\}_{k,l=1,2^n} + \theta_b) \right) \\ &\quad + \frac{\lambda}{2} \sum_{k,l=1,2,\dots,2^n} [u_k^H u_l - \delta_{k,l}]^2, \end{aligned} \quad (6)$$

and we have denoted the right-hand side of Eq. (4) by $\tilde{O}_j(\{u_{k,l}\}_{k,l=1,2^n})$. Here, $u_k := [u_{1,k}, u_{2,k}, \dots, u_{2^n,k}]^H$ for $k = 1, 2, \dots, 2^n$ and $(\cdot)^H$ is the Hermitian conjugate.

Then, we turn our attention to the kernel method [8, 9]. In the conventional kernel method, we make a prediction

on y_i by

$$f_{\text{pred}}(x; v) := v^\top \phi(x), \quad (7)$$

where $\phi(\cdot) := [\phi_1(\cdot), \phi_2(\cdot), \dots]^\top$ and $v := [v_1, v_2, \dots]^\top$ are the vector of feature maps and a real vector, respectively. We minimize the following function to determine v :

$$\mathcal{J}_{\text{cost}}(v) := \frac{1}{N} \sum_{i=1}^N \ell(y_i, f_{\text{pred}}(x_i; v)) + \frac{\lambda}{2} \|v\|_{\text{F}}^2. \quad (8)$$

Here, the second term in the right-hand side of Eq. (8) is the regularization term and $\|\cdot\|_{\text{F}}$ is the Frobenius norm. To clarify the correspondence between a VQC and the kernel method, we consider a modified version of the kernel method; that is, let us consider the following functions as the classifier and the cost function, respectively:

$$f_{\text{pred}}(x; w) := \sum_{k,l} w_{k,l} \tilde{\phi}_k(x) \tilde{\phi}_l(x), \quad (9)$$

$$\mathcal{J}_{\text{cost}}(w) := \frac{1}{N} \sum_{i=1}^N \ell(y_i, f_{\text{pred}}(x_i; w)) + \frac{\lambda}{2} |w_{k,l}|^2, \quad (10)$$

where $\{w_{k,l}\}_{k,l}$ are complex variables. Comparing Eqs. (6) with $\theta_{\text{b}} = 0$ and (10), a VQC and the kernel method have the following relationships:

$$\psi_l^{\text{in}}(x_i) \Leftrightarrow \tilde{\phi}_l(x_i), \quad (11a)$$

$$\sum_j \sum_{k_1, k_2} \xi_j u_{k, k_1}^* O_j^{k_1, k_2} u_{k_2, l} \Leftrightarrow w_{k, l}. \quad (11b)$$

Eq. (11) provides us a clear relationship between a VQC and the kernel method [12] and implicitly states that a VQC is a subset of the kernel method. Furthermore, Eq. (11) motivates us to devise the UKM, which lies between a VQC and the kernel method.

Quantum circuit learning.— Here, we review QCL proposed in Refs. [6, 7] from the viewpoint of a VQC. The schematic of QCL is demonstrated in Fig. 1(b). In QCL, we assume a parameterized unitary operator $\hat{U}_c(\theta)$ as \hat{U} and optimize θ [13]. We then compute $|\psi^{\text{out}}(x_i; \theta)\rangle := \hat{U}_c(\theta)|\psi^{\text{in}}(x_i)\rangle$. Then, we make a prediction on x_i by

$$f_{\text{pred}}(x_i; \theta, \theta_{\text{b}}) := \sum_{j=1}^Q \xi_j \langle \hat{O}_j \rangle_{x_i, \theta} + \theta_{\text{b}}, \quad (12)$$

where $\langle \hat{O}_j \rangle_{x_i, \theta} := \langle \psi^{\text{out}}(x_i; \theta) | \hat{O}_j | \psi^{\text{out}}(x_i; \theta) \rangle$. Similarly to Eq. (1), $\{\xi_j\}_{j=1}^Q$ are fixed parameters and θ_{b} is a bias term to be estimated. The second step of QCL is to update θ and θ_{b} by

$$\{\theta_*, \theta_{\text{b},*}\} = \arg \min_{\theta, \theta_{\text{b}}} \mathcal{J}_{\text{cost}}(\theta, \theta_{\text{b}}), \quad (13)$$

where

$$\mathcal{J}_{\text{cost}}(\theta, \theta_{\text{b}}) := \frac{1}{N} \sum_{i=1}^N \ell(y_i, f_{\text{pred}}(x_i; \theta, \theta_{\text{b}})), \quad (14)$$

and $\ell(\cdot, \cdot)$ is a loss function [14]. For this purpose, we often use the Nelder-Mead method [15] and other sophisticated numerical methods [10, 11].

As mentioned above, QCL assumes a parameterized unitary operator $\hat{U}_c(\theta)$; thus, its performance heavily depends on the topology of $\hat{U}_c(\theta)$. An assumed circuit topology is also called an ansatz; thus we can say that QCL is an ansatz-dependent VQC. This fact strongly motivates us to devise an ansatz-independent VQC, that is, the UKM. Furthermore, Ref. [16] pointed out the difficulty of learning parameters of quantum circuits, which they call the barren plateaus problem. Then, a VQC that is free of the barren plateaus problem is of interest.

Method of splitting orthogonal constraints.— The UKM heavily relies on the method of splitting orthogonal constraints (SOC); then, we review the method of SOC [17]. The method of SOC is a method for solving an optimization problem under an orthogonal constraints:

$$\min_X \mathcal{J}_{\text{cost}}(X), \quad (15a)$$

$$\text{subject to } X^\top A X = I, \quad (15b)$$

where $A > O$. Here, I and O are the identity matrix and the zero matrix, respectively. By splitting the constraints, we first rewrite Eq. (15) as

$$\min_{X, P} \mathcal{J}_{\text{cost}}(X), \quad (16a)$$

$$\text{subject to } L X = P, \quad (16b)$$

$$P^\top P = I, \quad (16c)$$

where L is a matrix that satisfies

$$A = L^\top L. \quad (17)$$

Then we solve Eq. 16 by

$$\{X_k, P_k\} = \arg \min_{X, P} \mathcal{J}_{\text{SOC}}(X; P, D_{k-1}),$$

$$\text{subject to } P^\top P = I, \quad (18a)$$

$$D_k = D_{k-1} + L X_k - P_k, \quad (18b)$$

where

$$\mathcal{J}_{\text{SOC}}(X; P, D) := \mathcal{J}_{\text{cost}}(X) + \frac{r}{2} \|L X - P + D\|_{\text{F}}^2. \quad (19)$$

Here, r is a positive constant. The performance of the method of SOC depends on r ; thus, we need to find an appropriate value of r . In the derivation of Eq. (19), the idea of Bregman iterative regularization [18, 19] is used [20].

It is still difficult to perform the computation of Eq. (18a). By splitting it and using operator unitarization (OU), which is explained later, we then have the following formula:

$$X_k = \arg \min_X \mathcal{J}_{\text{SOC}}(X; P_{k-1}, D_{k-1}), \quad (20a)$$

$$P_k = \arg \min_P \frac{r}{2} \|P - (L X_k + D_{k-1})\|_{\text{F}}^2,$$

$$\text{subject to } P^\top P = I, \quad (20b)$$

$$D_k = D_{k-1} + LX_k - P_k. \quad (20c)$$

Eq. (20) is the final form of the method of SOC [21]. Note that in the original paper of the method of SOC [17], only real matrices are considered; however, in the UKM, we utilize its complex version. The complex version of the method of SOC follows directly by noting that the SVD is also applicable to a complex matrix and the product of unitary matrices leads to a unitary matrix. Furthermore, in the original version of the method of SOC, we optimize a real-valued function of a real matrix. To optimize a real-valued function of a complex matrix, we optimize the real and complex parts of the complex matrix independently [22].

Operator unitarization.— OU is used in the method of SOC and will be used to obtain a unitary operator from a non-unitary operator. We briefly explain OU here. Let us consider the following optimization problem:

$$\begin{aligned} \hat{P}_* &= \arg \min_{\hat{P}} \frac{1}{2} \|\hat{P} - \hat{Y}\|, \\ &\text{subject to } \hat{P}^\dagger \hat{P} = \hat{1}. \end{aligned} \quad (21)$$

The solution of Eq. (21) is given by [17]

$$\hat{P}_* = \hat{K}_1 \hat{K}_2^\dagger, \quad (22)$$

where \hat{K}_1 and \hat{K}_2^\dagger are unitary operators that satisfy

$$\hat{Y} = \hat{K}_1 \hat{\Sigma} \hat{K}_2^\dagger, \quad (23)$$

and $\hat{\Sigma}$ is a diagonal operator in the sense that $\{\langle i | \hat{\Sigma} | i \rangle\}_i$ are the singular values of \hat{Y} and $\langle i | \hat{\Sigma} | j \rangle = 0$ for $i \neq j$. In this letter, we call Eq. (22) with Eq. (23) OU [23].

Unitary kernel method.— We here describe the UKM, which is one of the main algorithms in this letter. The schematic of the UKM is demonstrated in Fig. 1(c). In the UKM, we directly minimize Eq. (3). To this end, we employ the unitary version of the method of SOC [17]. Hereafter, we denote, by \hat{X} , an operator obtained via the method of SOC. We introduce \hat{P} and \hat{D} and iterate update equations for \hat{X} , \hat{P} , and \hat{D} until convergence. Hereafter, we denote, by \hat{X}_k , \hat{P}_k , \hat{D}_k , and $\theta_{b,k}$, \hat{X} , \hat{P} , \hat{D} , and θ_b at the k -th iteration, respectively. At the first step of the k -th iteration, we compute \hat{X}_k and $\theta_{b,k}$ by

$$\begin{aligned} &\{\hat{X}_k, \theta_{b,k}\} \\ &= \arg \min_{\hat{X}, \theta_b} \left[\mathcal{J}_{\text{cost}}(\hat{X}, \theta_b) + \frac{r}{2} \|\hat{X} - \hat{P}_{k-1} + \hat{D}_{k-1}\|_F^2 \right]. \end{aligned} \quad (24)$$

Next, we compute \hat{P}_k by

$$\hat{P}_k = \hat{K}_{1,k} \hat{K}_{2,k}^\dagger, \quad (25)$$

ALGORITHM 1: Unitary kernel method (UKM)

- 1: set \hat{P}_0 and \hat{D}_0
 - 2: **for** $k = 1, 2, \dots, K$ **do**
 - 3: compute \hat{X}_k and $\theta_{b,k}$ by Eq. (24)
 - 4: compute \hat{P}_k by Eq. (25)
 - 5: compute \hat{D}_k by Eq. (26)
 - 6: **end for**
-
-

where $\hat{K}_{1,k}$ and $\hat{K}_{2,k}^\dagger$ are unitary operators that satisfy $\hat{K}_{1,k} \hat{\Sigma}_k \hat{K}_{2,k}^\dagger = \hat{X}_k + \hat{D}_{k-1}$ and $\hat{\Sigma}_k$ is a diagonal operator. At the end of the k -th iteration, we compute

$$\hat{D}_k = \hat{D}_{k-1} + \hat{X}_k - \hat{P}_k. \quad (26)$$

We repeat the above equations, Eq. (24), (25), and (26), until convergence. We call this method the UKM. In Algo. 1, the UKM is summarized [24].

It is clear from the formulation of SOC that \hat{X} does not strictly satisfy the unitarity constraint; instead, \hat{P} and OU of \hat{X} does. Thus, using the optimal value of \hat{X} obtained from UKM leads to a classical classifier (it cannot be implemented using a quantum circuit), and will in general have higher performance than the unitary transformations given by \hat{P} and OU of \hat{X} that approximate \hat{X} . Thus, we compute the success rates for the training and test datasets by using all the versions: \hat{X} , \hat{P} , and OU of \hat{X} [25], of which only \hat{P} and OU of \hat{X} correspond to VQC.

Variational circuit realization.— There are a few studies on decomposing unitary operators into quantum circuits [26–28], including Knill’s decomposition and the quantum Shannon decomposition (QSD). In these methods, however, the number of CNOT gates scales exponentially in the number of qubits n .

Here we propose an alternate method: the target circuit is comprised of L layers of a parameterized sub-circuit with parameterized gates and a fixed topology; similar to the ansatz used in QCL. We then solve for the minimum number of layers L , such that the optimized circuit approximates the given unitary operator with a specified precision of δ . We refer to this circuit methodology as the Variational Circuit Realization technique. The schematic of the VCR is demonstrated in Fig. 1(d). Let \hat{U} and $\hat{U}_c(\theta; L)$ be a target unitary operator and a unitary operator realized by a quantum circuit that has L layers, respectively. Typically, the target unitary operator is obtained by the UKM discussed above. Furthermore, we define the global phase unitary operator $\hat{\Phi}_{2^n}(\lambda) := e^{-i\lambda} \hat{1}_{2^n}$. When \hat{U} and $\hat{U}_{c+p}(\theta, \lambda; L) := \hat{\Phi}_{2^n}(\lambda) \hat{U}_c(\theta; L)$ are identical, we have

$$\hat{U}^\dagger \hat{U}_{c+p}(\theta, \lambda; L) = \hat{1}_{2^n}. \quad (27)$$

Then, we can estimate θ , for any $p > 0$, by

$$\{\theta_*, \lambda_*\} = \arg \min_{\theta, \lambda} \mathcal{J}_{\text{cost}}(\theta, \lambda; L, p, \hat{U}), \quad (28)$$

where

$$\mathcal{J}_{\text{cost}}(\theta, \lambda; L, p, \hat{U}) := \|\hat{U}^\dagger \hat{U}_{c+p}(\theta, \lambda; L) - \hat{1}_{2^n}\|_{\mathbb{F}}^p. \quad (29)$$

We call this method the VCR.

In a circuit realization, the complexity of a circuit is of great interest. In this letter, we assume a layered structure for a quantum circuit. Thus, given an error threshold δ , it is convenient to define L_δ :

$$L_\delta := \arg \min_L \epsilon_L, \quad (30)$$

subject to $\epsilon_L \leq \delta$,

where

$$\epsilon_L := \min_{\theta, \lambda} \mathcal{J}_{\text{cost}}(\theta, \lambda; L, p, \hat{U}). \quad (31)$$

Numerical simulation of the UKM.— We first show the numerical results of QCL and the UKM for the cancer dataset (0 or 1) [29] in the UCI repository [30]. The results for multiple datasets with different dimensions, M , are presented in Table I

Before getting into the numerical results, we state the numerical setup [31]. For the UKM, we put $r = 0.010$ and set $K = 30$ in Algo. 1. Furthermore, we use the conjugate gradient (CG) method to find the solution of Eq. (24) and run the CG iteration 10 times [32]. The UKM is closed in real matrices; then we consider the real and complex cases. For QCL, we consider four types of quantum circuits: the CNOT-based circuit, the CRot-based circuit, the 1-dimensional (1d) Heisenberg circuit, and the fully-connected (FC) Heisenberg circuit [33], and run iterations 300 times. To accelerate QCL, we utilize the stochastic gradient descent method [9]. In both cases, we use the squared error function $\ell_{\text{SE}}(a, b) := \frac{1}{2}|a - b|^2$ for $\ell(\cdot, \cdot)$ in Eqs. (3) and (14), and set $Q = 1$ and $\xi_1 = 1$ in Eqs. (1) and (12). Furthermore, we consider two cases with the bias term and without the bias term in Eqs. (1) and (12).

We summarize the results of 5-fold cross-validation (CV) with 5 different random seeds of QCL and the UKM in Tables II and III, respectively. For each method, we select the best model for the training dataset over iterations to compute the performance. In Fig. 2, we plot the data shown in Tables II and III. As shown in Fig. 2, the performance of the UKM is better than that of QCL in several numerical setups.

Given our analytical results showing that a kernel method is a super-set of VQC, we next present the performance of the kernel method [34]. We summarize the results of 5-fold CV with 5 different random seeds of the kernel method in Table IV. We set $\lambda = 10^{-1}$, which is the coefficient of the regularization term, and consider the linear functions and the second-order polynomial functions for a feature map with and without normalization.

We then explore the performance dependence of QCL on the number of layers L . The result is shown in Fig. 3.

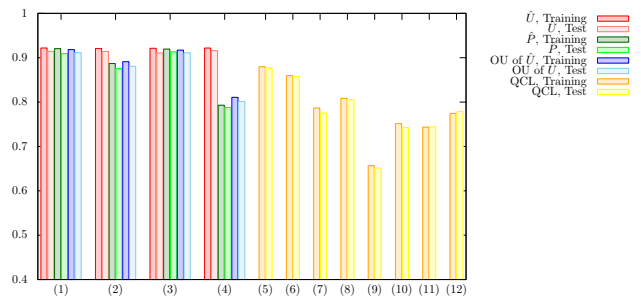


FIG. 2: Results of 5-fold CV with 5 different random seeds for the cancer dataset (0 or 1). For the UKM, we put $r = 0.010$ and $K = 30$. We repeat the CG iterations for Eq. (24) 10 times in each step of the method of SOC. For QCL, the number of layers L is 5 and the number of iterations is 300. The numerical settings are as follows: (1) complex matrix without bias, (2) complex matrix with bias, (3) real matrices without the bias term, (4) real matrices with the bias term, (5) CNOT-based circuit without the bias term, (6) CNOT-based circuit with the bias term, (7) CRot-based circuit without the bias term, (8) CRot-based circuit with the bias term, (9) 1d Heisenberg circuit without the bias term, (10) 1d Heisenberg circuit with the bias term, (11) FC Heisenberg circuit without the bias term, and (12) FC Heisenberg circuit with the bias term.

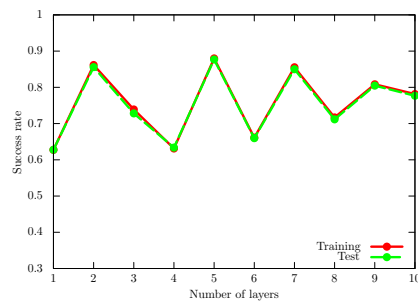


FIG. 3: Performance dependence of QCL on the number of layers L for the cancer dataset (0 or 1). We use the CNOT-based circuit geometry and set $\theta_{\text{bias}} = 0$. We iterate the computation 300 times.

One would naturally expect that increasing the number of layers L leads to better performance. In general, a circuit with $L + 1$ layers can clearly do at least as well as the circuit with L layers: pick the same parameters for the first L layers, and choose parameters to create an identity operator with the last layer. But Fig. 3 shows it is not the case. Rather, the test performance gets worse when we increase the number of layers L . This variability is potentially related to the structure of the cost function landscape: as the number of parameters is increased by adding an extra layer, there are potentially more local minima or the landscape develops what has been referred to as a “barren plateau” in Ref. [16].

We also see the performance dependence of the UKM on r , which is the coefficient of the second term in the right-hand side of Eq. (24). The result is shown in Fig. 4.

Dataset	N	M	n	- Quantum -			- Classical -	
				UKM (\hat{P})	UKM (OU of \hat{X})	QCL	UKM (\hat{X})	Kernel method
Iris (0 or 1)	100	4	2	1.0000/ 1.0000	1.0000/ 1.0000	1.0000/ 1.0000	1.0000/1.0000	1.0000/1.0000
Iris (0 or non-0)	150	4	2	1.0000/0.9987	1.0000/ 1.0000	1.0000/ 1.0000	1.0000/1.0000	1.0000/1.0000
Iris (1 or non-1)	150	4	2	0.7880/0.7789	0.7953/ 0.7994	0.6801/0.5872	0.9781/0.9618	0.9751/0.9666
Cancer (0 or 1)	569	30	5	0.9194/ 0.9131	0.9184/0.9115	0.8797/0.8768	0.9218/0.9160	0.9618/0.9568
Sonar (0 or 1)	208	60	6	0.9159/ 0.7985	0.9175/0.7909	0.7455/0.6924	0.8903/0.7774	1.0000/0.8198
Wine (0 or non-0)	178	14	4	0.9200/ 0.9185	0.9212/0.9171	0.9155/0.9126	0.9364/0.9313	0.9987/0.9955
Semeion (0 or 1)	323	256	8	1.0000/0.9943	1.0000/ 0.9945	0.9210/0.9099	1.0000/0.9957	1.0000/1.0000
Semeion (0 or non-0)	1593	256	8	0.9988/0.9949	0.9990/ 0.9953	0.8989/0.8982	0.9969/0.9925	1.0000/0.9955
MNIST256 (0 or 1)	569	256	8	0.9991/ 0.9969	1.0000/0.9951	0.9511/0.9459	0.9985/0.9966	1.0000/1.0000
MNIST256 (0 or non-0)	2766	256	8	0.9922/0.9871	0.9927/ 0.9889	0.9053/0.9050	0.9894/0.9859	0.9992/0.9953

TABLE I: Results of 5-fold CV with 5 different random seeds of the UKM (\hat{X} , \hat{P} , and OU of \hat{X}), QCL, and the kernel method for all the datasets. The cells are of the format “training performance/test performance.” We choose the model that shows the best test performance for each algorithm. For the UKM, we consider the complex and real cases with and without the bias term. We set $r = 0.010$. For QCL, we consider the CNOT-based, CRot-based, 1d-Heisenberg, and FC-Heisenberg circuits with and without the bias term for the iris, cancer, sonar, and wine datasets, and the CNOT-based and CRot-based circuits with and without bias term for the semeion and MNIST256 datasets. We set the number of layers L to 5. For the kernel method, we consider the linear functions and the second-order polynomial functions with and without the bias term for $\lambda = 10^{-2}, 10^{-1}, 1$. The values of the best VQC for each dataset are printed in bold. The numbers of data points N and dimensions M of the datasets are shown. The number of qubits n required for the amplitude encoding is also shown. Note that $n = \lceil \log_2 M \rceil$.

Algo.	Condition	Training	Test
QCL	CNOT-based, w/o bias	0.8797	0.8768
QCL	CNOT-based, w/ bias	0.8597	0.8577
QCL	CRot-based, w/o bias	0.7866	0.7752
QCL	CRot-based, w/ bias	0.8085	0.8052
QCL	1d Heisenberg, w/o bias	0.6568	0.6512
QCL	1d Heisenberg, w/ bias	0.7515	0.7427
QCL	FC Heisenberg, w/o bias	0.7435	0.7444
QCL	FC Heisenberg, w/ bias	0.7744	0.7789

TABLE II: Results of 5-fold CV with 5 different random seeds for the cancer dataset (0 or 1). The number of layers L is 5 and the number of iterations is 300. As shown in Fig. 3, increasing the number of layers L does not lead to better performance, and can in fact decrease performance of QCL.

For small r , \hat{X} in the UKM deviates from unitary matrices and the performance gets better. On the other hand, for large r , \hat{X} in the UKM becomes closer to unitary matrices but the performance gets worse. Thus, we should choose an appropriate value of r .

In Fig. 5, we show the performance dependence of the kernel method on λ , which is the coefficient of the regularization term. Like r in the UKM, we also need to choose an appropriate λ to realize good performance.

In Table. I, we summarize the performance of the UKM, QCL, and the kernel method for all the datasets investigated in this study. We choose the model that shows the best test performance for each algorithm. For the UKM, we consider the complex and real cases with and without the bias term. We set $r = 0.010$. For QCL, we consider the CNOT-based, CRot-based, 1d-Heisenberg, and FC-Heisenberg circuits with and without the bias term for the iris, cancer, sonar, and wine

Algo.	Condition	Training	Test
UKM	\hat{X} , complex, w/o bias	0.9219	0.9143
UKM	\hat{P} , complex, w/o bias	0.9204	0.9093
UKM	OU of \hat{X} , complex, w/o bias	0.9184	0.9115
UKM	\hat{X} , complex, w/ bias	0.9207	0.9143
UKM	\hat{P} , complex, w/ bias	0.8870	0.8753
UKM	OU of \hat{X} , complex, w/ bias	0.8912	0.8805
UKM	\hat{X} , real, w/o bias	0.9213	0.9107
UKM	\hat{P} , real, w/o bias	0.9194	0.9131
UKM	OU of \hat{X} , real, w/o bias	0.9170	0.9112
UKM	\hat{X} , real, w/ bias	0.9218	0.9160
UKM	\hat{P} , real, w/ bias	0.7929	0.7879
UKM	OU of \hat{X} , real, w/ bias	0.8107	0.8014

TABLE III: Results of 5-fold cross-validation (CV) with 5 different random seeds for the cancer dataset (0 or 1). We set $r = 0.010$ and $K = 30$. We repeat the CG iterations for Eq. (24) 10 times in each step of the method of SOC. Due to the inherent formulation of SOC, \hat{X} does not strictly satisfy the unitarity condition; \hat{P} and OU of \hat{X} strictly satisfy the unitarity condition, yielding VQC. The overall higher performance of \hat{X} can be attributed to it being a classical classifier; a special case of a kernel method. Note, however, that the UKM models without bias yield better performance than the best QCL results, as shown in Table II

datasets, and the CNOT-based and CRot-based circuits with and without bias term for the semeion and MNIST256 datasets. We set the number of layers L to 5. For the kernel method, we consider the linear functions and the second-order polynomial functions with and without the bias term for $\lambda = 10^{-2}, 10^{-1}, 1$. The numerical results support the claim that the UKM lies between the kernel method and QCL. We also show the detailed

Algo.	Condition	Training	Test
Kernel method	Linear, w/o normalization	0.9623	0.9549
Kernel method	Linear, w/ normalization	0.9205	0.9176
Kernel method	Poly-2, w/o normalization	0.9936	0.9361
Kernel method	Poly-2, w/ normalization	0.9210	0.9195

TABLE IV: Results of 5-fold CV with 5 different random seeds of the kernel method for the cancer dataset (0 or 1). We set $\lambda = 10^{-1}$.

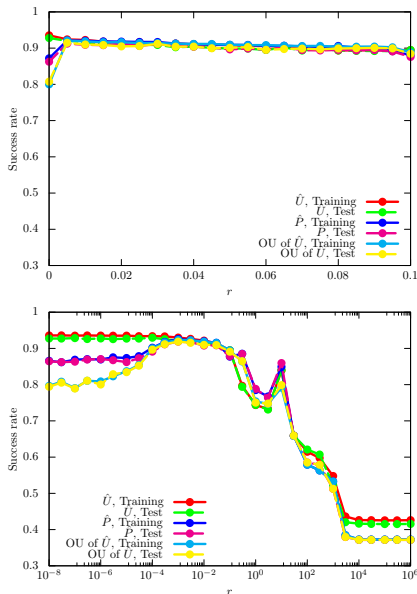


FIG. 4: Performance dependence of the UKM on r , which is the coefficient of the second term in the right-hand side of Eq. (24) for the cancer dataset (0 or 1). We use complex matrices and set $\theta_{\text{bias}} = 0$. We put $r = 0.010$ and $K = 30$. We repeat the CG iterations for Eq. (24) 10 times in each step of the method of SOC.

numerical results for all the datasets in the supplemental information (SI) [35]. The results shown in the SI are consistent with this letter. Finally, we note the difference between the squared error and hinge functions. *In this letter, we have used the squared error function; we show the results of the hinge function in the SI. The results are qualitatively same as obtained with the squared error function, and the statements about the relative performances of UKM, QCL, and Kernel methods do not change.*

Discussions on the UKM.— As shown in this letter, the performance of QCL is bounded from above by the UKM. One of the biggest reasons is a difference in the degrees of freedom in QCL and the UKM. In the UKM, we have $\mathcal{O}(M^2)$ parameters to estimate; on the other hand, the number of parameters in the QCL is $\mathcal{O}(L \ln M)$. This difference implies that a circuit ansatz introduces a strong bias in QCL, and may restrict the performance of QCL considerably. Thus, by designing the UKM, we can explore the ultimate power of QCL and at least, for the

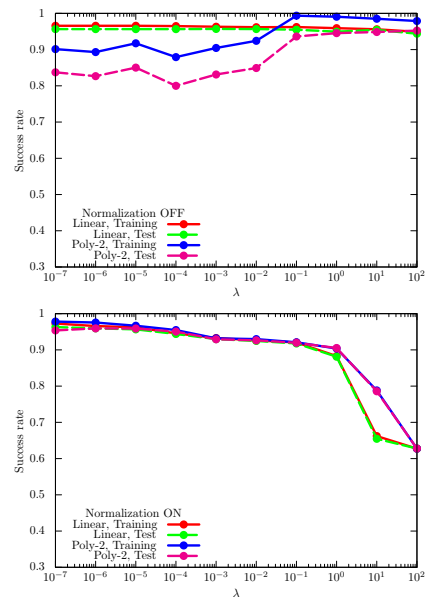


FIG. 5: Performance dependence of the kernel method on λ , which is the coefficient of the regularization term for the cancer dataset (0 or 1). For $\phi(\cdot)$, we use the linear functions and the second-degree polynomial functions with and without normalization. We use the squared error function.

case of a small number of qubits n , the numerical results in this letter show that the ultimate power of QCL is limited. However, by using a limited number of layers L , QCL can often get good performance, while requiring a fewer number of gate operations. Thus, if we can really develop a quantum computer with a sufficiently large number of qubits n , QCL may be useful for applications.

As noted earlier, we can also address the potential limitations of QCL from the viewpoint of optimization. Fig. 3 implies the difficulty of optimizing parameters in QCL. Otherwise, the success rates in Fig. 3 should be more smooth and monotonically increasing. This phenomenon may come from the barren plateaus problem [16]. On the other hand, the performance of the UKM is very high and close to that of the kernel method in 4; thus, we can say that the UKM does not suffer from a similar optimization problem.

We also note a practical difficulty in implementing QCL. If we can properly choose circuit geometry, the performance of QCL and the UKM should be the same or very close. But, in reality, there is a gap in the performance of QCL and the UKM; thus, it implies that choosing a good circuit geometry is difficult.

Numerical simulation of the VCR.— We then show numerical simulations on the VCR. For $\hat{U}_c(\theta)$, we use the CNOT-based circuit geometry. Furthermore, we use the BFGS method [11] to solve Eq. (28).

Let us consider the cancer dataset (0 or 1) and minimizing Eq. (29) with $p = 2$. As \hat{U} , we use the unitary operator that gives the success rate for the training dataset 0.7565 and that for the test dataset 0.8286. In Fig. 6, we

Algo.	Condition	Cost	Training	Test
Input	UKM, \hat{P} , real, w/o bias	—	0.9139	0.9483
VCR	# of layers: 10	1.9694	0.3929	0.2931
VCR	# of layers: 20	1.9734	0.6071	0.7069
VCR	# of layers: 30	1.3950	0.6071	0.7069
VCR	# of layers: 40	0.7777	0.6909	0.7586
VCR	# of layers: 50	0.4657	0.8499	0.9224
VCR	# of layers: 60	0.1877	0.9073	0.9483
VCR	# of layers: 70	0.0236	0.9073	0.9483
VCR	# of layers: 80	0.0000	0.9139	0.9483
VCR	# of layers: 90	0.0000	0.9139	0.9483
VCR	# of layers: 100	0.0000	0.9139	0.9483
UKM	\hat{P} , real, w/o bias	—	0.9194	0.9131
QCL	# of layers: 5	—	0.8798	0.8768
QCL	# of layers: 10	—	0.7814	0.7767

TABLE V: Performance of the VCR for the cancer dataset (0 or 1). We show the success rates for the training and test datasets and the value of the cost function for the VCR. The input for the VCR is \hat{P} created by the UKM under the condition of real matrices without the bias term with $r = 0.010$. For reference, we add the last three rows that show the results of 5-fold CV. The table shows that around 50 layers, by combining UKM with VCR one can get a better performance than that of QCL.

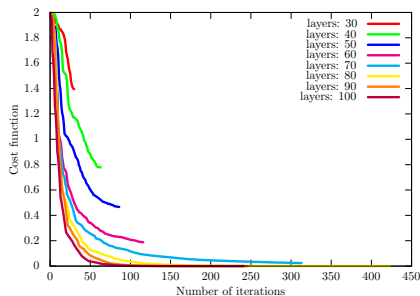


FIG. 6: Values of the cost function $J_{\text{cost}}(\theta, \lambda; L, 2, \hat{U})$, Eq. (29) with $p = 2$, for the cancer dataset (0 or 1). We set $L = 30, 40, 50, 60, 70, 80, 90, 100$.

show the values of the cost function in the right-hand side of Eq. (29) with different numbers of layers. In Table V, we summarize the performance of the input unitary operator, QCL, and the circuit geometry computed by the VCR.

Fig. 6 shows the values of the cost function, Eq. (29), over iterations with different number of layers L . Table V shows that $\hat{U}_c(\theta)$ gives high performance. We have $L_{0.001} = 80$.

Discussions on the VCR.— Recall that M and L are the dimension of the data points and the number of layers in an ansatz adopted in QCL, respectively. Note that we use the amplitude encoding in this letter. Then circuits in QCL have $\lceil \ln M \rceil$ qubits and have $\mathcal{O}(L \ln M)$ gates. The number of parameters to estimate is of the same order since we use the three-dimensional rotation gate as a parametrized gate. The UKM also has the same num-

ber of qubits $\lceil \ln M \rceil$; so it retains the qubit efficiency, but it optimizes over $\mathcal{O}(M^2)$ parameters. Moreover, circuits obtained by the combination of the UKM and the VCR are still of complexity $\mathcal{O}(L \ln M)$, except that now L is not a constant, as in QCL. For the datasets used in this letter, VCR yields much more compact circuits than traditional methods for obtaining circuits for unitary operators, such as the QSD, where the number of gates will be $\mathcal{O}(M^2)$. Thus, VCR yields better performance than the traditional methods.

Also, we show using the VCR that we can realize the unitary operator obtained by the UKM using the same ansatz used in QCL and for some cases we can beat the gate counts of QCL as well. In other cases, we have bigger circuits (i.e., L is larger) but with better performance. If data has very high dimensions, i.e. M is very large, the computational time and circuit size might be very large, $\mathcal{O}(M^2)$. But we still have the $\lceil \ln M \rceil$ advantage in the number of qubits n .

However, QCL also has two major potential problems, when M is very large. First, the dataset size has to be very large due to the curse of dimensionality. So the training time and convergence complexity will be a problem no matter what the parameter size is. Second, there is no guarantee that a kernel function with $\mathcal{O}(L \ln M)$ parameters will do well, especially for small L . The performance for small L and large M could be poor. There is no theoretical proof that for large M the QCL will do well with small L . We both use the same number of qubits $\lceil \ln M \rceil$; so in terms of intermediate-scale quantum computers, we both have the same advantage. And the computations of the VCR are in the order of M^2 ; so it is doable for any reasonable size dimension.

Concluding Remarks.— In this letter, we have first discussed the mathematical relationship between VQC/QCL and the kernel method. This relationship implies that VQC including QCL is a subset of the classical kernel method and cannot outperform the kernel method.

Then we have proposed the UKM for classification problems. Mathematically the UKM lies between the kernel method and the QCL, and thus it is expected to provide us an upper bound on the performance of QCL. By numerical simulation, we have shown that the UKM is better than QCL, as expected.

We also have proposed the VCR to find a circuit geometry that realizes a given unitary operator. By combining the UKM and the VCR, we have shown that we can find a circuit geometry that shows high performance in classification.

Also, we have assumed amplitude encoding, and in future work, we plan to explore the performance of VQC for other forms of encoding the classical data. For example, one straightforward extension would be to embed the feature vector $x_i \in \mathbb{R}^M$ into a higher dimensional vector $\phi(x_i) \in \mathbb{R}^L$ with $L = \mathcal{O}(M^c)$ and then use the rest of the framework; the number of qubits n will still be $\mathcal{O}(\log M)$, thus retaining any potential quantum advantage. Such extensions can extend the power of VQC and QCL.

- [1] P. W. Shor, SIAM review **41**, 303 (1999).
- [2] F. Arute, K. Arya, R. Babbush, D. Bacon, J. C. Bardin, R. Barends, R. Biswas, S. Boixo, F. G. Brandao, D. A. Buell, *et al.*, Nature **574**, 505 (2019).
- [3] M. Cerezo, A. Arrasmith, R. Babbush, S. C. Benjamin, S. Endo, K. Fujii, J. R. McClean, K. Mitarai, X. Yuan, L. Cincio, *et al.*, arXiv preprint arXiv:2012.09265 (2020).
- [4] E. Farhi, J. Goldstone, and S. Gutmann, arXiv preprint arXiv:1411.4028 (2014).
- [5] J. R. McClean, J. Romero, R. Babbush, and A. Aspuru-Guzik, New Journal of Physics **18**, 023023 (2016).
- [6] K. Mitarai, M. Negoro, M. Kitagawa, and K. Fujii, Physical Review A **98**, 032309 (2018).
- [7] M. Schuld, A. Bocharov, K. M. Svore, and N. Wiebe, Physical Review A **101**, 032308 (2020).
- [8] C. M. Bishop, *Pattern recognition and machine learning* (springer, 2006).
- [9] K. P. Murphy, *Machine learning: a probabilistic perspective* (MIT press, 2012).
- [10] S. Boyd, S. P. Boyd, and L. Vandenberghe, *Convex optimization* (Cambridge university press, 2004).
- [11] R. Fletcher, *Practical methods of optimization* (John Wiley & Sons, 2013).
- [12] The kernel method is discussed in Sec. G of the SI and the relationship between a VQC and the kernel method is discussed in Sec. H of the SI in detail.
- [13] Refer to Sec. F2 of the SI for the details of quantum circuits.
- [14] For details, refer to Sec. F of the SI.
- [15] J. A. Nelder and R. Mead, The computer journal **7**, 308 (1965).
- [16] J. R. McClean, S. Boixo, V. N. Smelyanskiy, R. Babbush, and H. Neven, Nature communications **9**, 1 (2018).
- [17] R. Lai and S. Osher, Journal of Scientific Computing **58**, 431 (2014).
- [18] S. Osher, M. Burger, D. Goldfarb, J. Xu, and W. Yin, Multiscale Modeling & Simulation **4**, 460 (2005).
- [19] W. Yin, S. Osher, D. Goldfarb, and J. Darbon, SIAM Journal on Imaging sciences **1**, 143 (2008).
- [20] See Sec. I1 in the SI for details.
- [21] See Sec. I4 for details.
- [22] See Sec. J2 for details.
- [23] See Secs. I4 and J1 of the SI for details.
- [24] For the details of the UKM, refer to Sec. J1 of the SI.
- [25] OU is explained in Sec. J1 of the SI.
- [26] V. V. Shende, S. S. Bullock, and I. L. Markov, IEEE Transactions on Computer-Aided Design of Integrated Circuits and Systems **25**, 1000 (2006).
- [27] M. A. Nielsen and I. Chuang, “Quantum computation and quantum information,” (2002).
- [28] M. Plesch and Č. Brukner, Physical Review A **83**, 032302 (2011).
- [29] The iris dataset in the UCI repository [30] has two labels: (0) ‘B’ and (1) ‘M.’ In the cancer dataset (0 or 1), we consider the classification problem between the 0 label and the 1 label. Furthermore, we relabel 0 with -1 to adjust labels with the eigenvalues of $\hat{\sigma}_z$. For the numerical results for other datasets, refer to Sec. L2 of the SI.
- [30] D. Dua and C. Graff, “UCI machine learning repository,” (2017).
- [31] For the details of numerical settings, refer to Sec. L1 of the SI.
- [32] Refer to Sec. E2 of the SI for the details of the CG method and Sec. J3 of the SI for the details of the UKM with the CG method.
- [33] The definitions of the CNOT-based circuit, the CRot-based circuit, the 1d Heisenberg circuit, and the FC Heisenberg circuit are given in Sec. F2 of the SI.
- [34] Particularly, we use Ridge classification as the kernel method. In Ridge classification, we make prediction on the label of x_i by $f_{\text{pred}}(x_i; v) := \frac{1}{N} \sum_j v_j \phi_j(x_i)$ where $v := [v_1, v_2, \dots, v_G]^T$ is a parameter and use the squared error function. For the details of Ridge classification, see Sec. G2 of the SI. Furthermore, the kernel method is described in Sec. G of the SI. Ref. [8, 9] are also helpful.
- [35] In Sec. L of the SI, the numerical results for other datasets are shown.
- [36] D. P. DiVincenzo, Physical Review A **51**, 1015 (1995).
- [37] A. Barenco, C. H. Bennett, R. Cleve, D. P. DiVincenzo, N. Margolus, P. Shor, T. Sleator, J. A. Smolin, and H. Weinfurter, Physical review A **52**, 3457 (1995).
- [38] G. E. Crooks, arXiv preprint arXiv:1905.13311 (2019).
- [39] K. Petersen and M. Pedersen, Technical University of Denmark **15** (2008).
- [40] K. Kreutz-Delgado, arXiv preprint arXiv:0906.4835 (2009).
- [41] R. Fletcher and C. M. Reeves, The computer journal **7**, 149 (1964).
- [42] J. R. Shewchuk *et al.*, “An introduction to the conjugate gradient method without the agonizing pain,” (1994).
- [43] C. G. Broyden, IMA Journal of Applied Mathematics **6**, 76 (1970).
- [44] R. Fletcher, The computer journal **13**, 317 (1970).
- [45] D. Goldfarb, Mathematics of computation **24**, 23 (1970).
- [46] D. F. Shanno, Mathematics of computation **24**, 647 (1970).
- [47] L. Armijo, Pacific Journal of mathematics **16**, 1 (1966).
- [48] P. Wolfe, SIAM review **11**, 226 (1969).
- [49] P. Wolfe, SIAM review **13**, 185 (1971).
- [50] E. Polak and G. Ribiere, ESAIM: Mathematical Modelling and Numerical Analysis-Modélisation Mathématique et Analyse Numérique **3**, 35 (1969).
- [51] M. R. Hestenes, E. Stiefel, *et al.*, Journal of research of the National Bureau of Standards **49**, 409 (1952).
- [52] Y.-H. Dai and Y.-x. Yuan, Annals of Operations Research **103**, 33 (2001).
- [53] M. Schuld, R. Sweke, and J. J. Meyer, arXiv preprint arXiv:2008.08605 (2020).
- [54] K. Fujii and K. Nakajima, Physical Review Applied **8**, 024030 (2017).
- [55] K. Nakajima, K. Fujii, M. Negoro, K. Mitarai, and M. Kitagawa, Physical Review Applied **11**, 034021 (2019).
- [56] R. T. Rockafellar, *Convex analysis*, 28 (Princeton university press, 1970).
- [57] L. M. Bregman, USSR computational mathematics and mathematical physics **7**, 200 (1967).
- [58] E. T. Hale, W. Yin, and Y. Zhang, *A fixed-point continuation method for L_1 -regularization with application to compressed sensing*, Tech. Rep. (2007).
- [59] J. H. Manton, IEEE Transactions on Signal Processing **50**, 635 (2002).

- [60] W. Gibson, *Psychometrika* **27**, 193 (1962).
- [61] M. Schuld and N. Killoran, *Physical review letters* **122**, 040504 (2019).
- [62] The SciPy package [63] provides the **optimize** function, in which the CG method, the BFGS method, and other optimization methods are implemented.
- [63] P. Virtanen, R. Gommers, T. E. Oliphant, M. Haberland, T. Reddy, D. Cournapeau, E. Burovski, P. Peterson, W. Weckesser, J. Bright, S. J. van der Walt, M. Brett, J. Wilson, K. J. Millman, N. Mayorov, A. R. J. Nelson, E. Jones, R. Kern, E. Larson, C. J. Carey, Í. Polat, Y. Feng, E. W. Moore, J. VanderPlas, D. Laxalde, J. Perktold, R. Cimrman, I. Henriksen, E. A. Quintero, C. R. Harris, A. M. Archibald, A. H. Ribeiro, F. Pedregosa, P. van Mulbregt, and SciPy 1.0 Contributors, *Nature Methods* **17**, 261 (2020).
- [64] R. Iten, R. Colbeck, I. Kukuljan, J. Home, and M. Christandl, *Physical Review A* **93**, 032318 (2016).
- [65] E. Knill, arXiv preprint quant-ph/9508006 (1995).
- [66] Y. LeCun and C. Cortes, (2010).

Appendix A: Introduction

This is the supplemental information (SI) for the paper entitled “Ansatz-Independent Variational Quantum Classifier.”

The SI has two major purposes. The first one is to provide the detailed descriptions of the unitary kernel method (UKM) and the variational circuit realization (VCR). The second one is to show additional numerical results of the UKM and the VCR to support the statements in the main text. Furthermore, we explain some useful formulas and related algorithms.

Appendix B: Notation

We introduce some symbols: product operators and matrix norms.

1. Product operator

We define

$$\prod_{j=k}^{k+l} \uparrow \hat{A}_j := \hat{A}_k \hat{A}_{k+1} \dots \hat{A}_{k+l}, \quad (\text{B1})$$

$$\prod_{j=k}^{k+l} \downarrow \hat{A}_j := \hat{A}_{k+l} \hat{A}_{k+l-1} \dots \hat{A}_k. \quad (\text{B2})$$

When Eq. (B1) and Eq. (B2) are identical, we denote them by $\prod_{j=k}^{k+l} \hat{A}_j$.

2. Matrix norms

Let A be a $M \times N$ matrix. We define $a_{i,j} := [A]_{i,j}$ for $i = 1, 2, \dots, M$ and $j = 1, 2, \dots, N$. For $p > 0$, we then define the matrix norm by

$$\|A\|_p := \left(\sum_i \sum_j |a_{i,j}|^p \right)^{\frac{1}{p}}. \quad (\text{B3})$$

From Eq. (B3), we have

$$\|A\|_{\text{F}} := \|A\|_2 \quad (\text{B4})$$

$$= (\text{Tr}[A^{\text{H}} A])^{\frac{1}{2}} \quad (\text{B5})$$

$$= \left(\sum_{i=1}^M \sum_{j=1}^N |a_{i,j}|^2 \right)^{\frac{1}{2}} \quad (\text{B6})$$

$$= \left(\sum_{i=1}^{\min(M,N)} \sigma_i^2 \right)^{\frac{1}{2}}, \quad (\text{B7})$$

where $(\cdot)^{\text{H}}$ denotes the Hermitian conjugate of a matrix.

Appendix C: Rotation operators and their controlled versions

In QCL, rotation gates and their controlled versions play an important role. In this section, we then review them.

1. Many-body operator

When we consider a n -qubit system, it is important to introduce many-body operators. Let $\hat{\sigma}$ be a single-qubit operator. We denote, by $\hat{\sigma}_i$, $\hat{\sigma}$ acting on the i -th qubit of a n -qubit system:

$$\hat{\sigma}_i := \underbrace{\hat{1} \otimes \cdots \otimes \hat{1}}_{i-1} \otimes \hat{\sigma} \otimes \underbrace{\hat{1} \otimes \cdots \otimes \hat{1}}_{n-i}. \quad (\text{C1})$$

For practical computations, we use the Kronecker product. We give its definition:

$$A \otimes B := \begin{bmatrix} a_{1,1}B & a_{1,2}B & \cdots \\ a_{2,1}B & a_{2,2}B & \cdots \\ \vdots & \vdots & \ddots \end{bmatrix}, \quad (\text{C2})$$

where $a_{i,j} := [A]_{i,j}$ is the element of A in the i -th row and j -th column.

The Kronecker product satisfies the following relation:

$$\hat{A} \otimes \hat{B} = (\hat{A} \otimes \hat{1})(\hat{1} \otimes \hat{B}) \quad (\text{C3})$$

$$= \hat{A}_1 \hat{B}_2, \quad (\text{C4})$$

where

$$\hat{A}_1 := \hat{A} \otimes \hat{1}, \quad (\text{C5})$$

$$\hat{B}_2 := \hat{1} \otimes \hat{B}. \quad (\text{C6})$$

In the case of projection operators, we have

$$\hat{P}^0 \otimes \hat{A} + \hat{P}^1 \otimes \hat{B} = \hat{P}_1^0 \hat{A}_2 + \hat{P}_1^1 \hat{B}_2, \quad (\text{C7})$$

where

$$\hat{P}^0 := |0\rangle\langle 0|, \quad (\text{C8})$$

$$\hat{P}^1 := |1\rangle\langle 1|. \quad (\text{C9})$$

2. Rotation gates

Two-qubit gates are known to be universal [27, 36], and we often use single-qubit rotation gates and CNOT gates in practice [27, 37]. Then, we review single-qubit rotation operators $\hat{R}^x(\phi)$, $\hat{R}^y(\phi)$, and $\hat{R}^z(\phi)$.

a. One-qubit case

We first introduce Pauli-matrices:

$$\hat{X} := \hat{\sigma}^x \quad (\text{C10})$$

$$= \begin{bmatrix} 0 & 1 \\ 1 & 0 \end{bmatrix}, \quad (\text{C11})$$

$$\hat{Y} := \hat{\sigma}^y \quad (\text{C12})$$

$$= \begin{bmatrix} 0 & -i \\ i & 0 \end{bmatrix}, \quad (\text{C13})$$

$$\hat{Z} := \hat{\sigma}^z \quad (\text{C14})$$

$$= \begin{bmatrix} 1 & 0 \\ 0 & -1 \end{bmatrix}. \quad (\text{C15})$$

Rotation gates with respect to \hat{X} , \hat{Y} , and \hat{Z} are written as

$$\hat{R}^x(\phi) := e^{-i\frac{\phi}{2}\hat{X}} \quad (\text{C16})$$

$$= \hat{1}_2 \cos(\phi/2) - i\hat{X} \sin(\phi/2) \quad (\text{C17})$$

$$= \begin{bmatrix} \cos(\phi/2) & -i \sin(\phi/2) \\ -i \sin(\phi/2) & \cos(\phi/2) \end{bmatrix}, \quad (\text{C18})$$

$$\hat{R}^y(\phi) := e^{-i\frac{\phi}{2}\hat{Y}} \quad (\text{C19})$$

$$= \hat{1}_2 \cos(\phi/2) - i\hat{Y} \sin(\phi/2) \quad (\text{C20})$$

$$= \begin{bmatrix} \cos(\phi/2) & -\sin(\phi/2) \\ \sin(\phi/2) & \cos(\phi/2) \end{bmatrix}, \quad (\text{C21})$$

$$\hat{R}^z(\phi) := e^{-i\frac{\phi}{2}\hat{Z}} \quad (\text{C22})$$

$$= \hat{1}_2 \cos(\phi/2) - i\hat{Z} \sin(\phi/2) \quad (\text{C23})$$

$$= \begin{bmatrix} e^{-i\phi/2} & 0 \\ 0 & e^{i\phi/2} \end{bmatrix}. \quad (\text{C24})$$

As shown in Ref. [37], the 3-dimensional rotation gate can be expressed as

$$\hat{R}^{3d}(\phi, \theta, \omega) := \hat{R}^z(\omega) \hat{R}^y(\theta) \hat{R}^z(\phi) \quad (\text{C25})$$

$$= \begin{bmatrix} e^{-i\frac{\phi+\omega}{2}} \cos(\theta/2) & -e^{i\frac{\phi-\omega}{2}} \sin(\theta/2) \\ e^{-i\frac{\phi-\omega}{2}} \sin(\theta/2) & e^{i\frac{\phi+\omega}{2}} \cos(\theta/2) \end{bmatrix}. \quad (\text{C26})$$

Eq. (C26) is called the ZYZ decomposition and the combination of this decomposition and the CNOT gate is very useful.

By applying the global phase operator to Eq. (C26), we can express any unitary operator:

$$\hat{R}^{3d}(\phi, \theta, \omega) \hat{\Phi}_2(\lambda) = \begin{bmatrix} e^{-i(\lambda+\frac{\phi+\omega}{2})} \cos(\theta/2) & -e^{-i(\lambda-\frac{\phi-\omega}{2})} \sin(\theta/2) \\ e^{-i(\lambda+\frac{\phi-\omega}{2})} \sin(\theta/2) & e^{-i(\lambda-\frac{\phi+\omega}{2})} \cos(\theta/2) \end{bmatrix}, \quad (\text{C27})$$

where, for $n = 1, 2, \dots$,

$$\hat{\Phi}_{2^n}(\lambda) := e^{-i\lambda} \hat{1}_{2^n}. \quad (\text{C28})$$

b. Many-qubit case

We denote \hat{X} , \hat{Y} , and \hat{Z} acting on the i -th qubit of a n -qubit system by \hat{X}_i , \hat{Y}_i , and \hat{Z}_i , respectively. Furthermore, $\hat{R}_j^{3d}(\phi, \theta, \omega) := \hat{R}_j^z(\omega) \hat{R}_j^y(\theta) \hat{R}_j^z(\phi)$ is the 3-dimensional rotation gate defined in Eq. (C26) on the j -th qubit of a n -qubit system [27, 37].

3. Controlled gates

a. Many-qubit case

Suppose that we have a n -qubit system. We denote, by $\text{Ct}_i[\cdot]$, the controlled two-qubit gate of a given single-qubit gate controlled by the i -th qubit of a n -qubit system. Then, we have

$$\text{Ct}_i[\hat{G}_j] = \hat{P}_i^0 + \hat{P}_i^1 \hat{G}_j, \quad (\text{C29})$$

where \hat{G}_j is \hat{G} acting on the j -th qubit for $j = 1, 2, \dots, n$, and

$$\hat{P}_i^0 := \underbrace{\hat{1}_2 \otimes \dots \otimes \hat{1}_2}_{i-1} \otimes |0\rangle\langle 0| \otimes \underbrace{\hat{1}_2 \otimes \dots \otimes \hat{1}_2}_{n-i} \quad (\text{C30})$$

$$= \frac{1}{2}(\hat{1}_{2^n} + \hat{Z}_i), \quad (\text{C31})$$

$$\hat{P}_i^1 := \underbrace{\hat{1}_2 \otimes \cdots \otimes \hat{1}_2}_{i-1} \otimes |1\rangle\langle 1| \otimes \underbrace{\hat{1}_2 \otimes \cdots \otimes \hat{1}_2}_{n-i} \quad (\text{C32})$$

$$= \frac{1}{2}(\hat{1}_{2^n} - \hat{Z}_i). \quad (\text{C33})$$

Here, \hat{Z}_i is the Pauli-Z operator acting on the i -th qubit of a n -qubit system.

b. Two-qubit case

Let us consider a controlled gate where the first qubit is the control qubit and the second qubit is the target qubit. For any single-qubit operator \hat{A} , its controlled version is defined as

$$\text{Ct}_1[\hat{A}_2] := |0\rangle\langle 0| \otimes \hat{1}_2 + |1\rangle\langle 1| \otimes \hat{A} \quad (\text{C34})$$

$$= \begin{bmatrix} \hat{1}_2 & \hat{0}_2 \\ \hat{0}_2 & \hat{A} \end{bmatrix}, \quad (\text{C35})$$

where $\hat{1}_2$ and $\hat{0}_2$ are the two-dimensional identity operator and the two-dimensional zero operator, respectively. Note that $|0\rangle = |\uparrow\rangle = [1, 0]^\top$ and $|1\rangle = |\downarrow\rangle = [0, 1]^\top$.

For example, we have

$$\text{Ct}_1[\hat{X}_2] = |0\rangle\langle 0| \otimes \hat{1}_2 + |1\rangle\langle 1| \otimes \hat{X} \quad (\text{C36})$$

$$= \begin{bmatrix} 1 & 0 & 0 & 0 \\ 0 & 1 & 0 & 0 \\ 0 & 0 & 0 & 1 \\ 0 & 0 & 1 & 0 \end{bmatrix}, \quad (\text{C37})$$

$$\text{Ct}_2[\hat{X}_1] = \hat{1}_2 \otimes |0\rangle\langle 0| + \hat{X} \otimes |1\rangle\langle 1| \quad (\text{C38})$$

$$= \begin{bmatrix} 1 & 0 & 0 & 0 \\ 0 & 0 & 0 & 1 \\ 0 & 0 & 1 & 0 \\ 0 & 1 & 0 & 0 \end{bmatrix}, \quad (\text{C39})$$

$$\text{Ct}_1[\hat{R}_2^z(\phi)] = \text{Ct}_1[e^{-i\frac{\phi}{2}\hat{Z}_2}] \quad (\text{C40})$$

$$= \begin{bmatrix} 1 & 0 & 0 & 0 \\ 0 & 1 & 0 & 0 \\ 0 & 0 & e^{-i\phi/2} & 0 \\ 0 & 0 & 0 & e^{i\phi/2} \end{bmatrix}, \quad (\text{C41})$$

and

$$\text{Ct}_1[\hat{R}_2^{3d}(\phi, \theta, \omega)] = \text{Ct}_1[\hat{R}_2^z(\omega)]\text{Ct}_1[\hat{R}_2^y(\theta)]\text{Ct}_1[\hat{R}_2^z(\phi)] \quad (\text{C42})$$

$$= \begin{bmatrix} 1 & 0 & 0 & 0 \\ 0 & 1 & 0 & 0 \\ 0 & 0 & e^{-i(\phi+\omega)/2} \cos(\theta/2) & -e^{-i(\phi-\omega)/2} \sin(\theta/2) \\ 0 & 0 & e^{-i(\phi-\omega)/2} \sin(\theta/2) & e^{i(\phi+\omega)/2} \cos(\theta/2) \end{bmatrix}. \quad (\text{C43})$$

4. Gradients on gate operators

In the case of QCL, we often estimate the gradients of expectation values. Here, we review it by following Ref. [38].

a. Multiple gates

The unitary operator in QCL takes the following form:

$$\hat{U}_c(\theta) := \prod_{i=1}^L \hat{U}_{c,i}(\theta_i), \quad (\text{C44})$$

$$\theta := [\theta_1, \theta_2, \dots, \theta_L]^\top. \quad (\text{C45})$$

Then, its derivative becomes

$$\frac{d}{d\theta_j} \hat{U}_c(\theta) = \sum_{i=1}^L \left[\prod_{i'=i+1}^L \hat{U}_{c,i'}(\theta_{i'}) \right] \left(\frac{d}{d\theta_j} \hat{U}_{c,i}(\theta_i) \right) \left[\prod_{i'=1}^{i-1} \hat{U}_{c,i'}(\theta_{i'}) \right]. \quad (\text{C46})$$

b. Expectation values

Formula for computing the derivative of parameters of the rotation gates, Eqs. (C18), (C21), and (C24), are very useful. Here, we describe them by following Ref. [38].

Let us consider the following function:

$$f_{\hat{O}}(\theta) := \langle \psi | \hat{U}_c^\dagger(\theta) \hat{O} \hat{U}_c(\theta) | \psi \rangle, \quad (\text{C47})$$

where a is a constant, \hat{G} is a unitary and Hermitian operator that has two unique eigenvalues, and

$$\hat{U}_c(\theta) := \exp(-ia\theta\hat{G}). \quad (\text{C48})$$

Note that \hat{X}_i , \hat{Y}_i , and \hat{Z}_i all satisfy the conditions of \hat{G} .

The derivative of Eq. (C47) is given by

$$\frac{d}{d\theta} f_{\hat{O}}(\theta) = a[f_{\hat{O}}(\theta + \pi/4a) - f_{\hat{O}}(\theta - \pi/4a)]. \quad (\text{C49})$$

The proof of Eq. (C49) is shown as follows.

Proof. Since \hat{G} is unitary and Hermitian, we have

$$\hat{G}\hat{G} = \hat{G}^\dagger\hat{G} \quad (\text{C50})$$

$$= \hat{1}. \quad (\text{C51})$$

Then, it leads to

$$\hat{U}_c(\theta) = \exp(-ia\theta\hat{G}) \quad (\text{C52})$$

$$= \sum_{j=0}^{\infty} \frac{1}{j!} (-ia\theta\hat{G})^j \quad (\text{C53})$$

$$= \sum_{j=0}^{\infty} \frac{1}{(2j)!} (-ia\theta\hat{G})^{(2j)} + \sum_{j=0}^{\infty} \frac{1}{(2j+1)!} (-ia\theta\hat{G})^{(2j+1)} \quad (\text{C54})$$

$$= \hat{1} \sum_{j=0}^{\infty} \frac{(-1)^j}{(2j)!} (a\theta)^{(2j)} - i\hat{G} \sum_{j=0}^{\infty} \frac{(-1)^j}{(2j+1)!} (a\theta)^{(2j+1)} \quad (\text{C55})$$

$$= \hat{1} \cos(a\theta) - i\hat{G} \sin(a\theta), \quad (\text{C56})$$

and

$$\frac{d}{d\theta} \hat{U}_c(\theta) = \frac{d}{d\theta} \exp(-ia\theta\hat{G}) \quad (\text{C57})$$

$$= -ia\hat{G} \exp(-ia\theta\hat{G}) \quad (\text{C58})$$

$$= -ia\hat{G}\hat{U}_c(\theta). \quad (\text{C59})$$

The derivative of Eq. (C47) becomes

$$\frac{d}{d\theta}f_{\hat{O}}(\theta) = \frac{d}{d\theta}\langle\psi|\hat{U}_c^\dagger(\theta)\hat{O}\hat{U}_c(\theta)|\psi\rangle \quad (\text{C60})$$

$$= \langle\psi|\left[\frac{d}{d\theta}\hat{U}_c^\dagger(\theta)\right]\hat{O}\hat{U}_c(\theta)|\psi\rangle + \langle\psi|\hat{U}_c^\dagger(\theta)\hat{O}\left[\frac{d}{d\theta}\hat{U}_c(\theta)\right]|\psi\rangle \quad (\text{C61})$$

$$= \langle\psi|[ia\hat{G}\hat{U}_c^\dagger(\theta)]\hat{O}\hat{U}_c(\theta)|\psi\rangle + \langle\psi|\hat{U}_c^\dagger(\theta)\hat{O}[-ia\hat{G}\hat{U}_c(\theta)]|\psi\rangle \quad (\text{C62})$$

$$= a\langle\psi|\hat{U}_c^\dagger(\theta)\left[\frac{\hat{1}+i\hat{G}}{\sqrt{2}}\right]\hat{O}\left[\frac{\hat{1}-i\hat{G}}{\sqrt{2}}\right]\hat{U}_c(\theta)|\psi\rangle - a\langle\psi|\hat{U}_c^\dagger(\theta)\left[\frac{\hat{1}-i\hat{G}}{\sqrt{2}}\right]\hat{O}\left[\frac{\hat{1}+i\hat{G}}{\sqrt{2}}\right]\hat{U}_c(\theta)|\psi\rangle \quad (\text{C63})$$

$$= a\langle\psi|\hat{U}_c^\dagger(\theta+\pi/4a)\hat{O}\hat{U}_c(\theta+\pi/4a)|\psi\rangle - a\langle\psi|\hat{U}_c^\dagger(\theta-\pi/4a)\hat{O}\hat{U}_c(\theta-\pi/4a)|\psi\rangle \quad (\text{C64})$$

$$= a[f_{\hat{O}}(\theta+\pi/4a) - f_{\hat{O}}(\theta-\pi/4a)], \quad (\text{C65})$$

where we have used

$$\hat{U}_c(\pm\pi/4a) := \frac{\hat{1} \mp i\hat{G}}{\sqrt{2}}. \quad (\text{C66})$$

Then we have obtained Eq. (C49). □

By setting $a = 1/2$, the expectation value of the derivatives of the rotation gates, Eqs. (C18), (C21), and (C24), are analytically computed as

$$\frac{d}{d\phi}\mathbb{E}_\psi[\hat{R}^w(\phi)] = \frac{1}{2}(\mathbb{E}_\psi[\hat{R}^w(\phi+\pi/2)] - \mathbb{E}_\psi[\hat{R}^w(\phi-\pi/2)]), \quad (\text{C67})$$

for $w = x, y, z$. Here, $\mathbb{E}_\psi[\cdot] := \langle\psi|\cdot|\psi\rangle$.

Appendix D: Matrix derivative

In the UKM, we optimize the cost function of a unitary matrix. Then, we provide the formula of matrix derivatives.

1. Matrix derivative

We review the derivative of the trace with respect to a matrix. For details, refer to Ref. [39, 40].

a. Real case

Let A and X be square matrices and define $a_{i,j}$ and $x_{i,j}$ by

$$a_{i,j} := [A]_{i,j}, \quad (\text{D1})$$

$$x_{i,j} := [X]_{i,j}, \quad (\text{D2})$$

where $[\cdot]_{i,j}$ is the element in the i -th row and the j -th column of a matrix. Then, we have

$$\frac{d}{dx_{i,j}}\text{Tr}[AX^\top] = a_{i,j}, \quad (\text{D3})$$

$$\frac{d}{dx_{i,j}}\text{Tr}[AX] = -a_{j,i}. \quad (\text{D4})$$

The matrix representations of Eqs. (D3) and (D4) are, respectively,

$$\frac{d}{dX}\text{Tr}[AX^\top] = A, \quad (\text{D5})$$

$$\frac{d}{dX} \text{Tr}[AX] = A^\top. \quad (\text{D6})$$

By using Eq. (D5) and (D6), we have

$$\frac{d}{dX} \text{Tr}[AXBX^\top C] = A^\top C^\top XB^\top + CAXB. \quad (\text{D7})$$

b. Complex case

So far, we have considered the matrix derivatives of the trace in the case of real matrices. Here, we present the matrix derivatives in the case of complex matrices.

Let $(\cdot)^*$, $(\cdot)^\top$, and $(\cdot)^{\text{H}}$ denote the complex conjugate, the transpose, and the Hermitian conjugate of a matrix. Then we have

$$A^{\text{H}} = (A^*)^\top \quad (\text{D8})$$

$$= (A^\top)^*. \quad (\text{D9})$$

For a complex matrix X , we denote, by $\Re[X]$ and $\Im[X]$, the real and complex parts of X :

$$\Re[X] := \frac{X + X^*}{2}, \quad (\text{D10})$$

$$\Im[X] := \frac{X - X^*}{2i}. \quad (\text{D11})$$

Furthermore, we define

$$x_{i,j} := [X]_{i,j}, \quad (\text{D12})$$

and

$$x_{i,j}^{\Re} := \Re[x_{i,j}], \quad (\text{D13})$$

$$x_{i,j}^{\Im} := \Im[x_{i,j}]. \quad (\text{D14})$$

From Eq. (D10), we have

$$\text{Tr}[AX^{\text{H}}] = \text{Tr}[A\Re[X^{\text{H}}]] + i\text{Tr}[A\Im[X^{\text{H}}]] \quad (\text{D15})$$

$$= \text{Tr}[A\Re[X^\top]] - i\text{Tr}[A\Im[X^\top]]. \quad (\text{D16})$$

Then, the complex versions of Eqs. (D3) and (D4) are, respectively,

$$\frac{d}{dx_{i,j}^{\Re}} \text{Tr}[AX^{\text{H}}] = a_{i,j}, \quad (\text{D17})$$

$$i \frac{d}{dx_{i,j}^{\Im}} \text{Tr}[AX^{\text{H}}] = a_{i,j}, \quad (\text{D18})$$

and

$$\frac{d}{dx_{i,j}^{\Re}} \text{Tr}[AX] = a_{j,i}, \quad (\text{D19})$$

$$i \frac{d}{dx_{i,j}^{\Im}} \text{Tr}[AX] = a_{j,i}. \quad (\text{D20})$$

Furthermore, from Eqs. (D17) and (D18), the complex versions of Eqs. (D5) and (D6) are, respectively,

$$\frac{d}{d\Re[X]} \text{Tr}[AX^{\text{H}}] = A, \quad (\text{D21})$$

$$i \frac{d}{d\Im[X]} \text{Tr}[AX^H] = A, \quad (\text{D22})$$

and

$$\frac{d}{d\Re[X]} \text{Tr}[AX] = A^\top, \quad (\text{D23})$$

$$i \frac{d}{d\Im[X]} \text{Tr}[AX] = -A^\top. \quad (\text{D24})$$

2. Derivative of the expectation value with respect to a unitary operator

Let $(\cdot)^\dagger$ denote the Hermitian conjugate of an operator. For an operator \hat{A} , we have

$$\hat{A}^\dagger = (\hat{A}^*)^\top \quad (\text{D25})$$

$$= (\hat{A}^\top)^*. \quad (\text{D26})$$

As defined in Eqs. (D10) and (D11), we denote, by $\Re[\hat{U}]$ and $\Im[\hat{U}]$, the real and imaginary parts of \hat{U} :

$$\Re[\hat{U}] := \frac{\hat{U} + \hat{U}^*}{2}, \quad (\text{D27})$$

$$\Im[\hat{U}] := \frac{\hat{U} - \hat{U}^*}{2i}. \quad (\text{D28})$$

The expectation value of \hat{O} with respect to the state that evolves from $\hat{\rho}$ by \hat{U} is given by $\text{Tr}[\hat{U}^\dagger \hat{O} \hat{U} \hat{\rho}]$. In the UKM, it is the central problem to find \hat{U} that minimizes a given cost function. Then, it is helpful if we have the derivative of $\text{Tr}[\hat{U}^\dagger \hat{O} \hat{U} \hat{\rho}]$ with respect to \hat{U} . By using Eqs. (D21) and (D22), we have

$$\frac{d}{d\Re[\hat{U}]} \text{Tr}[\hat{U}^\dagger \hat{O} \hat{U} \hat{\rho}] = \frac{d}{d\Re[\hat{U}]} \text{Tr}[\hat{U}^\dagger \hat{O} \hat{V} \hat{\rho}]|_{\hat{V}=\hat{U}} + \frac{d}{d\Re[\hat{U}]} \text{Tr}[\hat{V}^\dagger \hat{O} \hat{U} \hat{\rho}]|_{\hat{V}^\dagger=\hat{U}^\dagger} \quad (\text{D29})$$

$$= \hat{O} \hat{U} \hat{\rho} + \hat{O}^\top \hat{U}^* \hat{\rho}^\top. \quad (\text{D30})$$

Here, we have used

$$\frac{d}{d\Re[\hat{U}]} \text{Tr}[\hat{U}^\dagger \hat{O} \hat{V} \hat{\rho}]|_{\hat{V}=\hat{U}} = \frac{d}{d\Re[\hat{U}]} \text{Tr}[\hat{O} \hat{V} \hat{\rho} \hat{U}^\dagger]|_{\hat{V}=\hat{U}} \quad (\text{D31})$$

$$= \hat{O} \hat{U} \hat{\rho}, \quad (\text{D32})$$

$$\frac{d}{d\Re[\hat{U}]} \text{Tr}[\hat{V}^\dagger \hat{O} \hat{U} \hat{\rho}]|_{\hat{V}^\dagger=\hat{U}^\dagger} = \frac{d}{d\Re[\hat{U}]} \text{Tr}[\hat{\rho} \hat{V}^\dagger \hat{O} \hat{U}]|_{\hat{V}^\dagger=\hat{U}^\dagger} \quad (\text{D33})$$

$$= (\hat{\rho} \hat{U}^\dagger \hat{O})^\top \quad (\text{D34})$$

$$= \hat{O}^\top \hat{U}^* \hat{\rho}^\top. \quad (\text{D35})$$

Similarly, we also have

$$\frac{d}{d\Im[\hat{U}]} \text{Tr}[\hat{U}^\dagger \hat{O} \hat{U} \hat{\rho}] = \frac{d}{d\Im[\hat{U}]} \text{Tr}[\hat{U}^\dagger \hat{O} \hat{V} \hat{\rho}]|_{\hat{V}=\hat{U}} + \frac{d}{d\Im[\hat{U}]} \text{Tr}[\hat{V}^\dagger \hat{O} \hat{U} \hat{\rho}]|_{\hat{V}^\dagger=\hat{U}^\dagger} \quad (\text{D36})$$

$$= -i \hat{O} \hat{U} \hat{\rho} + i \hat{O}^\top \hat{U}^* \hat{\rho}^\top. \quad (\text{D37})$$

Here, we have used

$$i \frac{d}{d\Im[\hat{U}]} \text{Tr}[\hat{U}^\dagger \hat{O} \hat{V} \hat{\rho}]|_{\hat{V}=\hat{U}} = i \frac{d}{d\Im[\hat{U}]} \text{Tr}[\hat{O} \hat{V} \hat{\rho} \hat{U}^\dagger]|_{\hat{V}=\hat{U}} \quad (\text{D38})$$

$$= \hat{O} \hat{U} \hat{\rho}, \quad (\text{D39})$$

$$i \frac{d}{d\Im[\hat{U}]} \text{Tr}[\hat{V}^\dagger \hat{O} \hat{U} \hat{\rho}]|_{\hat{V}^\dagger=\hat{U}^\dagger} = i \frac{d}{d\Im[\hat{U}]} \text{Tr}[\hat{\rho} \hat{V}^\dagger \hat{O} \hat{U}]|_{\hat{V}^\dagger=\hat{U}^\dagger} \quad (\text{D40})$$

ALGORITHM 2: Iterative method based on linear search

```

1: initialize  $x_0$ 
2: for  $k = 1, 2, \dots, K$  do
3:   compute  $d_k$  that satisfies Eq. (E3)
4:   compute  $\alpha_k$ 
5:   compute  $x_k$  by Eq. (E2)
6: end for

```

$$= -(\hat{\rho}\hat{U}^\dagger\hat{O})^\top \quad (\text{D41})$$

$$= -\hat{O}^\top\hat{U}^*\hat{\rho}^\top. \quad (\text{D42})$$

We utilize Eqs. (D30) and (D37) in the UKM.

Appendix E: Review of optimization methods

In the UKM and the VCR, optimization algorithms play an important role. There are many approaches to solve minimization problems, such as the gradient method, the Newton method, the quasi-Newton method [10, 11]. Among them, the nonlinear conjugate gradient (CG) method [41, 42] is very simple and work well for optimization problems associated with a high dimensional vector [41, 42] and the Broyden-Fletcher-Goldfarb-Shanno (BFGS) method [41, 43–46] is one of the most sophisticated methods. In this paper, the CG method and the UKM and the BFGS method are used for the UKM and the VCR, respectively.

In this section, we review the CG method and the BFGS method as optimization methods. For details, refer to Refs. [10, 11].

1. Basics of the gradient method

Before getting into the CG method the BFGS method, we review the basics of the gradient method.

a. Iteration method based on Linear search

Let us consider the following optimization problem:

$$\min_x \mathcal{J}_{\text{cost}}(x). \quad (\text{E1})$$

Let d_k and α_k be the gradient descent direction and the step size at the k -th iteration, respectively. Then we update x_k by

$$x_k = x_{k-1} + \alpha_k d_k. \quad (\text{E2})$$

To decrease $\mathcal{J}_{\text{cost}}(x)$ in Eq. (E1), the gradient direction d_k must satisfy the following condition:

$$\nabla \mathcal{J}_{\text{cost}}(x_k)^\top d_k < 0. \quad (\text{E3})$$

By using the Taylor expansion, we have

$$\mathcal{J}_{\text{cost}}(x_k) - \mathcal{J}_{\text{cost}}(x_{k-1}) = \alpha_k \left(\nabla \mathcal{J}_{\text{cost}}(x_{k-1})^\top d_k + \frac{o(\alpha_k)}{\alpha_k} \right). \quad (\text{E4})$$

Then, α_k is sufficiently small, Eq. (E2) is expected to work well. We summarize the iterative method based on linear search in Algo. 2.

b. *Linear search*

It is quite important to compute appropriate α_k , and there exist well-known conditions for good α_k . Here we review the conditions for α_k .

To derive the conditions for α_k , let us consider the minimization problem of the following function:

$$\phi(\alpha) := \mathcal{J}_{\text{cost}}(x + \alpha d). \quad (\text{E5})$$

The simplest condition for α_k is the Armijo condition [47] given by

$$\phi(\alpha) \leq \phi(0) + c_1 \alpha \phi'(0), \quad (\text{E6})$$

for $0 < c_1 < 1$. When we use Eq. (E6), α_k is likely to be very small. Another well-used condition for α_k is the Wolfe condition [48, 49] given by

$$\phi(\alpha) \leq \phi(0) + c_1 \alpha \phi'(0), \quad (\text{E7a})$$

$$\phi'(\alpha) \geq c_2 \phi'(0), \quad (\text{E7b})$$

for $0 < c_1 < c_2 < 1$. In this case, $\phi'(\alpha)$ may take a large positive number. To avoid this problem, the following condition for α , which is called the strong Wolfe condition, is used:

$$\phi(\alpha) \leq \phi(0) + c_1 \alpha \phi'(0), \quad (\text{E8a})$$

$$|\phi'(\alpha)| \geq c_2 |\phi'(0)|, \quad (\text{E8b})$$

for $0 < c_1 < c_2 < 1$. Finally, we also mention the Goldstein condition for α given by

$$\phi(0) + (1 - c) \alpha \phi'(0) \leq \phi(\alpha) \quad (\text{E9})$$

$$\leq \phi(0) + c \alpha \phi'(0), \quad (\text{E10})$$

for $0 < c < 1/2$.

To find α_k that satisfies one of the above conditions, the backtracking line search is often used. In the backtracking line search, we set $\alpha_0 > 0$ and iterate the following equation until Eq. (E6) is satisfied:

$$\alpha_k = \rho \alpha_{k-1}, \quad (\text{E11})$$

where $\rho \in (0, 1)$.

2. Nonlinear CG method

In the UKM, the gradient method is utilized to \hat{U}_k in Eq. (J8). The BFGS method is known as a sophisticated method but requires relatively large memory space. Then, we use the CG method in the UKM. Here, we explain the CG method.

a. *Linear CG method*

We begin with the CG method. Let us consider minimizing

$$\mathcal{J}_{\text{cost}}(x) := \frac{1}{2} (x - x_*)^\top A (x - x_*), \quad (\text{E12})$$

where $A > O$.

In the CG method, we set x_0 and $d_0 = -\nabla \mathcal{J}_{\text{cost}}(x_0)$, and then iterate, until convergence,

$$x_k = x_{k-1} + \alpha_k d_{k-1}, \quad (\text{E13a})$$

$$d_k = -\nabla \mathcal{J}_{\text{cost}}(x_k) + \beta_k d_{k-1}, \quad (\text{E13b})$$

where

$$\alpha_k = -\frac{\nabla \mathcal{J}_{\text{cost}}(x_{k-1})^\top d_{k-1}}{d_{k-1}^\top A d_{k-1}}, \quad (\text{E14a})$$

$$\beta_k = \frac{\nabla \mathcal{J}_{\text{cost}}(x_k)^\top A d_{k-1}}{d_{k-1}^\top A d_{k-1}}. \quad (\text{E14b})$$

The CG method is summarized in Algo. 3.

ALGORITHM 3: Conjugate gradient (CG) method

```

1: initialize  $x_0$ 
2: set  $d_0 = -\nabla \mathcal{J}_{\text{cost}}(x_0)$ 
3: for  $k = 1, 2, \dots, K$  do
4:   compute  $x_k$  by Eq. (E13a) with Eq. (E14a)
5:   compute  $d_k$  by Eq. (E13b) with Eq. (E14b)
6: end for

```

ALGORITHM 4: Nonlinear conjugate gradient (CG) method

```

1: initialize  $x_0$ 
2: set  $d_0 = -\nabla \mathcal{J}_{\text{cost}}(x_0)$ 
3: for  $k = 1, 2, \dots, K$  do
4:   compute  $\alpha_k$  by Eq. (E15)
5:   compute  $x_k$  by Eq. (E13a)
6:   compute  $\beta_k$  by Eq. (E16)
7:   compute  $d_k$  by Eq. (E13b)
8: end for

```

b. Nonlinear CG method

Eq. (E14) requires the Hessian matrix A . When we do not know the Hessian, we need to replace Eq. (E14) with different approaches. These approaches are called the nonlinear CG method [41, 42, 50–52].

First, let us focus on how to compute α_k because Eq. (E14a) is not available when we do not know the Hessian. It is very simple because we can use the line search method:

$$\alpha_k = \arg \min_{\alpha} \mathcal{J}_{\text{cost}}(x_{k-1} + \alpha d_{k-1}). \quad (\text{E15})$$

Here, Eqs. (E6) and (E7) are often used.

Next, let us turn our attention to β_k . While we do not elaborate on them, there are several methods to replace β_k in Eq. (E14b):

$$\beta_k = \frac{\|\nabla \mathcal{J}_{\text{cost}}(x_k)\|_{\text{F}}^2}{\|\nabla \mathcal{J}_{\text{cost}}(x_{k-1})\|_{\text{F}}^2}, \quad (\text{E16})$$

$$\beta_k = \frac{\nabla \mathcal{J}_{\text{cost}}(x_k)^\top y_k}{\|\nabla \mathcal{J}_{\text{cost}}(x_{k-1})\|_{\text{F}}^2}, \quad (\text{E17})$$

$$\beta_k = \frac{\nabla \mathcal{J}_{\text{cost}}(x_k)^\top y_k}{d_k^\top y_k}, \quad (\text{E18})$$

$$\beta_k = \frac{\|\nabla \mathcal{J}_{\text{cost}}(x_k)\|_{\text{F}}^2}{d_k^\top y_k}, \quad (\text{E19})$$

where $y_k := \nabla \mathcal{J}_{\text{cost}}(x_k) - \nabla \mathcal{J}_{\text{cost}}(x_{k-1})$. In this paper, we utilize Eq. (E16) called the Fletcher-Reeves method [41]. Eq. (E17), Eq. (E18), and Eq. (E19) are called the Polak-Ribière method [50], the Hestenes-Stiefel method [51], and the Dai-Yuan method [52], respectively.

The nonlinear CG method is summarized in Algo. 4.

3. BFGS method

In this paper, the BFGS method is used for the VCR. The aim of this subsection is to describe the BFGS method [41, 43–46].

ALGORITHM 5: Newton's method

```

1: initialize  $x_0$ 
2: for  $k = 1, 2, \dots, K$  do
3:   compute  $x_k$  by Eq. (E20)
4: end for

```

a. Algorithmic details of the quasi-Newton method

Let us consider the optimization problem, Eq. (E1). We begin with Newton's method. In Newton's method, we set x_0 and iterate the following equation until convergence:

$$x_k = x_{k-1} - (\nabla^2 \mathcal{J}_{\text{cost}}(x_{k-1}))^{-1} \nabla \mathcal{J}_{\text{cost}}(x_{k-1}). \quad (\text{E20})$$

Newton's method is summarized in Algo. 5 The biggest problem of Newton's method is the difficulty of computing $\nabla^2 \mathcal{J}_{\text{cost}}(x_{k-1})^{-1}$ in Eq. (E20). Then some alternative methods, called the quasi-Newton method, were proposed [11].

Let us turn our attention to the quasi-Newton method. In the quasi-Newton method, the gradient descent direction is computed as

$$d_k = -B_k^{-1} \nabla \mathcal{J}_{\text{cost}}(x_k), \quad (\text{E21})$$

where B_k is an approximation of $\nabla^2 \mathcal{J}_{\text{cost}}(x)$. Similarly, Eq. (E21) is equivalent to

$$d_k = -H_k \nabla \mathcal{J}_{\text{cost}}(x_k), \quad (\text{E22})$$

where H_k is an approximation of $[\nabla^2 \mathcal{J}_{\text{cost}}(x)]^{-1}$. Next, by using Eqs. (E6) and (E7), we compute α_k by

$$\alpha_k = \arg \min_{\alpha} \mathcal{J}_{\text{cost}}(x_{k-1} + \alpha d_k). \quad (\text{E23})$$

Then, we update x_k , in the quasi-Newton method, by

$$x_k = x_{k-1} + \alpha_k d_k. \quad (\text{E24})$$

b. Condition for B_k

Next, we consider the condition for B_k . By the Taylor expansion, we have

$$\nabla^2 \mathcal{J}_{\text{cost}}(x_k) \times (x_k - x_{k-1}) = \nabla \mathcal{J}_{\text{cost}}(x_k) - \nabla \mathcal{J}_{\text{cost}}(x_{k-1}) + \mathcal{O}(\|x_k - x_{k-1}\|^2). \quad (\text{E25})$$

By introducing

$$y_k := \nabla \mathcal{J}_{\text{cost}}(x_k) - \nabla \mathcal{J}_{\text{cost}}(x_{k-1}), \quad (\text{E26})$$

$$s_k := x_k - x_{k-1}, \quad (\text{E27})$$

Eq. (E25) is also expressed as

$$\nabla^2 \mathcal{J}_{\text{cost}}(x_k) s_k = y_k + \mathcal{O}(\|s_k\|^2). \quad (\text{E28})$$

Thus, in the quasi-Newton method, the following secant condition is imposed:

$$B_k s_k = y_k. \quad (\text{E29})$$

Eq. (E29) is equivalent to

$$H_k y_k = s_k. \quad (\text{E30})$$

The necessary condition for B_k that satisfies the secant condition, Eq. (E29), to exist, is

$$s_k^\top y_k > 0, \quad (\text{E31})$$

The proof of Eq. (E31) is as follows.

ALGORITHM 6: BFGS method

```

1: initialize  $x_0$ 
2: set  $B_0 = I$ 
3: for  $k = 1, 2, \dots, K$  do
4:   compute  $d_k$  by Eq. (E21)
5:   compute  $\alpha_k$  by Eq. (E23)
6:   compute  $x_k$  by Eq. (E24)
7:   compute  $B_k$  by Eq. (E35)
8: end for

```

Proof. From Eq. (E7b) and $\alpha_k > 0$, we have

$$\nabla \mathcal{J}_{\text{cost}}(x_k)^\top s_k \geq c_2 \nabla \mathcal{J}_{\text{cost}}(x_{k-1})^\top s_k, \quad (\text{E32})$$

where c_2 is a constant that appears in the Wolfe condition, Eq. (E7). Then, we have

$$y_k^\top s_k = \nabla \mathcal{J}_{\text{cost}}(x_k)^\top s_k - \nabla \mathcal{J}_{\text{cost}}(x_{k-1})^\top s_k \quad (\text{E33})$$

$$\geq -(1 - c_2) \nabla \mathcal{J}_{\text{cost}}(x_{k-1})^\top s_k. \quad (\text{E34})$$

Since $c_2 < 1$ and s_k is a gradient descent direction, we obtain Eq. (E31) as a necessary condition for the secant condition, Eq. (E29). □

c. BFGS formula

We do not elaborate on the BFGS method, we here give the BFGS formula. The BFGS formula is given by

$$B_k = B_{k-1} - \frac{B_{k-1} s_k s_k^\top B_{k-1}}{s_k^\top B_{k-1} s_k} + \frac{y_k y_k^\top}{s_k^\top y_k}. \quad (\text{E35})$$

In the case of BFGS formula, we have

$$H_k = \left(I - \frac{s_k y_k^\top}{s_k^\top y_k} \right) H_{k-1} \left(I - \frac{y_k s_k^\top}{s_k^\top y_k} \right) + \frac{s_k s_k^\top}{s_k^\top y_k}. \quad (\text{E36})$$

The quasi-Newton method is summarized in Algo. 6

So far, we explained Eq. (E35), but another formula for B_k is also known. The Davidon-Fletcher-Powell (DFP) formula is given by [11]

$$B_k = \left(I - \frac{y_k s_k^\top}{s_k^\top y_k} \right) B_{k-1} \left(I - \frac{s_k y_k^\top}{s_k^\top y_k} \right) + \frac{y_k y_k^\top}{s_k^\top y_k}. \quad (\text{E37})$$

Appendix F: Quantum circuit learning

QCL was proposed in Refs. [6, 7] as an application of the QAOA and the VQE for machine learning. In this section, we review Refs. [6, 7]. We first explain the ingredients of QCL and then describe the whole procedure of QCL.

1. Encoding

Suppose that we have $\mathcal{D} := \{x_i, y_i\}_{i=1}^N$ and let y_i be the label of x_i . It is an important thing to encode $x_i \in \mathbb{R}^M$ on qubits efficiently.

Suppose that we have a n -qubit system and that the initial state is written as $|\text{init}\rangle$. A typical example of $|\text{init}\rangle$ is given by

$$|\text{init}\rangle := \underbrace{|00 \dots 0\rangle}_n. \quad (\text{F1})$$

We then encode x_i by applying $\hat{S}(x_i)$ on $|\text{init}\rangle$:

$$|\psi^{\text{in}}(x_i)\rangle := \hat{S}(x_i)|\text{init}\rangle. \quad (\text{F2})$$

There exist some novel quantum encoding methods; in Refs. [7, 28], the amplitude encoding is used. In the amplitude encoding, we construct the quantum state for x_i :

$$|\psi^{\text{in}}(x_i)\rangle = \sum_{j=1}^{2^n} \tilde{x}_i^j |j\rangle, \quad (\text{F3})$$

where

$$\tilde{x}_i := \frac{1}{\chi_i} [x_i^1, x_i^2, \dots, x_i^M, c_i^1, c_i^2, \dots, c_i^{M'}], \quad (\text{F4a})$$

$$\chi_i := \sqrt{\sum_{j=1}^M (x_i^j)^2 + \sum_{j=1}^{M'} (c_i^j)^2}. \quad (\text{F4b})$$

Here, $\{c_i^j\}_{j=1}^{M'}$ are certain constant values for padding and $M + M' = 2^n$.

2. Quantum circuit

A near-term quantum device is believed to realize a quantum circuit [2]. Suppose that we have a n -qubit system and a quantum circuit that is parameterized by θ . By applying $\hat{U}_c(\theta)$ realized by the quantum circuit, $|\psi^{\text{in}}(x_i)\rangle$ evolves into

$$|\psi^{\text{out}}(x_i; \theta)\rangle := \hat{U}_c(\theta)|\psi^{\text{in}}(x_i)\rangle, \quad (\text{F5})$$

where

$$\hat{U}_c(\theta) := \prod_{i=1}^L \hat{U}_{c,i}(\theta_i), \quad (\text{F6})$$

$\theta := \{\theta_i\}_{i=1}^L$, and the definition of \prod^\downarrow is given by Eq. (B2).

The functional form of $\hat{U}_{c,i}(\theta_i)$ in Eq. (F6), depends on quantum circuits. In Refs. [6, 7, 53], the following form is often assumed for $\hat{U}_{c,i}(\theta_i)$ in Eq. (F6):

$$\hat{U}_{c,i}(\theta_i) := \left[\prod_{j=1}^n \hat{R}_j^{3\text{d}}(\theta_{i,j}) \right] \hat{U}_{\text{ent}}. \quad (\text{F7})$$

Graphically, $\hat{U}_{c,i}(\theta_i)$, Eq. (F7), for $n = 4$ is expressed as

$$\hat{U}_{c,i}(\theta_i) = \begin{array}{c} \begin{array}{|c|} \hline \hat{U}_{\text{ent}} \\ \hline \end{array} \begin{array}{|c|} \hline \hat{R}^{3\text{d}} \\ \hline \end{array} \begin{array}{|c|} \hline \hat{R}^{3\text{d}} \\ \hline \end{array} \begin{array}{|c|} \hline \hat{R}^{3\text{d}} \\ \hline \end{array} \begin{array}{|c|} \hline \hat{R}^{3\text{d}} \\ \hline \end{array} \end{array}. \quad (\text{F8})$$

Here, $\theta_i := \{\theta_{i,j}\}_{j=1}^n$, $\theta_{i,j} := \{\theta_{i,j,k}\}_{k=1}^3$ and $\hat{R}_j^{3\text{d}}(\theta_{i,j}) := \hat{R}_j^z(\theta_{i,j,3})\hat{R}_j^y(\theta_{i,j,2})\hat{R}_j^z(\theta_{i,j,1})$ is the 3-dimensional rotation gate defined in Eq. (C26) on the j -th qubit [27, 37]. Note that the 3-dimensional rotation can be, in general, decomposed into the product of the z -rotation gate and the y -rotation gate as shown in Refs. [27, 37]. For details, see Sec. C 2.

Two-qubit gates are known to be universal [36]. In Refs. [7, 53], CNOT gates and controlled-rotation gates are used for \hat{U}_{ent} in Eq. (F7). For example, we can use the following for \hat{U}_{ent} in Eq. (F7):

$$\hat{U}_{\text{ent}} = \prod_{j=1}^n \text{Ct}_j[\hat{X}_{j+1}], \quad (\text{F9})$$

where $\hat{X}_{n+1} := \hat{X}_1$. Graphically $\hat{U}_{c,i}(\theta_i)$, Eq. (F9), for $n = 4$ is expressed as

$$\hat{U}_{\text{ent}} = \text{CNOT}(1,2) \text{CNOT}(2,3) \text{CNOT}(3,4) \text{CNOT}(4,1). \quad (\text{F10})$$

Then, $\hat{U}_{c,i}(\theta_i)$ in Eq. (F7) with Eq. (F9) for $n = 4$ graphically becomes

$$\hat{U}_{c,i}(\theta_i) = \text{CNOT}(1,2) \text{CNOT}(2,3) \text{CNOT}(3,4) \text{CNOT}(4,1) \hat{R}^{3d}_1 \hat{R}^{3d}_2 \hat{R}^{3d}_3 \hat{R}^{3d}_4. \quad (\text{F11})$$

If only CNOT gates are used to construct \hat{U}_{ent} like the above example, \hat{U}_{ent} is fixed and free from parameters. Instead of Eq. (F7), we can also use

$$\hat{U}_{c,i}(\theta_i) := \left[\prod_{j=1}^n \hat{R}_j^{3d}(\theta_{i,j}^1) \right] \hat{U}_{\text{ent}}(\theta_{i,j}^2), \quad (\text{F12})$$

where

$$\hat{U}_{\text{ent}}(\theta_i^2) := \prod_{j=1}^n \text{Ct}_j[\hat{R}_{j+1}^{3d}(\theta_{i,j}^2)], \quad (\text{F13})$$

and $\hat{R}_{n+1}^{3d}(\theta_{i,n+1}^2) := \hat{R}_1^{3d}(\theta_{i,1}^2)$. In the case of Eq. (F12), the definition of θ_i is replaced by $\theta_i := \{\theta_i^1, \theta_i^2\}$, and we set $\theta_i^1 := \{\theta_{i,j}^1\}_{j=1}^n$, $\theta_i^2 := \{\theta_{i,j}^2\}_{j=1}^n$, $\theta_{i,j}^1 := \{\theta_{i,j,k}^1\}_{k=1}^3$, and $\theta_{i,j}^2 := \{\theta_{i,j,k}^2\}_{k=1}^3$. Graphically, $\hat{U}_{c,i}(\theta_i)$ in Eq. (F12) for $n = 4$ becomes

$$\hat{U}_{c,i}(\theta_i) = \hat{R}^{3d}_1 \text{CNOT}(1,2) \hat{R}^{3d}_2 \text{CNOT}(2,3) \hat{R}^{3d}_3 \text{CNOT}(3,4) \hat{R}^{3d}_4 \text{CNOT}(4,1) \hat{R}^{3d}_1. \quad (\text{F14})$$

In Ref. [6], the following operator is used for \hat{U}_{ent} in Eq. (F7):

$$\hat{U}_{\text{ent}} = e^{-i\Delta t \hat{H}_H}, \quad (\text{F15})$$

where \hat{H}_H is the Heisenberg model given by

$$\hat{H}_H := \sum_{i,j} J_{i,j} \hat{\sigma}_i \cdot \hat{\sigma}_j + \sum_i \sum_{w=x,y,z} h_i^w \hat{\sigma}_i^w, \quad (\text{F16})$$

$$\hat{\sigma}_i := [\hat{\sigma}_i^x, \hat{\sigma}_i^y, \hat{\sigma}_i^z]^\top. \quad (\text{F17})$$

More generally, \hat{H}_H can involve n -body terms with $n \geq 3$. Graphically, $\hat{U}_{c,i}(\theta_i)$, Eq. (F7), with Eq. (F15) for $n = 4$ is

expressed as

$$\hat{U}_{c,i}(\theta_i) = \begin{array}{c} \begin{array}{|c|} \hline e^{-i\Delta t \hat{H}_H} \\ \hline \end{array} \begin{array}{|c|} \hline \hat{R}^{3d} \\ \hline \hat{R}^{3d} \\ \hline \hat{R}^{3d} \\ \hline \hat{R}^{3d} \\ \hline \end{array} \end{array}. \quad (\text{F18})$$

In numerical simulation, we compare Eqs. (F9), (F13), and (F15).

3. Measurement and prediction

Next, we turn our attention to measurements on $|\psi^{\text{out}}(x_i; \theta)\rangle$ and prediction based on measurements. We obtain the measurement of \hat{O}_j with respect to $|\psi^{\text{out}}(x_i; \theta)\rangle$:

$$\langle \hat{O}_j \rangle_{x_i, \theta} := \langle \psi^{\text{out}}(x_i; \theta) | \hat{O}_j | \psi^{\text{out}}(x_i; \theta) \rangle. \quad (\text{F19})$$

In QCL, the label of x_i is predicted by

$$f_{\text{pred}}(x_i; \theta, \theta_b) := \sum_{j=1}^Q \xi_j \langle \hat{O}_j \rangle_{x_i, \theta} + \theta_b, \quad (\text{F20})$$

where $\xi := [\xi_1, \xi_2, \dots, \xi_Q]$ are fixed parameters. Here θ_b is a bias term to be estimated, but we may set $\theta_b = 0$ for simplicity.

So far, we have focused on quantum circuit learning [6, 7], in which θ is optimized. We here mention the difference between QCL and related algorithms. In the cases of the QAOA and the VQE, $\{\xi_j\}_{j=1}^Q$ are fixed as in case case of QCL; but $\{\xi_j\}_{j=1}^Q$ in QAOA and VQE encode the problem of interest, though $\{\xi_j\}_{j=1}^Q$ in QCL are just fixed parameters.

For the almost same purpose with QCL, quantum reservoir computing (QRC) was proposed in Ref. [54] and Ref. [55]. In QRC, θ is fixed and ξ is optimized. Then, in the above problem setting, $\{\xi_j\}_{j=1}^Q$ are optimized.

4. Cost function and loss functions

To find a good θ , we formulate the optimization problem with respect to θ . In QCL, we consider the optimization problem of minimizing the following cost function:

$$\mathcal{J}_{\text{cost}}(\theta, \theta_b) := \frac{1}{N} \sum_{i=1}^N \ell(y_i, f_{\text{pred}}(x_i; \theta, \theta_b)), \quad (\text{F21})$$

where $\ell(\cdot, \cdot)$ is a loss function [8, 9]. For example, $\ell(\cdot, \cdot)$ takes the form

$$\ell_{\text{SE}}(y, \tilde{y}) := \frac{1}{2} |y - \tilde{y}|^2, \quad (\text{F22})$$

which is called the squared error function. Letting y and \tilde{y} be a label that takes ± 1 and a prediction on y , respectively, another example is

$$\ell_{\text{hinge}}(y, \tilde{y}) := \max(0, 1 - y\tilde{y}), \quad (\text{F23})$$

which is called the hinge function. Letting y and \tilde{y} be a label that takes 0 or 1 and a prediction on y , respectively, we can use

$$\ell_{\text{XE}}(y, \tilde{y}) := -y \ln \tilde{y} - (1 - y) \ln(1 - \tilde{y}), \quad (\text{F24})$$

which is called the cross-entropy loss function. In Eq. (F24), y and \tilde{y} are not symmetric though, in Eqs. (F24) and (F23), y and \tilde{y} are symmetric. Note that Eqs. (F22), (F23), and (F24) are not specific to QCL but also used for many machine learning algorithms [8, 9] and the UKM, which is one of the main algorithms of this paper. In Ref. [7], a different cost function is introduced. However, we do not use it in this paper.

ALGORITHM 7: Quantum circuit learning (QCL)

```

1: while termination condition is not satisfied do
2:   compute  $|\psi^{\text{in}}(x_i)\rangle$  in Eq. (F2) for  $i = 1, 2, \dots, N$ 
3:   compute  $|\psi^{\text{out}}(x_i; \theta)\rangle$  in Eq. (F5) for  $i = 1, 2, \dots, N$ 
4:   compute  $\langle \hat{O}_j \rangle_{x_i, \theta}$  in Eq. (F19) for  $j = 1, 2, \dots, Q$  and  $i = 1, 2, \dots, N$ 
5:   compute  $f_{\text{pred}}(x_i; \theta, \theta_b) = \sum_j \xi_j \langle \hat{O}_j \rangle_{x_i, \theta} + \theta_b$  in Eq. (F20) for  $i = 1, 2, \dots, N$ 
6:   update  $\theta$  and  $\theta_b$  by minimizing  $\mathcal{J}_{\text{cost}}(\theta, \theta_b)$  in Eq. (F21)
7: end while

```

ALGORITHM 8: Quantum circuit learning (QCL) with stochastic gradient descent (SGD)

```

1: set  $N' < N$ 
2: while termination condition is not satisfied do
3:   sample  $i_l$  from  $[1, 2, \dots, N]$  for  $l = 1, 2, \dots, N'$ 
4:   compute  $|\psi^{\text{in}}(x_{i_l})\rangle$  in Eq. (F2) for  $l = 1, 2, \dots, N'$ 
5:   compute  $|\psi^{\text{out}}(x_{i_l}; \theta)\rangle$  in Eq. (F5) for  $l = 1, 2, \dots, N'$ 
6:   compute  $\langle \hat{O}_j \rangle_{x_{i_l}, \theta}$  in Eq. (F19) for  $j = 1, 2, \dots, Q$  and  $l = 1, 2, \dots, N'$ 
7:   compute  $f_{\text{pred}}(x_{i_l}; \theta, \theta_b) = \sum_j \xi_j \langle \hat{O}_j \rangle_{x_{i_l}, \theta} + \theta_b$  in Eq. (F20) for  $l = 1, 2, \dots, N'$ 
8:   update  $\theta$  and  $\theta_b$  by minimizing  $\sum_l \ell(y_{i_l}, f_{\text{pred}}(x_{i_l}; \theta, \theta_b))$ 
9: end while

```

5. Algorithmic procedure of QCL

So far, we have explained the ingredients of QCL. Here we explain the whole procedure of QCL. In QCL, we estimate θ in Eq. (F6) by iterating the following two steps. The first step is compute $\langle \hat{O}_j \rangle_{x_i, \theta}$ in Eq. (F19). The first step is done in a quantum device. The second step is update θ and θ_b by minimizing $\mathcal{J}_{\text{cost}}(\theta, \theta_b)$ in Eq. (F21). To update θ , the derivative of $\mathcal{J}_{\text{cost}}(\theta, \theta_b)$ is required; thus, Eq. (C46) and Eq. (C67) are useful. The second step is expected done in a classical device. We repeat these steps until convergence.

Finally, we summarize QCL in Algo. 7. In practice, stochastic gradient descent (SGD) is also used for QCL. Then, the procedure of QCL with SGD is summarized in Algo. 8.

Appendix G: Kernel method

Machine learning provides many kinds of tool kits to analyze a wide range of datasets [8, 9]. Among them, the kernel method is one of the most important approaches because it is very powerful and mathematically simple compared with a mixture model, neural networks, etc [8, 9]. This section is devoted to the kernel method [8, 9].

1. Algorithmic details of the kernel method

Let us assume that we have

$$\mathcal{D} := [(x_1, y_1), (x_2, y_2), \dots, (x_N, y_N)], \quad (\text{G1})$$

where x_i is a data point and y_i is the label of x_i for $i = 1, 2, \dots, N$. We also assume that each data point x_i is a M -dimensional vector:

$$x_i := [x_i^1, x_i^2, \dots, x_i^M]^\top, \quad (\text{G2})$$

where $(\cdot)^\top$ represents the transpose.

We first define the feature map $\phi(\cdot)$ by

$$\phi(x_i) := [\phi_1(x_i), \phi_2(x_i), \dots, \phi_G(x_i)]^\top. \quad (\text{G3})$$

Then, in the kernel method, by using the feature map (G3), the prediction on x_i is done by

$$f_{\text{pred}}(x_i; v) = \sum_{j=1}^G v_j \phi_j(x_i), \quad (\text{G4})$$

where $v := [v_1, v_2, \dots, v_G]^\top$ is the parameter to be estimated. The performance of $f_{\text{pred}}(\cdot; v)$ heavily depends on v ; then it is quite important to estimate v .

To find a good v , the following optimization problem is often considered:

$$\min_v \mathcal{J}_{\text{cost}}(v), \quad (\text{G5})$$

where

$$\mathcal{J}_{\text{cost}}(v) := \frac{1}{N} \sum_{i=1}^N \ell(y_i, f_{\text{pred}}(x_i; v)) + \frac{\lambda}{2} \|v\|_{\text{F}}^2, \quad (\text{G6})$$

and $\|\cdot\|_{\text{F}}$ is the Frobenius norm. For example, the squared error function, Eq. (F22), the hinge function, Eq. (F23), and the cross-entropy loss function, Eq. (F24), are often used for $\ell(\cdot, \cdot)$ in Eq. (G6). Then, the optimal v is given by

$$v_* = \arg \min_v \mathcal{J}_{\text{cost}}(v). \quad (\text{G7})$$

2. Ridge classification

As Eq. (G4), we consider the following function to predict the label of x_i :

$$f_{\text{pred}}(x_i; v) = \sum_{j=1}^G v_j \phi_j(x_i). \quad (\text{G8})$$

Furthermore, let us consider the squared error function, Eq. (F22) for Eq. (G6): In this case, Eq. (G6) becomes

$$\mathcal{J}_{\text{cost}}(v) = \frac{1}{N} \sum_{i=1}^N \ell_{\text{SE}}(y_i, f_{\text{pred}}(x_i; v)) + \frac{\lambda}{2} \|v\|_{\text{F}}^2 \quad (\text{G9})$$

$$= \frac{1}{N} \sum_{i=1}^N \ell_{\text{SE}}\left(y_i, \sum_{j=1}^G v_j \phi_j(x_i)\right) + \frac{\lambda}{2} \sum_{j=1}^G |v_j|^2 \quad (\text{G10})$$

$$= \frac{1}{2N} \sum_{i=1}^N \left[y_i - \sum_{j=1}^G v_j \phi_j(x_i) \right]^2 + \frac{\lambda}{2} \sum_{j=1}^G |v_j|^2. \quad (\text{G11})$$

The classification method based on Eq. (G7) with Eq. (G11) is called Ridge classification.

3. Optimal solution in the case of Ridge classification

Here, we consider the optimal solution of Eq. (G7) in the case of Eq. (G11). By solving $\frac{d}{dv} \mathcal{J}_{\text{cost}}(v) = 0$, we have

$$v = \frac{1}{\lambda N} \sum_{i=1}^N \left[y_i - \sum_{j=1}^G v_j \phi_j(x_i) \right] \phi(x_i). \quad (\text{G12})$$

Defining, for $i = 1, 2, \dots, N$,

$$a_i := \frac{1}{\lambda N} \left[y_i - \sum_{j=1}^G v_j \phi_j(x_i) \right], \quad (\text{G13})$$

Eq. (G12) is rewritten as

$$v = \sum_{i=1}^N a_i \phi(x_i). \quad (\text{G14})$$

Introducing

$$a := [a_1, a_2, \dots, a_N]^\top, \quad (\text{G15})$$

Eq. (G11) is transformed into

$$\mathcal{J}_{\text{cost}}(v) = \frac{1}{2N} \sum_{i=1}^N \left[y_i - \sum_{l=1}^G \left(\sum_{j=1}^N a_j \phi_l(x_j) \right) \phi_l(x_i) \right]^2 + \frac{\lambda}{2} \sum_{l=1}^G \left[\sum_{i=1}^N a_i \phi_l(x_i) \right]^2 \quad (\text{G16})$$

$$= \frac{1}{2N} \sum_{i=1}^N \left[y_i - \sum_{j=1}^N a_j k(x_j, x_i) \right]^2 + \frac{\lambda}{2} \sum_{i,j=1}^N a_i k(x_i, x_j) a_j \quad (\text{G17})$$

$$= \frac{1}{2N} [y - Ka]^\top [y - Ka] + \frac{\lambda}{2} a^\top Ka. \quad (\text{G18})$$

Here we have used

$$k(x_i, x_j) := \phi^\top(x_i) \phi(x_j), \quad (\text{G19})$$

$$y := [y_1, y_2, \dots, y_N]^\top, \quad (\text{G20})$$

$$K := \Phi \Phi^\top, \quad (\text{G21})$$

$$\Phi := [\phi(x_1), \phi(x_2), \dots, \phi(x_N)]^\top. \quad (\text{G22})$$

Each element of the matrix K is also expressed as

$$[K]_{i,j} = k(x_i, x_j), \quad (\text{G23})$$

where $[\cdot]_{i,j}$ is the element in the i -th row and j -th column. Thus, Eq. (G5) is equivalent to

$$\min_a \mathcal{J}_{\text{cost}}(a), \quad (\text{G24})$$

where, as shown in Eq. (G18),

$$\mathcal{J}_{\text{cost}}(a) := \frac{1}{2N} [y - Ka]^\top [y - Ka] + \frac{\lambda}{2} a^\top Ka. \quad (\text{G25})$$

As the solution of Eq. (G24), we have

$$a_* = \frac{1}{N} (K + \lambda N I_N)^{-1} y. \quad (\text{G26})$$

where that I_N is the $N \times N$ identity matrix. The proof of Eq. (G26) is as follows.

Proof. From Eq. (G25), the derivative of $\mathcal{J}_{\text{cost}}(a)$ with respect to a is given by

$$\frac{d}{da} \mathcal{J}_{\text{cost}}(a) = -\frac{1}{N} K [y - Ka] + \lambda Ka \quad (\text{G27})$$

$$= -\frac{1}{N} K [y - (K + \lambda N I_N) a]. \quad (\text{G28})$$

By setting the derivative of $\mathcal{J}_{\text{cost}}(a)$, Eq. (G28), equal to zero and solving it, we have

$$\frac{d}{da} \mathcal{J}_{\text{cost}}(a_*) = 0 \Leftrightarrow -\frac{1}{N} K [y - (K + \lambda N I_N) a_*] = 0 \quad (\text{G29})$$

$$\Leftrightarrow (K + \lambda N I_N) a_* = y \quad (\text{G30})$$

$$\Leftrightarrow a_* = (K + \lambda N I_N)^{-1} y. \quad (\text{G31})$$

Therefore, we have obtained Eq. (G26). □

From Eq. (G15) and (G22), we have

$$v = a^\top \Phi. \quad (\text{G32})$$

Then, the optimal $f_{\text{pred}}(x; v_*)$ is written as

$$f_{\text{pred}}(x; v_*) = v_*^\top \phi(x) \quad (\text{G33})$$

$$= a_*^\top \Phi \phi(x) \quad (\text{G34})$$

$$= y^\top (K + \lambda N I_N)^{-1} k(x), \quad (\text{G35})$$

where

$$k(x) := \Phi \phi(x) \quad (\text{G36})$$

$$= [k(x_1, x), k(x_2, x), \dots, k(x_N, x)]^\top. \quad (\text{G37})$$

Appendix H: Correspondence between QCL and the kernel method

To clarify the properties of QCL [6, 7], we discuss the relationship between quantum computing and the kernel method [8, 9] in this section.

1. Rewriting QCL

Here, we consider the correspondence between QCL [6, 7] and the kernel method [8, 9]. As discussed in Sec. F 4, the optimization of QCL is understood as the minimization problem:

$$\min_{\theta, \theta_b} \mathcal{J}_{\text{cost}}(\theta, \theta_b), \quad (\text{H1})$$

where

$$\mathcal{J}_{\text{cost}}(\theta, \theta_b) := \frac{1}{N} \sum_{i=1}^N \ell(y_i, f_{\text{pred}}(x_i; \theta, \theta_b)). \quad (\text{H2})$$

Note that Eq. (H2) is already given in Eq. (F21), Here, we have used

$$f_{\text{pred}}(x_i; \theta, \theta_b) := \sum_{j=1}^Q \xi_j \langle \hat{O}_j \rangle_{x_i, \theta} + \theta_b, \quad (\text{H3})$$

$$\langle \hat{O}_j \rangle_{x_i, \theta} := \langle \psi^{\text{out}}(x_i; \theta) | \hat{O}_j | \psi^{\text{out}}(x_i; \theta) \rangle, \quad (\text{H4})$$

$$|\psi^{\text{out}}(x_i; \theta)\rangle := \hat{U}_c(\theta) |\psi^{\text{in}}(x_i)\rangle, \quad (\text{H5})$$

$$|\psi^{\text{in}}(x_i)\rangle := \hat{S}(x_i) |\text{init}\rangle. \quad (\text{H6})$$

Note that Eqs. (H3), (H4), (H5), and (H6) are already given in Eqs. (F20), (F19), (F5), and (F2).

To rewrite Eq. (H1), we define

$$\tilde{O}_j(\{u_{k,l}\}_{k,l=1}^{2^n}) := \sum_{\substack{k_1, k_2, \\ k_3, k_4}} [\psi_{k_1}^{\text{in}}(x_i)]^* u_{k_1, k_2}^* O_j^{k_2, k_3} u_{k_3, k_4} \psi_{k_4}^{\text{in}}(x_i), \quad (\text{H7})$$

where

$$\psi_l^{\text{in}}(x_i) := \langle l | \psi^{\text{in}}(x_i) \rangle, \quad (\text{H8})$$

$$O_j^{k,l} := \langle k | \hat{O}_j | l \rangle, \quad (\text{H9})$$

for $k, l = 1, 2, \dots, 2^n$, and $(\cdot)^*$ represents the complex conjugate for scalars. Thus, we have the following relation on Eqs. (H4) and (H7):

$$\langle \hat{O}_j \rangle_{x_i, \theta} = \tilde{O}_j(\{u_{k,l}\}_{k,l=1}^{2^n}). \quad (\text{H10})$$

So far, we have assumed that $\hat{U}_c(\theta)$ is a parametrized universal quantum circuit. By regarding $\{u_{k,l}\}_{k,l=1}^{2^n}$ as variables to be estimated instead of θ in $\hat{U}_c(\theta)$, Eq. (H1) is rewritten as

$$\min_{\{u_{k,l}\}_{k,l=1}^{2^n}, \theta_b} \mathcal{J}_{\text{cost}}(\{u_{k,l}\}_{k,l=1}^{2^n}, \theta_b), \quad (\text{H11a})$$

$$\text{subject to } u_k^H u_l = \delta_{k,l} \quad (k, l = 1, 2, \dots, 2^n), \quad (\text{H11b})$$

where

$$\mathcal{J}_{\text{cost}}(\{u_{k,l}\}_{k,l=1}^{2^n}, \theta_b) := \frac{1}{N} \sum_{i=1}^N \ell \left(y_i, \sum_{j=1}^Q \xi_j \tilde{O}_j(\{u_{k,l}\}_{k,l=1}^{2^n}) + \theta_b \right). \quad (\text{H12})$$

Furthermore, by using the penalty method [10, 11], Eq. (H11) can be expressed as

$$\lim_{\lambda \rightarrow \infty} \min_{\{u_{k,l}\}_{k,l=1}^{2^n}, \theta_b} \mathcal{J}_{\text{pm}}(\{u_{k,l}\}_{k,l=1}^{2^n}, \theta_b; \lambda), \quad (\text{H13})$$

where

$$\mathcal{J}_{\text{pm}}(\{u_{k,l}\}_{k,l=1}^{2^n}, \theta_b; \lambda) := \mathcal{J}_{\text{cost}}(\{u_{k,l}\}_{k,l=1}^{2^n}, \theta_b) + \frac{\lambda}{2} \sum_{k,l=1,2,\dots,2^n} [u_k^H u_l - \delta_{k,l}]^2. \quad (\text{H14})$$

Here we define, for $k = 1, 2, \dots, 2^n$,

$$u_k := [u_{1,k}, u_{2,k}, \dots, u_{2^n,k}]^H, \quad (\text{H15})$$

where $(\cdot)^H := ((\cdot)^*)^\top = ((\cdot)^\top)^*$ is the Hermitian conjugate for vectors and matrices. Furthermore, $\delta_{k,l}$ is the Kronecker delta function:

$$\delta_{k,l} = \begin{cases} 1 & (k = l), \\ 0 & (k \neq l). \end{cases} \quad (\text{H16})$$

As shown in Eq. (H15), $\{u_k\}_{k=1}^{2^n}$ are the k -th column vectors, but we can also use the row vectors for $\{u_k\}_{k=1}^{2^n}$ by replacing Eq. (H11b) with $u_k u_l^H = \delta_{k,l}$.

2. Rewriting the kernel method: Quadratic formulation

Here, to consider the correspondence between QCL and the kernel method, we consider a slightly different formulation of the kernel method. Instead of Eq. (G4), let us make a prediction on y_i by

$$f_{\text{pred}}(x; w) := \sum_{k,l=1,2,\dots,G} w_{k,l} \tilde{\phi}_k(x) \tilde{\phi}_l(x), \quad (\text{H17})$$

where $[w]_{i,j} := w_{i,j}$. Here, $[\cdot]_{i,j}$ is the element in the i -th row and the j -th column. Then, Eq. (G5) is transformed into

$$\min_w \mathcal{J}_{\text{cost}}(w), \quad (\text{H18})$$

where

$$\mathcal{J}_{\text{cost}}(w) := \frac{1}{N} \sum_{i=1}^N \ell(y_i, f_{\text{pred}}(x_i; w)) + \frac{\lambda}{2} \|w\|_{\mathbb{F}}^2 \quad (\text{H19})$$

$$= \frac{1}{N} \sum_{i=1}^N \ell \left(y_i, \sum_{k,l=1,2,\dots,G} w_{k,l} \tilde{\phi}_k(x_i) \tilde{\phi}_l(x_i) \right) + \frac{\lambda}{2} \sum_{k,l=1,2,\dots,G} |w_{k,l}|^2. \quad (\text{H20})$$

At the end of this subsection, we also introduce

$$w_{k,l}^\delta := w_{k,l} + \delta_{k,l}. \quad (\text{H21})$$

Then we can rewrite Eq. (H20) as

$$\mathcal{J}_{\text{cost}}(w^\delta) = \frac{1}{N} \sum_{i=1}^N \ell \left(y_i, \sum_{k,l=1,2,\dots,G} (w_{k,l}^\delta - \delta_{k,l}) \tilde{\phi}_k(x_i) \tilde{\phi}_l(x_i) \right) + \frac{\lambda}{2} \sum_{k,l=1,2,\dots,G} |w_{k,l}^\delta - \delta_{k,l}|^2. \quad (\text{H22})$$

In the rest of this section, we clarify the correspondence between QCL and the kernel method by using Eqs. (H20) and (H22).

3. Correspondence with QCL

So far, we have finished the preparation. We discuss the correspondence between QCL and the kernel method. For simplicity, we set $\theta_b = 0$ in Eq. (F20) in this subsection.

a. Cost functions

We here compare QCL and the kernel method from the viewpoint of cost functions. Eq. (H20) and Eq. (H14) have the following correspondence:

$$\psi_l^{\text{in}}(x_i) \Leftrightarrow \tilde{\phi}_l(x_i), \quad (\text{H23a})$$

$$\sum_j \sum_{k_1, k_2} \xi_j u_{k, k_1}^* O_j^{k_1, k_2} u_{k_2, l} \Leftrightarrow w_{k, l}, \quad (\text{H23b})$$

$$\frac{\lambda}{2} \sum_{k, l} |u_k^H u_l - \delta_{k, l}|^2 \Leftrightarrow \frac{\lambda}{2} \sum_{k, l} |w_{k, l}|^2. \quad (\text{H23c})$$

By using Eq. (H22), we can rewrite Eq. (H23) as

$$\psi_l^{\text{in}}(x_i) \Leftrightarrow \tilde{\phi}_l(x_i), \quad (\text{H24})$$

$$\sum_j \sum_{k_1, k_2} \xi_j u_{k, k_1}^* O_j^{k_1, k_2} u_{k_2, l} \Leftrightarrow w_{k, l}^\delta - \delta_{k, l}, \quad (\text{H25})$$

$$\frac{\lambda}{2} \sum_{k, l} |u_k^H u_l - \delta_{k, l}|^2 \Leftrightarrow \frac{\lambda}{2} \sum_{k, l} |w_{k, l}^\delta - \delta_{k, l}|^2. \quad (\text{H26})$$

b. Feature map and encoding

At the end of this section, we mention the relationship between quantum encoding and the feature map. Depending on \hat{S}_x , $|\psi^{\text{in}}(x_i)\rangle$ varies. When we employ amplitude encoding, described by Eq. (F3), we have

$$\begin{aligned} \psi_l^{\text{in}}(x_i) &= \langle l | \psi^{\text{in}}(x_i) \rangle \\ &= \langle l | \left[\sum_{k=1}^{M+M'} \tilde{x}_i^k \right] |k\rangle \\ &= \tilde{x}_i^l, \end{aligned} \quad (\text{H27})$$

for $l = 1, 2, \dots, 2^n$. But, we can extend Eq. (H27):

$$|\psi^{\text{in}}(x_i)\rangle := \frac{1}{\chi} \sum_{k_1, k_2, \dots} (x_i^{k_1} x_i^{k_2} \dots) |k_1, k_2, \dots, k_M\rangle, \quad (\text{H28})$$

where

$$\chi := \sqrt{\sum_{k_1, k_2, \dots, k_M} (x_i^{k_1} x_i^{k_2} \dots x_i^{k_M})}, \quad (\text{H29})$$

for $k_m = 1, 2, \dots$ and $m = 1, 2, \dots, M$. Note that M is the dimensions of each x_i .

On the other hand, in the kernel method, we need to select the functional form of the feature map. For example, we may adopt the linear map given by

$$\tilde{\phi}(x_i) = [x_i^1, x_i^2, \dots], \quad (\text{H30})$$

and the nonlinear map $\tilde{\phi}(x_i)$ given by

$$\tilde{\phi}(x_i) = [x_i^1, x_i^2, x_i^1 x_i^2, \dots]. \quad (\text{H31})$$

Thus, by tuning parameters, we can associate Eqs. (H30) and (H31) to Eqs. (H27) and (H28), respectively.

Appendix I: Splitting method for orthogonality constrained problems

The main purpose of this section is to review the method of splitting orthogonality constraints (SOC) proposed in Ref. [17]. The method of SOC is based on Bregman iterative regularization proposed in Refs. [18, 19]. We begin with Bregman iterative regularization and discuss its relation with the augmented Lagrange method. Then, we review the method of SOC.

1. Bregman iterative regularization

The method of SOC proposed in Ref. [17] is based on Bregman iterative regularization proposed in Refs. [18, 19]. We then explain Bregman iterative regularization. Let us consider the following optimization problem:

$$\min_x \mathcal{J}_{\text{cost}}(x), \quad (\text{I1a})$$

$$\text{subject to } Ax = g, \quad (\text{I1b})$$

where A is a matrix.

Bregman iterative regularization solves Eq. (I1) by the following approach:

$$x_{k+1} = \arg \min_x \mathcal{J}_{\text{BIR}}(x; x_k, p_k), \quad (\text{I2a})$$

$$p_{k+1} = p_k - rA^\top(Ax_{k+1} - g), \quad (\text{I2b})$$

where

$$\mathcal{J}_{\text{BIR}}(x; y, p) := B_{\mathcal{J}_{\text{cost}}(\cdot)}^p(x, y) + \frac{r}{2} \|Ax - g\|_{\text{F}}^2, \quad (\text{I3})$$

$$B_{\mathcal{J}_{\text{cost}}(\cdot)}^p(x, y) := \mathcal{J}_{\text{cost}}(x) - \mathcal{J}_{\text{cost}}(y) - \langle p, x - y \rangle. \quad (\text{I4})$$

Here, r is a positive constant. The performance of Bregman iterative regularization depends on r ; thus we need to find an appropriate value of r . Letting x_* and p_* be x and p at convergence, we have $p_* \in \partial \mathcal{J}_{\text{cost}}(x_*)$ where $\partial \mathcal{J}_{\text{cost}}(x)$ is the subderivative of $\mathcal{J}_{\text{cost}}(\cdot)$ at x [56]. Suppose that $\mathcal{J}_{\text{cost}}(x)$ is convex for Ω ; the definition of the subderivative is

$$\partial \mathcal{J}_{\text{cost}}(y) = \left\{ c \mid \forall x \in \Omega, \mathcal{J}_{\text{cost}}(x) - \mathcal{J}_{\text{cost}}(y) \geq c(x - y) \right\}. \quad (\text{I5})$$

Note that the conventional Bregman divergence is [57]

$$B_{\mathcal{J}_{\text{cost}}(\cdot)}(x, y) := \mathcal{J}_{\text{cost}}(x) - \mathcal{J}_{\text{cost}}(y) - \langle \nabla \mathcal{J}_{\text{cost}}(y), x - y \rangle; \quad (\text{I6})$$

then Eq. (I4) can be regarded as the subderivative extension of Eq. (I6).

Eq. (I2) can be rewritten as [17]

$$x_{k+1} = \arg \min_x \left[\mathcal{J}_{\text{cost}}(x) + \frac{r}{2} \|Ax - g + b_k\|_{\text{F}}^2 \right], \quad (\text{I7a})$$

$$b_{k+1} = b_k + Ax_{k+1} - g. \quad (\text{I7b})$$

By setting $g_k := g - b_k$, Eq. (I7) is also expressed as [19]

$$x_{k+1} = \arg \min_x \left[\mathcal{J}_{\text{cost}}(x) + \frac{r}{2} \|Ax - g_k\|_{\text{F}}^2 \right], \quad (\text{I8a})$$

$$g_{k+1} = g_k - (Ax_{k+1} - g). \quad (\text{I8b})$$

The equivalence between Eqs. (I2) with $r = 1$ and (I8) with $r = 1$ is shown as follows.

Proof. For clarity, when we consider the algorithm described by (I8), we use \tilde{x}_k instead of x_k .

We first assume, for a certain k , $p_k = A^\top(g_k - A\tilde{x}_k)$. From Eq. (I4), we have

$$B_{\mathcal{J}_{\text{cost}}(\cdot)}^{p_k}(x, x_k) + \frac{1}{2} \|Ax - g\|_{\text{F}}^2 = \mathcal{J}_{\text{cost}}(x) - \mathcal{J}_{\text{cost}}(x_k) - \langle p_k, x - x_k \rangle + \frac{1}{2} \|Ax - g\|_{\text{F}}^2 \quad (\text{I9})$$

$$= \mathcal{J}_{\text{cost}}(x) - \langle (g_k - A\tilde{x}_k), Ax \rangle + \frac{1}{2} \|Ax - g\|_{\mathbb{F}}^2 + C_1 \quad (\text{I10})$$

$$= \mathcal{J}_{\text{cost}}(x) + \frac{1}{2} \|Ax - g - (g_k - A\tilde{x}_k)\|_{\mathbb{F}}^2 + C_2 \quad (\text{I11})$$

$$= \mathcal{J}_{\text{cost}}(x) + \frac{1}{2} \|Ax - g_{k+1}\|_{\mathbb{F}}^2 + C_2, \quad (\text{I12})$$

where

$$C_1 := -\mathcal{J}_{\text{cost}}(x_k) - \langle p_k, -x_k \rangle, \quad (\text{I13})$$

$$C_2 := C_1 - \frac{1}{2} \|g_k - A\tilde{x}_k\|_{\mathbb{F}}^2. \quad (\text{I14})$$

Thus, we have shown that Eqs. (12) and (18) are identical. For details, refer to Ref. [58]. \square

2. Correspondence between Bregman iterative regularization and the augmented Lagrange method

It seems meaningful to clarify the relationship between Bregman iterative regularization and a well-known algorithm. Here we explain the penalty method and the augmented Lagrangian method [10, 11]. Then we see the correspondence between Bregman iterative regularization and the augmented Lagrange method. To this end, let us consider the following optimization problem:

$$\min_x \mathcal{J}_{\text{cost}}(x), \quad (\text{I15a})$$

$$\text{subject to } c_i(x) = 0 \quad (i = 1, 2, \dots, m). \quad (\text{I15b})$$

To find the solution of Eq. (I15), the penalty method solves

$$\lim_{\lambda \rightarrow \infty} \min_x \mathcal{J}_{\text{pm}}(x; \lambda), \quad (\text{I16})$$

where

$$\mathcal{J}_{\text{pm}}(x; \lambda) := \mathcal{J}_{\text{cost}}(x) + \frac{\lambda}{2} \sum_i \|c_i(x)\|_{\mathbb{F}}^2. \quad (\text{I17})$$

Introducing $\lambda := [\lambda_1, \lambda_2, \dots, \lambda_m]^\top$ and $c(x) := [c_1(x), c_2(x), \dots, c_m(x)]^\top$, the augmented Lagrange method for Eq. (I15) solves, for $k = 1, 2, \dots$,

$$\lim_{k \rightarrow \infty} \min_x \mathcal{J}_{\text{alm}}(x; \lambda_k), \quad (\text{I18})$$

where

$$\mathcal{J}_{\text{alm}}(x; \lambda_k) = \mathcal{J}_{\text{cost}}(x) + \lambda_k^\top c(x) + \frac{r}{2} \|c(x)\|_{\mathbb{F}}^2, \quad (\text{I19})$$

$$\lambda_{k+1} = \lambda_k + rc(x_{k+1}), \quad (\text{I20})$$

and $r > 0$ is a parameter.

We note that Eq. (I3) with $r = 1$ and Eq. (I19) with $r = 1$ are equivalent when $c(x)$ is linear. The proof is shown below.

Proof. From the assumption, we can set

$$c(x) = Ax - g. \quad (\text{I21})$$

For a certain k , we impose the following relation:

$$p_k = -A^\top \lambda_k. \quad (\text{I22})$$

Then we have

$$\mathcal{J}_{\text{alm}}(x; \lambda_k) = \mathcal{J}_{\text{cost}}(x) + \langle \lambda_k, (Ax - g) \rangle + \frac{1}{2} \|Ax - g\|_{\mathbb{F}}^2 \quad (\text{I23})$$

$$= \mathcal{J}_{\text{cost}}(x) + \langle \lambda_k, Ax \rangle + \frac{1}{2} \|Ax - g\|_{\mathbb{F}}^2 + C_1 \quad (\text{I24})$$

$$= \mathcal{J}_{\text{cost}}(x) - \langle p_k, x \rangle + \frac{1}{2} \|Ax - g\|_{\mathbb{F}}^2 + C_1 \quad (\text{I25})$$

$$= \mathcal{J}_{\text{cost}}(x) - \mathcal{J}_{\text{cost}}(x_k) - \langle p_k, (x - x_k) \rangle + \frac{1}{2} \|Ax - g\|_{\mathbb{F}}^2 + \mathcal{J}_{\text{cost}}(x_k) - \langle p_k, x_k \rangle + C_1 \quad (\text{I26})$$

$$= B_{\mathcal{J}_{\text{cost}}(\cdot)}^{p_k}(x, x_k) + \frac{1}{2} \|Ax - g\|_{\mathbb{F}}^2 + C_2. \quad (\text{I27})$$

where C_1 and C_2 are constant terms with respect to x given by

$$C_1 := -\langle \lambda_k, g \rangle, \quad (\text{I28})$$

$$C_2 := C_1 + \mathcal{J}_{\text{cost}}(x_k) - \langle p_k, x_k \rangle. \quad (\text{I29})$$

Thus we have shown the equivalence between Eq. (I3) with $r = 1$ and Eq. (I19) with $r = 1$. \square

Furthermore, Eq. (I20) leads to Eq. (I2b). Therefore, we have confirmed the equivalence between Bregman iterative regularization and the augmented Lagrange method.

3. Penalty method and augmented Lagrangian method for optimization problems with orthogonality constraints

Before getting into the method of SOC, we explain the penalty method and the augmented Lagrangian method for optimization problems with orthogonality constraints [10, 11]. Then let us consider the following optimization problem:

$$\min_X \mathcal{J}_{\text{cost}}(X), \quad (\text{I30a})$$

$$\text{subject to } X^{\top}AX = I, \quad (\text{I30b})$$

where $A > O$. Here, I and O are the identity matrix and the zero matrix, respectively.

The penalty method for Eq. (I30) can be formulated as follows:

$$\lim_{\lambda \rightarrow \infty} \min_X \mathcal{J}_{\text{pm}}(X; \lambda), \quad (\text{I31})$$

where

$$\mathcal{J}_{\text{pm}}(X; \lambda) := \mathcal{J}_{\text{cost}}(X) + \frac{\lambda}{2} \|X^{\top}AX - I\|_{\mathbb{F}}^2. \quad (\text{I32})$$

The augmented Lagrange method for Eq. (I30) solves, for $k = 1, 2, \dots$,

$$\lim_{k \rightarrow \infty} \min_X \mathcal{J}_{\text{alm}}(X; \Lambda_k), \quad (\text{I33})$$

where

$$\mathcal{J}_{\text{alm}}(X; \Lambda_k) := \mathcal{J}_{\text{cost}}(X) + \text{Tr}[(\Lambda_k)^{\top}(X^{\top}AX - I)] + \frac{r}{2} \|X^{\top}AX - I\|_{\mathbb{F}}^2, \quad (\text{I34})$$

$$\Lambda_{k+1} = \Lambda_k + r(X^{\top}AX - I), \quad (\text{I35})$$

and $r > 0$ is a parameter.

The main problem with the above approaches is that they are very slow. Then, we review the method of SOC proposed in Ref. [17] in the next subsection.

4. Algorithmic details of the method of SOC

Let us consider the optimization problem given in Eq. (I30). By splitting the constraints, we first rewrite Eq. (I30) as

$$\min_{X,P} \mathcal{J}_{\text{cost}}(X), \quad (\text{I36a})$$

$$\text{subject to } LX = P, \quad (\text{I36b})$$

$$P^\top P = I, \quad (\text{I36c})$$

where L is a matrix that satisfies

$$A = L^\top L. \quad (\text{I37})$$

Next we apply Bregman iterative regularization to Eq. (I36); then, we solve it by iterating the following equations:

$$\{X_k, P_k\} = \arg \min_{X,P} \mathcal{J}_{\text{SOC}}(X; P, D_{k-1}),$$

$$\text{subject to } P^\top P = I, \quad (\text{I38a})$$

$$D_k = D_{k-1} + LX_k - P_k, \quad (\text{I38b})$$

$$(\text{I38c})$$

where

$$\mathcal{J}_{\text{SOC}}(X; P, D) := \mathcal{J}_{\text{cost}}(X) + \frac{r}{2} \|LX - P + D\|_{\mathbb{F}}^2. \quad (\text{I39})$$

Here, r is a positive constant. The performance of the method of SOC depends on r ; thus, we need to find a good value of r . Note that Eq. (I38a) comes from Eq. (I7a).

By dividing Eq. (I38a) into two equations, we rewrite Eq. (I38) as follows:

$$X_k = \arg \min_X \mathcal{J}_{\text{SOC}}(X; P_{k-1}, D_{k-1}), \quad (\text{I40a})$$

$$P_k = \arg \min_P \frac{r}{2} \|P - (LX_k + D_{k-1})\|_{\mathbb{F}}^2,$$

$$\text{subject to } P^\top P = I, \quad (\text{I40b})$$

$$D_k = D_{k-1} + LX_k - P_k. \quad (\text{I40c})$$

Note that Eq. (I40b) comes from the fact that $\mathcal{J}_{\text{cost}}(X)$ does not depend on P :

$$\arg \min_P \frac{r}{2} \|P - (LX_k + D_{k-1})\|_{\mathbb{F}}^2 = \arg \min_P \mathcal{J}_{\text{SOC}}(X_k; P, D_{k-1}). \quad (\text{I41})$$

Furthermore, the closed form solution of Eq. (I40b) is already known as shown in Refs. [17, 59, 60]. We first compute

$$K_{1,k} \Sigma_k K_{2,k}^\top = LX_k + D_{k-1}, \quad (\text{I42})$$

where $K_{1,k}$ and $K_{2,k}^\top$ are orthogonal matrices and Σ_k is a $p \times q$ matrix, the elements of which in the i -th row and the j -th column for $i \neq j$ are zero, and then we can compute P_k in Eq. (I40b) in a closed form by

$$P_k = K_{1,k} I_{p,q} K_{2,k}^\top. \quad (\text{I43})$$

We call Eq. (I40) the method of SOC and it is summarized in Algo. 9.

To explain Eq. (I43), we then state the related theorem by following Ref. [17].

Theorem 1. *Suppose that we have a $p \times q$ matrix Y and let us consider the following problem:*

$$P_Y = \arg \min_P \frac{1}{2} \|P - Y\|,$$

$$\text{subject to } P^\top P = I. \quad (\text{I44})$$

Then, the solution of Eq. (I44) is given by

$$P_Y = K_1 I_{p,q} K_2^\top. \quad (\text{I45})$$

where K_1 and K_2^\top satisfy $K_1 \Sigma K_2^\top = Y$ and Σ is a diagonal matrix whose diagonal elements are the singular values of Y .

ALGORITHM 9: Method of splitting orthogonality constraints (SOC)

```

1: set  $P_0$  and  $D_0$ 
2: for  $k = 1, 2, \dots, K$  do
3:   compute  $X_k$  by Eq. (I40a)
4:   compute  $P_k$  by Eq. (I43)
5:   compute  $D_k$  by Eq. (I40c)
6: end for

```

By setting $Y = LX_k + D_{k-1}$ in Eq. (I44), Eq. (I45) leads to Eq. (I43). The proof of Thm. 1 is given as follows.

Proof. Let us consider the singular value decomposition of Y :

$$Y = K_1 \Sigma K_2^\top, \quad (\text{I46})$$

where K_1 and K_2^\top are $p \times p$ and $q \times q$ orthogonal matrices, respectively, and Σ is a $p \times q$ diagonal matrix in the sense that $\{[\Sigma]_{i,i}\}_i$ are the singular values of Y and $[\Sigma]_{i,j} = 0$ for $i \neq j$.

By using K_1 and K_2^\top in Eq. (I46), we define

$$\tilde{P} := K_1^\top P K_2. \quad (\text{I47})$$

Then, we have

$$\|P - Y\|_{\mathbb{F}}^2 = \|K_1(K_1^\top P K_2 - \Sigma)K_2^\top\|_{\mathbb{F}}^2 \quad (\text{I48})$$

$$= \|K_1(\tilde{P} - \Sigma)K_2^\top\|_{\mathbb{F}}^2 \quad (\text{I49})$$

$$= \|\tilde{P} - \Sigma\|_{\mathbb{F}}^2. \quad (\text{I50})$$

Furthermore, from Eq. (I47), we also have

$$P^\top P = I \Leftrightarrow \tilde{P}^\top \tilde{P} = I. \quad (\text{I51})$$

Then, Eq. (I44) is almost equivalent to

$$P_\Sigma = \arg \min_{\tilde{P}} \frac{1}{2} \|\tilde{P} - \Sigma\|_{\mathbb{F}}^2, \quad (\text{I52})$$

subject to $\tilde{P}^\top \tilde{P} = I.$

It is almost trivial that the solution of Eq. (I52) takes the following form:

$$P_\Sigma = I_{p,q}, \quad (\text{I53})$$

where

$$[I_{p,q}]_{k,l} = \begin{cases} 1 & (k = l) \\ 0 & (k \neq l) \end{cases}. \quad (\text{I54})$$

Here $[\cdot]_{k,l}$ is the element in the k -th row and l -th column. Thus, the closed form solution of Eq. (I44) is given by

$$P_Y = K_1 P_\Sigma K_2^\top \quad (\text{I55})$$

$$= K_1 I_{p,q} K_2^\top. \quad (\text{I56})$$

Thus we have obtained Eq. (I45). □

The UKM described in Sec. J is based on the method of SOC. More precisely, the UKM is based on the complex version of the method of SOC.

Appendix J: Unitary kernel method

This section describes the UKM, which is one of the main algorithms in this paper. We first provide an overview of the UKM and then discuss how to implement it by using the CG method.

1. Algorithmic details of the UKM

We explain the UKM in this section. We first describe the optimization problem and then state how to solve it.

In the UKM, we make a prediction on y_i by $f_{\text{pred}}(x_i; \hat{U}, \theta_b)$. The problem of the UKM is to estimate \hat{U} . To do so, similarly to Eq. (F20), we consider the following cost function:

$$\mathcal{J}_{\text{cost}}(\hat{U}, \theta_b) := \frac{1}{N} \sum_{i=1}^N \ell(y_i, f_{\text{pred}}(x_i; \hat{U}, \theta_b)), \quad (\text{J1})$$

where

$$f_{\text{pred}}(x_i; \hat{U}, \theta_b) := \sum_{j=1}^Q \xi_j \langle \hat{O}_j \rangle_{x_i, \hat{U}} + \theta_b, \quad (\text{J2})$$

$$\langle \hat{O}_j \rangle_{x_i, \hat{U}} := \langle \psi^{\text{out}}(x_i; \hat{U}) | \hat{O}_j | \psi^{\text{out}}(x_i; \hat{U}) \rangle, \quad (\text{J3})$$

$$|\psi^{\text{out}}(x_i; \hat{U})\rangle := \hat{U} |\psi^{\text{in}}(x_i)\rangle, \quad (\text{J4})$$

$$|\psi^{\text{in}}(x_i)\rangle := \hat{S}(x_i) |\text{init}\rangle. \quad (\text{J5})$$

Here, $|\text{init}\rangle$ is a initial quantum state, $\{\xi_j\}_{j=1}^Q$ are fixed parameters, $\{\hat{O}_j\}_{j=1}^Q$ are the set of measurements, $\hat{S}(x_i)$ is the operator to encode x_i on qubits, and $\ell(\cdot, \cdot)$ is a loss function. For example, the squared error function, Eq. (F22), the hinge function, Eq. (F23), and the cross-entropy loss function, Eq. (F24), are often used for $\ell(\cdot, \cdot)$ [8, 9], and the amplitude encoding is used for $\hat{S}(x_i)$ [7, 61]. Note that the dimension of \hat{U} can take any positive integer, but to consider the correspondence with quantum computing, we consider a n -qubit system and then the dimension of \hat{U} is 2^n . Here, θ_b is a bias term to be estimated, but we may set $\theta_b = 0$ for simplicity. Due to the nature of quantum mechanics, \hat{U} in Eq. (J1) is a unitary operator and, to find a unitary operator, the method of SOC discussed in Sec. I4 is applicable. Similarly to Eq. (I30), we estimate \hat{U} and θ_b by solving the following optimization problem:

$$\min_{\hat{U}, \theta_b} \mathcal{J}_{\text{cost}}(\hat{U}, \theta_b), \quad (\text{J6a})$$

$$\text{subject to } \hat{U}^\dagger \hat{U} = \hat{1}_{2^n}. \quad (\text{J6b})$$

To solve Eq. (J6), we use the method of SOC, Eq. (I36). Hereafter we denote, by \hat{X} , an operator obtained by the method of SOC since it does not strictly satisfy the unitarity condition. Then, we rewrite Eq. (J6) as

$$\min_{\hat{X}, \theta_b} \mathcal{J}_{\text{cost}}(\hat{X}, \theta_b), \quad (\text{J7a})$$

$$\text{subject to } \hat{X} = \hat{P}, \quad (\text{J7b})$$

$$\hat{P}^\dagger \hat{P} = \hat{1}_{2^n}. \quad (\text{J7c})$$

Note that L in Eq. (I36) is replaced by the identity operator and the UKM deals with unitary operators though the method of SOC considers the real matrices. Then, we try to explicitly write the update equations for Eq. (J7) by following the method of SOC. From now on, we denote \hat{X} , \hat{P} , \hat{D} , and θ_b at the k -th iteration by \hat{X}_k , \hat{P}_k , \hat{D}_k , and $\theta_{b,k}$, respectively. Like Eqs. (I40a) and (I40b), by introducing \hat{D} , we split Eq. (J7) into

$$\{\hat{X}_k, \theta_{b,k}\} = \arg \min_{\hat{X}, \theta_b} \mathcal{J}_{\text{SOC}}(\hat{X}, \theta_b; \hat{P}_{k-1}, \hat{D}_{k-1}), \quad (\text{J8})$$

and

$$\hat{P}_k = \arg \min_{\hat{P}} \frac{r}{2} \|\hat{P} - (\hat{X}_k + \hat{D}_{k-1})\|_{\text{F}}^2,$$

ALGORITHM 10: Unitary kernel method (UKM)

```

1: set  $\hat{P}_0$  and  $\hat{D}_0$ 
2: for  $k = 1, 2, \dots, K$  do
3:   compute  $\hat{X}_k$  and  $\theta_{b,k}$  by Eq. (J8)
4:   compute  $\hat{P}_k$  by Eq. (J15)
5:   compute  $\hat{D}_k$  by Eq. (J16)
6: end for

```

$$\text{subject to } \hat{P}^\dagger \hat{P} = \hat{1}_{2^n}, \quad (\text{J9})$$

where

$$\mathcal{J}_{\text{SOC}}(\hat{X}, \theta_b; \hat{P}, \hat{D}) := \mathcal{J}_{\text{cost}}(\hat{X}, \theta_b) + \frac{r}{2} \|\hat{X} - \hat{P} + \hat{D}\|_{\mathbb{F}}^2. \quad (\text{J10})$$

Then, we turn our attention to how to solve Eq. (J9). In Thm. 1, we limit ourselves to real matrices. Note that, while Thm. 1 in the previous section and Ref. [17] focus on an orthogonal case, Refs. [59, 60] discuss a unitary case. In the case of operators, Eq. (I44) is transformed into

$$\begin{aligned} \hat{P}_* &= \arg \min_{\hat{P}} \frac{1}{2} \|\hat{P} - \hat{Y}\|, \\ &\text{subject to } \hat{P}^\dagger \hat{P} = \hat{1}. \end{aligned} \quad (\text{J11})$$

Then, the solution of Eq. (J11) becomes

$$\hat{P}_* = \hat{K}_1 \hat{K}_2^\dagger, \quad (\text{J12})$$

where \hat{K}_1 and \hat{K}_2 are unitary matrices that satisfy

$$\hat{Y} = \hat{K}_1 \hat{\Sigma} \hat{K}_2^\dagger, \quad (\text{J13})$$

and $\hat{\Sigma}$ is a diagonal operator in the sense that $\{\langle i | \hat{\Sigma} | i \rangle\}_i$ are the singular values of \hat{Y} and $\langle i | \hat{\Sigma} | j \rangle = 0$ for $i \neq j$. In this paper, we call Eq. (J12) with Eq. (J13) operator unitarization (OU) and in the numerical sections, Secs. L and M, we use OU to obtain matrices that exactly satisfy the unitarity constraint. Thus, to find the solution of Eq. (J9), we first apply the SVD to $\hat{X}_k + \hat{D}_{k-1}$ and compute $\hat{K}_{1,k}$, $\hat{\Sigma}_k$, and $\hat{K}_{2,k}^\dagger$ such that

$$\hat{K}_{1,k} \hat{\Sigma}_k \hat{K}_{2,k}^\dagger = \hat{X}_k + \hat{D}_{k-1}, \quad (\text{J14})$$

where $\hat{K}_{1,k}$ and $\hat{K}_{2,k}^\dagger$ are unitary operators and $\hat{\Sigma}_k$ is a diagonal operator whose diagonal elements are the singular values of $\hat{X}_k + \hat{D}_{k-1}$. We then compute

$$\hat{P}_k = \hat{K}_{1,k} \hat{K}_{2,k}^\dagger. \quad (\text{J15})$$

Note that the dimensions of $\hat{K}_{1,k}$ and $\hat{K}_{2,k}^\dagger$ are identical and thus nothing need to be inserted between $\hat{K}_{1,k}$ and $\hat{K}_{2,k}^\dagger$ though $I_{p,q}$ in Eq. (I54) is inserted between K_1 and K_2^\dagger in Eq. (I45).

At the end of the k -th iteration, like Eq. (I40c), we update \hat{D}_k by

$$\hat{D}_k = \hat{D}_{k-1} + \hat{X}_k - \hat{P}_k. \quad (\text{J16})$$

In the UKM, we iterate Eq. (J8), Eq. (J15), and Eq. (J16) until convergence. The UKM is summarized in Algo. 10 In the next subsection, we elaborate on how to solve Eq. (J8).

2. Derivatives of the cost function

Let us consider the derivatives of Eq. (J1) and (J10). For simplicity, we set $Q = 1$ and $\xi_1 = 1$ in Eq. (J2); we denote the measurement by \hat{O} . Furthermore, we define $\hat{\rho}_i := |\psi^{\text{in}}(x_i)\rangle\langle\psi^{\text{in}}(x_i)|$.

First, we consider the derivatives of Eq. (J1). By using Eq. (D30), we have

$$\frac{d}{d\Re[\hat{X}]} \mathcal{J}_{\text{cost}}(\hat{X}, \theta_b) = \frac{1}{N} \sum_{i=1}^N \left[\frac{d}{dz} \ell(y_i, z) \Big|_{z=f_{\text{pred}}(x_i; \hat{X}, \theta_b)} \right] \frac{d}{d\Re[\hat{X}]} f_{\text{pred}}(x_i; \hat{X}, \theta_b) \quad (\text{J17})$$

$$= \frac{1}{N} \sum_{i=1}^N \left[\frac{d}{dz} \ell(y_i, z) \Big|_{z=f_{\text{pred}}(x_i; \hat{X}, \theta_b)} \right] (\hat{O} \hat{X} \hat{\rho}_i + \hat{O}^\top \hat{X}^* \hat{\rho}_i^\top). \quad (\text{J18})$$

Similarly, by using Eq. (D37), we get

$$\frac{d}{d\Im[\hat{X}]} \mathcal{J}_{\text{cost}}(\hat{X}, \theta_b) = \frac{1}{N} \sum_{i=1}^N \left[\frac{d}{dz} \ell(y_i, z) \Big|_{z=f_{\text{pred}}(x_i; \hat{X}, \theta_b)} \right] \frac{d}{d\Im[\hat{X}]} f_{\text{pred}}(x_i; \hat{X}, \theta_b) \quad (\text{J19})$$

$$= \frac{1}{N} \sum_{i=1}^N \left[\frac{d}{dz} \ell(y_i, z) \Big|_{z=f_{\text{pred}}(x_i; \hat{X}, \theta_b)} \right] (-i \hat{O} \hat{X} \hat{\rho}_i + i \hat{O}^\top \hat{X}^* \hat{\rho}_i^\top). \quad (\text{J20})$$

Finally, we have

$$\frac{d}{d\theta_b} \mathcal{J}_{\text{cost}}(\hat{X}, \theta_b) = \frac{1}{N} \sum_{i=1}^N \left[\frac{d}{dz} \ell(y_i, z) \Big|_{z=f_{\text{pred}}(x_i; \hat{X}, \theta_b)} \right] \frac{d}{d\theta_b} f_{\text{pred}}(x_i; \hat{X}, \theta_b) \quad (\text{J21})$$

$$= \frac{1}{N} \sum_{i=1}^N \left[\frac{d}{dz} \ell(y_i, z) \Big|_{z=f_{\text{pred}}(x_i; \hat{X}, \theta_b)} \right]. \quad (\text{J22})$$

Thus, we have obtained the derivatives of Eq. (J1).

We also give the derivatives of the square of the Frobenius norm since they appear in Eq. (J8). By using Eqs. (D21) and (D23), we have

$$\frac{d}{d\Re[\hat{X}]} \|\hat{X} - \hat{Y}\|_{\text{F}}^2 = \frac{d}{d\Re[\hat{X}]} \text{Tr}[(\hat{X} - \hat{Y})^\dagger (\hat{X} - \hat{Y})] \quad (\text{J23})$$

$$= (\hat{X} - \hat{Y}) + (\hat{X} - \hat{Y})^* \quad (\text{J24})$$

$$= 2\Re[\hat{X} - \hat{Y}]. \quad (\text{J25})$$

Similarly, by using Eqs. (D22) and (D24), we have

$$\frac{d}{d\Im[\hat{X}]} \|\hat{X} - \hat{Y}\|_{\text{F}}^2 = \frac{d}{d\Im[\hat{X}]} \text{Tr}[(\hat{X} - \hat{Y})^\dagger (\hat{X} - \hat{Y})] \quad (\text{J26})$$

$$= -i(\hat{X} - \hat{Y}) + i(\hat{X} - \hat{Y})^* \quad (\text{J27})$$

$$= 2\Im[\hat{X} - \hat{Y}]. \quad (\text{J28})$$

Finally, we consider the derivatives of Eq. (J10). Eqs. (J18) and (J25) lead to

$$\frac{d}{d\Re[\hat{X}]} \mathcal{J}_{\text{SOC}}(\hat{X}, \theta_b; \hat{P}, \hat{D}) = \frac{1}{N} \left[\frac{d}{dz} \ell(y_i, z) \Big|_{z=f_{\text{pred}}(x_i; \hat{X}, \theta_b)} \right] (\hat{O} \hat{X} \hat{\rho}_i + \hat{O}^\top \hat{X}^* \hat{\rho}_i^\top) + r\Re[\hat{X} - \hat{P} + \hat{D}], \quad (\text{J29})$$

and Eqs. (J20) and (J28) also lead to

$$\frac{d}{d\Im[\hat{X}]} \mathcal{J}_{\text{SOC}}(\hat{X}, \theta_b; \hat{P}, \hat{D}) = \frac{1}{N} \sum_{i=1}^N \left[\frac{d}{dz} \ell(y_i, z) \Big|_{z=f_{\text{pred}}(x_i; \hat{X}, \theta_b)} \right] (-i \hat{O} \hat{X} \hat{\rho}_i + i \hat{O}^\top \hat{X}^* \hat{\rho}_i^\top) + r\Im[\hat{X} - \hat{P} + \hat{D}]. \quad (\text{J30})$$

The second term of Eq. (J10) does not depend on θ_b . Thus, similarly to Eq. (J22), we have

$$\frac{d}{d\theta_b} \mathcal{J}_{\text{SOC}}(\hat{X}, \theta_b) = \frac{1}{N} \sum_{i=1}^N \left[\frac{d}{dz} \ell(y_i, z) \Big|_{z=f_{\text{pred}}(x_i; \hat{X}, \theta_b)} \right]. \quad (\text{J31})$$

ALGORITHM 11: Unitary kernel method (UKM) with the conjugate gradient (CG) method

```

1: set  $\hat{P}_0$  and  $\hat{D}_0$ 
2: for  $k = 1, 2, \dots, K$  do
3:   initialize  $\tilde{x}_0$  by Eq. (J33)
4:   set  $d_0 = -\nabla \mathcal{J}_{\text{CG}}(\tilde{x}_0)$ 
5:   for  $k' = 1, 2, \dots, K'$  do
6:     compute  $\tilde{x}_{k'}$  by Eq. (J35a)
7:     compute  $d_{k'}$  by Eq. (J35b)
8:   end for
9:   compute  $\hat{X}_k$  and  $\theta_{b,k}$  from  $\tilde{x}_{K'}$  by Eq. (J33)
10:  compute  $\hat{P}_k$  by Eq. (J9)
11:  compute  $\hat{D}_k$  by Eq. (J15)
12: end for

```

Thus, we have obtained the derivatives of Eq. (J10).

Without specifying $\ell(\cdot, \cdot)$ in Eq. (J1), we cannot go further. Then let us consider the squared error function, Eq. (F22), for $\ell(\cdot, \cdot)$ in Eq. (J1); the derivative of the loss function takes the form

$$\left. \frac{d}{dz} \ell_{\text{SE}}(y_i, z) \right|_{z=f_{\text{pred}}(x_i; \hat{X}, \theta_b)} = -[y_i - f_{\text{pred}}(x_i; \hat{X}, \theta_b)]. \quad (\text{J32})$$

Substituting Eq. (J32) into Eqs. (J29) and (J30), we obtain the derivatives of Eq. (J10) in the case of the squared error function, Eq. (F22).

We employ the **optimize** function [62] in the SciPy package [63] to solve Eq. (J8). Eqs. (J29) and (J30) help it run faster.

3. UKM with the nonlinear CG method

We have explained the UKM in the previous subsection. Here we state how to solve Eq. (J8).

We first define the $2N^2 + 1$ -dimensional real vector \tilde{x} whose element is given by

$$[\tilde{x}]_{2(N(i-1)+(j-1))+1} := \Re[\langle i | \hat{X} | j \rangle], \quad (\text{J33a})$$

$$[\tilde{x}]_{2(N(i-1)+(j-1))+2} := \Im[\langle i | \hat{X} | j \rangle], \quad (\text{J33b})$$

$$[\tilde{x}]_{2N^2+1} := \theta_b, \quad (\text{J33c})$$

for $i, j = 1, 2, \dots, N$, where N is the dimension of \hat{X} . From Eq. (J1) and Eq. (J8), we then define

$$\mathcal{J}_{\text{CG}}(\tilde{x}) := \mathcal{J}_{\text{cost}}(\hat{X}, \theta_b) + \frac{r}{2} \|\hat{X} - \hat{P}_{k-1} + \hat{D}_{k-1}\|_{\text{F}}^2. \quad (\text{J34})$$

Then, similarly to Eq. (E13), we solve Eq. (J8) by

$$\tilde{x}_k = \tilde{x}_{k-1} + \alpha_k d_{k-1}, \quad (\text{J35a})$$

$$d_k = -\nabla \mathcal{J}_{\text{CG}}(\tilde{x}_k) + \beta_k d_{k-1}. \quad (\text{J35b})$$

Here we use the CG method: Eq. (E15) for α_k and Eq. (E16) for β_k , since the BFGS method requires a large memory space then the CG method and for the case of a large number of qubits, the memory space problem becomes severe. Note that Eqs. (D30) and (D37) are available to compute $\nabla \mathcal{J}_{\text{cost}}(\hat{X}, \theta_b)$ and $\nabla \mathcal{J}_{\text{CG}}(\tilde{x})$. Then, we compute \hat{X}_k from \tilde{x} by using by Eq. (J33). Furthermore, we repeat the SOC update K times and the CG update K' times.

We summarize the UKM with the CG method in Algo. 11. In this paper, We perform the UKM with the CG method, Algo. 11, and see its performance in Sec. L.

Appendix K: Variational circuit realization

In the literature, some novel unitary decomposition methods were proposed: the quantum Shannon decomposition (QSD) [26], the column-by-column decomposition [64], Knill's decomposition [27, 65], etc. Despite their usefulness, they require an exponentially large number of CNOT gates when the number of qubits n increases.

In this section, we propose a variational method to obtain a quantum circuit that realizes a given unitary operator, which we call the VCR.

1. Algorithmic details of the VCR

We first assume that a target unitary and a quantum circuit that has the set of parameters. Then, let \hat{U} and $\hat{U}_c(\theta; L)$ be the target unitary operator and the unitary operator composed of gates that are parametrized by $\theta := [\theta_1, \theta_2, \dots]^T$, respectively. So far, we have denoted, by $\hat{U}_c(\theta)$, the unitary realized by a quantum circuit, but we denote it by $\hat{U}_c(\theta; L)$ to emphasize the number of layers L in this section.

In the VCR, we construct a cost function and estimate θ by minimizing the cost function. For example, we can estimate θ by

$$\{\theta_*, \lambda_*\} = \arg \min_{\theta, \lambda} \tilde{\mathcal{J}}_{\text{cost}}(\theta, \lambda; L, p, \hat{U}), \quad (\text{K1})$$

where, for arbitrary $p > 0$,

$$\tilde{\mathcal{J}}_{\text{cost}}(\theta, \lambda; L, p, \hat{U}) := \|\hat{U} - \hat{U}_{c+p}(\theta, \lambda; L)\|_{\mathbb{F}}^p. \quad (\text{K2})$$

The global phase does not matter physically, but it matters for approximating a unitary operator; then we have used, in Eq. (K2), the unitary operator $\hat{U}_{c+p}(\theta, \lambda; L)$ defined by

$$\hat{U}_{c+p}(\theta, \lambda; L) := \hat{\Phi}_{2^n}(\lambda) \hat{U}_c(\theta; L), \quad (\text{K3})$$

where $\hat{\Phi}_{2^n}(\lambda) := e^{-i\lambda} \hat{1}_{2^n}$ is defined in Eq. (C28).

We give another example of a cost function. When \hat{U} and $\hat{U}_{c+p}(\theta, \lambda; L)$ are identical, we have

$$\hat{U}^\dagger \hat{U}_{c+p}(\theta, \lambda; L) = \hat{1}_{2^n}. \quad (\text{K4})$$

Then, we can estimate θ by

$$\{\theta_*, \lambda_*\} = \arg \min_{\theta, \lambda} \mathcal{J}_{\text{cost}}(\theta, \lambda; L, p, \hat{U}), \quad (\text{K5})$$

where, for any $p > 0$,

$$\mathcal{J}_{\text{cost}}(\theta, \lambda; L, p, \hat{U}) := \|\hat{U}^\dagger \hat{U}_{c+p}(\theta, \lambda; L) - \hat{1}_{2^n}\|_{\mathbb{F}}^p. \quad (\text{K6})$$

In a circuit realization, the complexity of a circuit is of great interest. In this letter, we assume a layered structure for a quantum circuit. Thus, given an error threshold δ , it is convenient to define L_δ :

$$\begin{aligned} L_\delta &= \arg \min_L \epsilon_L, \\ &\text{subject to } \epsilon_L \leq \delta, \end{aligned} \quad (\text{K7})$$

where

$$\epsilon_L := \min_{\theta, \lambda} \mathcal{J}_{\text{cost}}(\theta, \lambda; L, p, \hat{U}). \quad (\text{K8})$$

The advantage of the VCR is that the number of CNOT gates is expected to be small though the number of CNOT gates exponentially grows in the QSD. In Sec. M, we perform the VCR and see its performance.

2. Derivatives of the cost functions

To employ the **optimize** function in the SciPy package [63], the derivative of a cost function is required for fast computing. We explain the derivatives of Eqs. (K2) and (K6).

From Eq. (B5), we can rewrite the Frobenius norm by using the trace operator; then Eqs. (K2) and (K6) for $p = 2$ become, respectively,

$$\tilde{\mathcal{J}}_{\text{cost}}(\theta, \lambda; L, 2, \hat{U}) = \text{Tr}\left[\left(\hat{U} - \hat{U}_{c+p}(\theta, \lambda; L)\right)^\dagger \left(\hat{U} - \hat{U}_{c+p}(\theta, \lambda; L)\right)\right], \quad (\text{K9})$$

$$\mathcal{J}_{\text{cost}}(\theta, \lambda; L, 2, \hat{U}) = \text{Tr} \left[\left(\hat{U}^\dagger \hat{U}_{\text{c+p}}(\theta, \lambda; L) - \hat{1}_{2^n} \right)^\dagger \left(\hat{U}^\dagger \hat{U}_{\text{c+p}}(\theta, \lambda; L) - \hat{1}_{2^n} \right) \right]. \quad (\text{K10})$$

Due to the linearity of the trace operation, the following relation holds:

$$\frac{d}{d\theta_i} \text{Tr}[\hat{A}(\theta)] = \text{Tr} \left[\frac{d}{d\theta_i} \hat{A}(\theta) \right]. \quad (\text{K11})$$

Then we have

$$\frac{d}{d\theta_i} \tilde{\mathcal{J}}_{\text{cost}}(\theta, \lambda; L, 2, \hat{U}) = -\text{Tr} \left[\frac{d}{d\theta_i} \hat{U}_{\text{c+p}}^\dagger(\theta, \lambda; L) \left(\hat{U} - \hat{U}_{\text{c+p}}(\theta, \lambda; L) \right) \right] - \text{Tr} \left[\left(\hat{U} - \hat{U}_{\text{c+p}}(\theta, \lambda; L) \right)^\dagger \frac{d}{d\theta_i} \hat{U}_{\text{c+p}}(\theta, \lambda; L) \right], \quad (\text{K12})$$

and

$$\begin{aligned} & \frac{d}{d\theta_i} \mathcal{J}_{\text{cost}}(\theta, \lambda; L, 2, \hat{U}) \\ &= \text{Tr} \left[\left(\hat{U}^\dagger \frac{d}{d\theta_i} \hat{U}_{\text{c+p}}(\theta, \lambda; L) \right)^\dagger \left(\hat{U}^\dagger \hat{U}_{\text{c+p}}(\theta, \lambda; L) - \hat{1}_{2^n} \right) \right] + \text{Tr} \left[\left(\hat{U}^\dagger \hat{U}_{\text{c+p}}(\theta, \lambda; L) - \hat{1}_{2^n} \right)^\dagger \left(\hat{U}^\dagger \frac{d}{d\theta_i} \hat{U}_{\text{c+p}}(\theta, \lambda; L) \right) \right]. \end{aligned} \quad (\text{K13})$$

By using Eq. (C46), we compute $\frac{d}{d\theta_i} \hat{U}_{\text{c+p}}(\theta, \lambda; L)$ in Eqs. (K12) and (K13).

Appendix L: Numerical simulation of the UKM

In this section, we show numerical simulations of QCL and the UKM for several datasets. We first describe the numerical setting and the properties of datasets. Then, we show the results.

1. Numerical setting

To evaluate the performance of QCL and the UKM, we use 5-fold cross-validation (CV) with 5 different random initial conditions. For each method, we select the best model for the training dataset over iterations to compute the performance.

For the UKM, we show the performance of \hat{X} , \hat{P} , and OU of \hat{X} . Refer to Sec. I4 for the details of OU. Furthermore, we consider real and complex matrices as initial inputs.

For QCL, we show the performance of the CNOT-based circuit geometry (F9), the CRot-based circuit geometry (F13), and the Heisenberg circuit geometry (F15). In the Heisenberg circuit geometry, Eq.(F15), we put $h_i^w = 0$ for $i = 1, 2, \dots, n$ and $w = x, y, z$, and we consider two cases for $J_{i,j}$:

$$J_{i,j} = \delta_{j,i+1}, \quad (\text{L1})$$

$$J_{i,j} = \frac{1}{N}, \quad (\text{L2})$$

for $i, j = 1, 2, \dots, n$. Note that Eq. (L1) is the 1-dimensional (1d) Heisenberg model and Eq. (L2) is the fully-connected (FC) Heisenberg model. In the case of the Heisenberg circuits, we set $\Delta t = 0.1$ in Eq. (F15). For QCL, we utilize the stochastic gradient descent method [9].

To create $|\psi^{\text{in}}(x_i)\rangle$ in Eq. (F2) and (J5), we need to fix $\hat{S}(x_i)$. For $\hat{S}(x_i)$ for $i = 1, 2, \dots, N$, we use the amplitude encoding with $c_i^k = 0$ in Eq. (F4) for all i and k , described in Sec. F1. For $\ell(\cdot, \cdot)$ in Eqs. (F21) and (J1), we utilize the squared error function, Eq. (F22). Furthermore, we set $Q = 1$ and $\xi_1 = 1$ in Eqs. (F20) and (J2), and consider two cases on θ_b in Eqs. (F20) and (J2): the cases of fixing $\theta_b = 0$ and estimating θ_b .

2. Datasets

In this section, the following six datasets are used to compare the performance of QCL and the UKM: the iris dataset, the cancer dataset, the wine dataset, the sonar dataset, the semeion dataset in the UCI repository [30], and the MNIST dataset [66].

The original MNIST dataset has 28×28 dimensions. We create the MNIST256 dataset by reducing its dimensions to 16×16 using coarse-graining.

We consider the binary classification problem. The cancer dataset has two labels, (0) “B” and (1) “M”, and the wine dataset has two labels, (0) “R” and (1) “M”.

On the other hand, other datasets have more labels. The iris dataset has three labels: (0) Iris-setosa, (1) Iris-versicolor, and (2) Iris-virginica. When we deal with the classification problem between (0) Iris-setosa and (1) Iris-versicolor, we write the dataset by Iris (0 or 1). When we deal with the classification problem between (0) Iris-setosa and the others, we write it by Iris (0 or non-0). Similarly, when we deal with the classification problem between (1) Iris-setosa and the others, we write the dataset by Iris (1 or non-1).

The wine dataset has three labels: (0) class 1, (1) class 2, and (3) class 3. We consider the classification problem between (0) class 1 and others, we write it as the wine dataset (0 or non-0).

The semeion dataset and the MNIST256 dataset has ten labels from 0 to 9. We write it as (0 or 1) when we consider the classification problem between 0 and 1, and we write it as (0 or non-0) when we consider the classification problem between 0 and the others.

At the end of this subsection, the numbers of datapoints N and dimensions M of the datasets are shown in Table VI.

ID	N	M	n
Iris (0 or 1)	100	4	2
Iris (0 or non-0)	150	4	2
Iris (1 or non-1)	150	4	2
Cancer (0 or 1)	569	30	5
Sonar (0 or 1)	208	60	6
Wine (0 or non-0)	178	14	4
Semeion (0 or 1)	323	256	8
Semeion (0 or non-0)	1593	256	8
MNIST256 (0 or 1)	569	256	8
MNIST256 (0 or non-0)	2766	256	8

TABLE VI: Numbers of datapoints N dimensions M of the datasets and the number of qubits n required for amplitude encoding. Note that $n = \lceil \log_2 M \rceil$.

3. Iris dataset (0 or 1)

We here show the numerical result for the iris dataset (0 or 1). For the UKM, we put $r = 0.010$ and set $K = 30$ and $K' = 10$ in Algo. 11. For QCL, we run iterations 300 times.

In Fig. 7, we show the numerical results of QCL for the 5-fold datasets with 5 different random seeds. In Fig. 8, we show the numerical results of \hat{P} of the UKM for the 5-fold datasets with 5 different random seeds. In Fig. 9, we also show the numerical results of OU of \hat{X} of the UKM for the 5-fold datasets with 5 different random seeds.

We summarize the results of 5-fold CV with 5 different random seeds of QCL and the UKM in Tables VII and VIII, respectively. For QCL and the UKM, we select the best model for the training dataset over iterations to compute the performance. In Fig. 10, we plot the data shown in Tables VII and VIII. We also summarize the results of 5-fold

Algo.	Condition	Training	Test
QCL	CNOT-based, w/o bias	1.0	1.0
QCL	CNOT-based, w/ bias	1.0	1.0
QCL	CRot-based, w/o bias	1.0	0.9953
QCL	CRot-based, w/ bias	1.0	0.9982
QCL	1d Heisenberg, w/o bias	1.0	0.9895
QCL	1d Heisenberg, w/ bias	1.0	0.9874
QCL	FC Heisenberg, w/o bias	1.0	0.9895
QCL	FC Heisenberg, w/ bias	1.0	0.9874

TABLE VII: Results of 5-fold CV with 5 different random seeds of QCL for the iris dataset (0 or 1). The number of layers L is set to 5 and the number of iterations is set to 300.

CV with 5 different random seeds of the kernel method in Table IX. More specifically, we use Ridge classification in

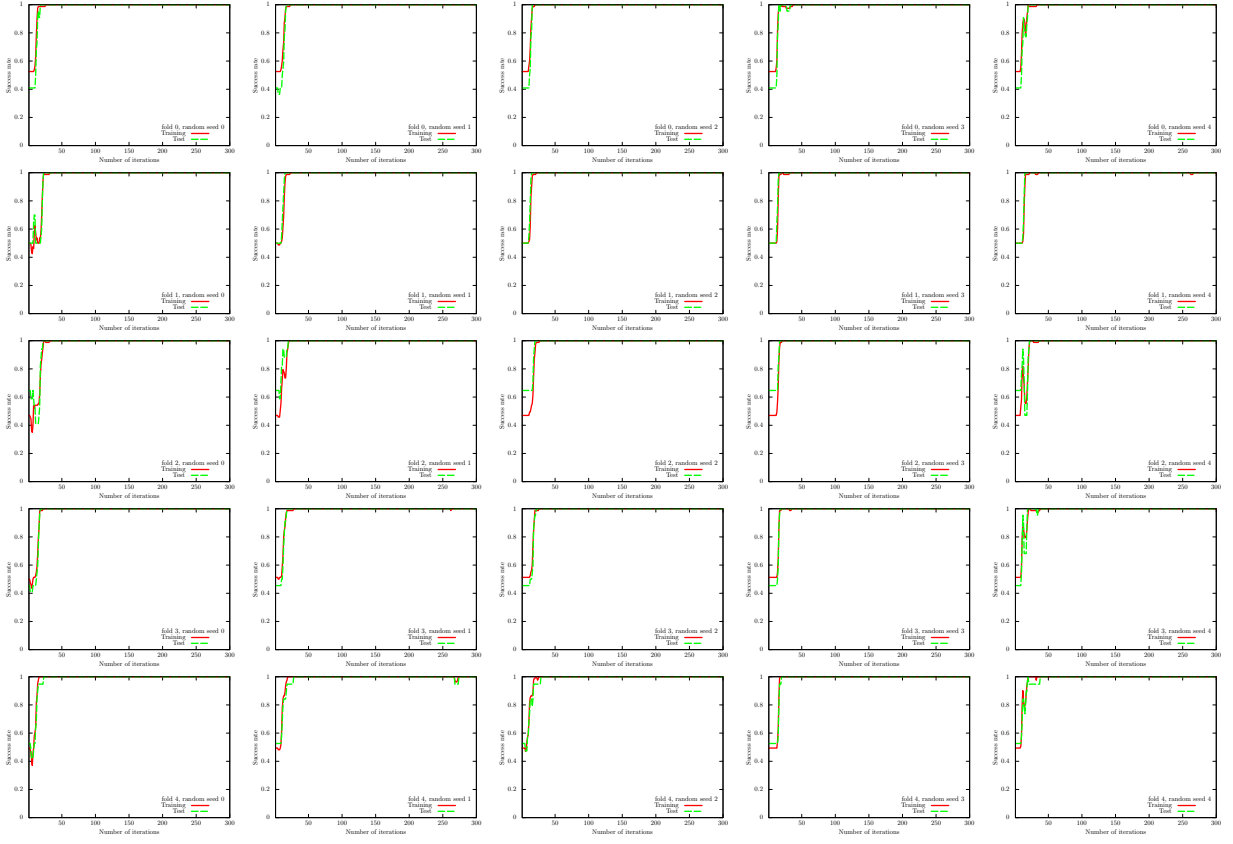


FIG. 7: Results of QCL on the 5-fold datasets with 5 different random seeds for the iris dataset (0 or 1). We use the CNOT-based circuit and set $\theta_{\text{bias}} = 0$. The number of layers L is set to 5.

Algo.	Condition	Training	Test
UKM	\hat{X} , complex, w/o bias	1.0	1.0
UKM	\hat{P} , complex, w/o bias	1.0	1.0
UKM	OU of \hat{X} , complex, w/ bias	1.0	1.0
UKM	\hat{X} , complex, w/ bias	1.0	1.0
UKM	\hat{P} , complex, w/ bias	1.0	1.0
UKM	OU of \hat{X} , real, w/o bias	1.0	1.0
UKM	\hat{X} , real, w/o bias	1.0	1.0
UKM	\hat{P} , real, w/o bias	1.0	1.0
UKM	OU of \hat{X} , real w/o bias	1.0	1.0
UKM	\hat{X} , real, w/ bias	1.0	1.0
UKM	\hat{P} , real, w/ bias	1.0	0.9953
UKM	OU of \hat{X} , real, w/ bias	1.0	0.9953

TABLE VIII: Results of 5-fold CV with 5 different random seeds of the UKM for the iris dataset (0 or 1). We put $r = 0.010$ and set $K = 30$ and $K' = 10$.

Sec. G 2. We consider the linear functions and the second-order polynomial functions for $\phi(\cdot)$ in Eq. (G8) with and without normalization. We set $\lambda = 10^{-2}, 10^{-1}, 1$ where λ is the coefficient of the regularization term.

Next, we show the performance dependence of the three algorithms on their key parameters. We see the performance dependence of QCL on the number of layers L . The result is shown in Fig. 11. We then see the performance dependence of the UKM on r , which is the coefficient of the second term in the right-hand side of Eq. (J8). The result is shown in Fig. 12. In Fig. 13, we show the performance dependence of the kernel method on λ , which is the coefficient of the second term in the right-hand side of Eq. (G11).

So far, we have used the squared error function, Eq. (F22). In Fig. 14, we show the performance dependence of

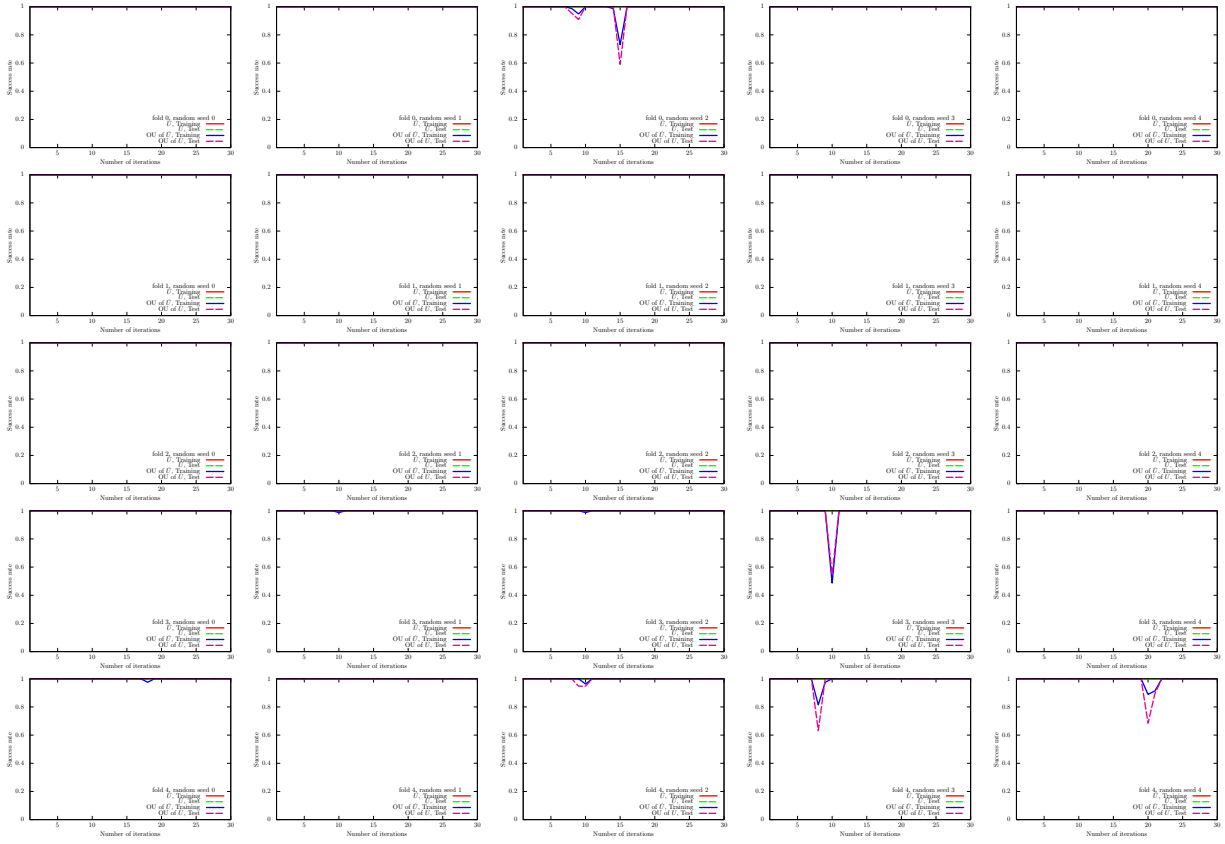


FIG. 8: Results of the UKM (\hat{X} and \hat{P}) on the 5-fold datasets with 5 different random seeds for the iris dataset (0 or 1). We use complex matrices and set $\theta_{\text{bias}} = 0$. We set $r = 0.010$.

Algo.	Condition	Training	Test
Kernel method	Linear, w/o normalization, $\lambda = 10^{-2}$	1.0000	1.0000
Kernel method	Linear, w/o normalization, $\lambda = 10^{-1}$	1.0000	1.0000
Kernel method	Linear, w/o normalization, $\lambda = 1$	1.0000	1.0000
Kernel method	Linear, w/ normalization, $\lambda = 10^{-2}$	1.0000	1.0000
Kernel method	Linear, w/ normalization, $\lambda = 10^{-1}$	1.0000	1.0000
Kernel method	Linear, w/ normalization, $\lambda = 1$	1.0000	1.0000
Kernel method	Poly-2, w/o normalization, $\lambda = 10^{-2}$	1.0000	1.0000
Kernel method	Poly-2, w/o normalization, $\lambda = 10^{-1}$	1.0000	1.0000
Kernel method	Poly-2, w/o normalization, $\lambda = 1$	1.0000	1.0000
Kernel method	Poly-2, w/ normalization, $\lambda = 10^{-2}$	1.0000	1.0000
Kernel method	Poly-2, w/ normalization, $\lambda = 10^{-1}$	1.0000	1.0000
Kernel method	Poly-2, w/ normalization, $\lambda = 1$	1.0000	1.0000

TABLE IX: Results of 5-fold CV with 5 different random seeds of the kernel method for the iris dataset (0 or 1).

QCL on the number of layers L in the case of the hinge function, Eq. (F23). In Fig. 15, we show the performance dependence of the UKM on r , which is the coefficient of the second term in the right-hand side of Eq. (J8), in the case of the hinge function, Eq. (F23).

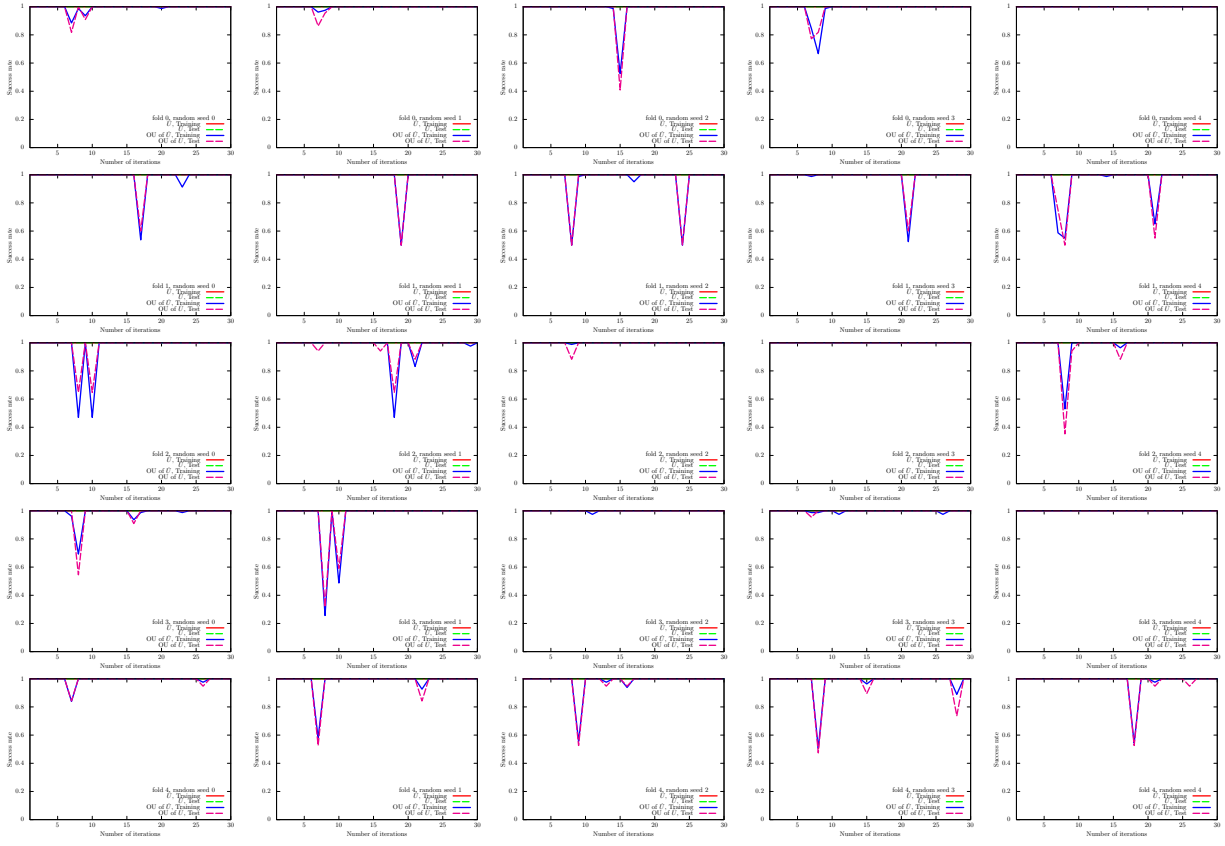


FIG. 9: Results of the UKM (\hat{X} and OU of \hat{X}) on the 5-fold datasets with 5 different random seeds for the iris dataset (0 or 1). We use complex matrices and set $\theta_{\text{bias}} = 0$. We set $r = 0.010$.

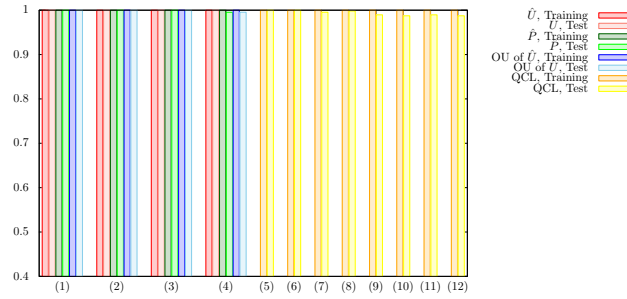


FIG. 10: Results of 5-fold CV with 5 different random seeds for the iris dataset (0 or 1). For the UKM, we put $r = 0.010$ and set $K = 30$ and $K' = 10$. For QCL, the number of layers L is 5 and the number of iterations is 300. The numerical settings are as follows: (1) complex matrices without the bias term, (2) complex matrices with the bias term, (3) real matrices without the bias term, (4) real matrices with the bias term, (5) CNOT-based circuit without the bias term, (6) CNOT-based circuit with the bias term, (7) CRot-based circuit without the bias term, (8) CRot-based circuit with the bias term, (9) 1d Heisenberg circuit without the bias term, (10) 1d Heisenberg circuit with the bias term, (11) FC Heisenberg circuit without the bias term, and (12) FC Heisenberg circuit with the bias term.

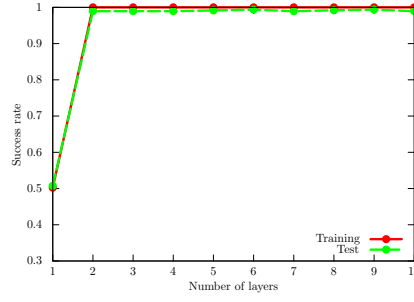


FIG. 11: Performance dependence of QCL on the number of layers L for the iris dataset (0 or 1). We use the CNOT-based circuit geometry and set $\theta_{\text{bias}} = 0$. We iterate the computation 300 times.

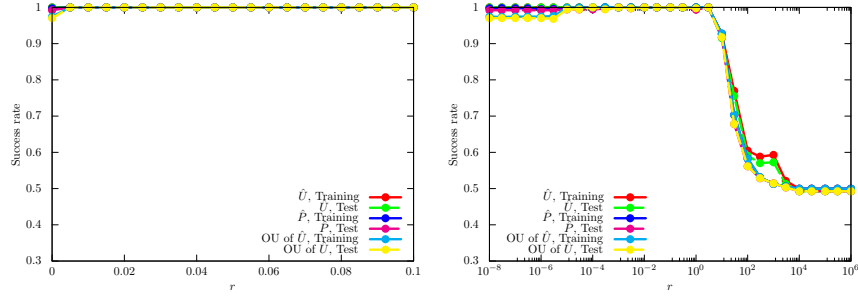


FIG. 12: Performance dependence of the UKM on r , which is the coefficient of the second term in the right-hand side of Eq. (J8) for the iris dataset (0 or 1). We use complex matrices and set $\theta_{\text{bias}} = 0$. We set $K = 30$ and $K' = 10$.

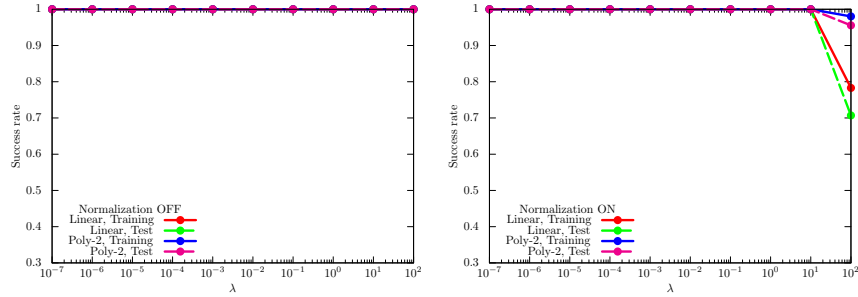


FIG. 13: Performance dependence of the kernel method on λ , which is the coefficient of the second term in the right-hand side of Eq. (G11) for the iris dataset (0 or 1). For $\phi(\cdot)$ in Eq. (G8), we use the linear functions and the second-degree polynomial functions with and without normalization.

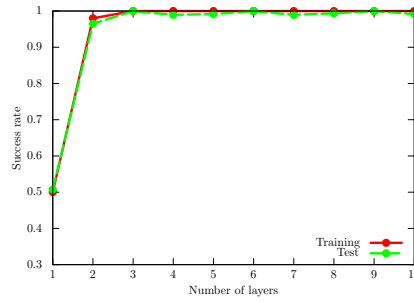


FIG. 14: Performance dependence of QCL on the number of layers L for the iris dataset (0 or 1) in the case of the hinge function, Eq. (F23). We use the CNOT-based circuit geometry and set $\theta_{\text{bias}} = 0$. We iterate the computation 300 times.

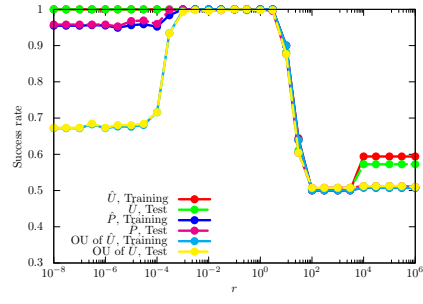


FIG. 15: Performance dependence of the UKM on r , which is the coefficient of the second term in the right-hand side of Eq. (J8) for the iris dataset (0 or 1) in the case of the hinge function, Eq. (F23). We use complex matrices and set $\theta_{\text{bias}} = 0$. We set $K = 30$ and $K' = 10$.

4. Iris dataset (0 or non-0)

We here show the numerical result for the iris dataset (0 or non-0). For the UKM, we put $r = 0.010$ and set $K = 30$ and $K' = 10$ in Algo. 11. For QCL, we run iterations 300 times.

In Fig. 16, we show the numerical results of QCL for the 5-fold datasets with 5 different random seeds. In Fig. 17,

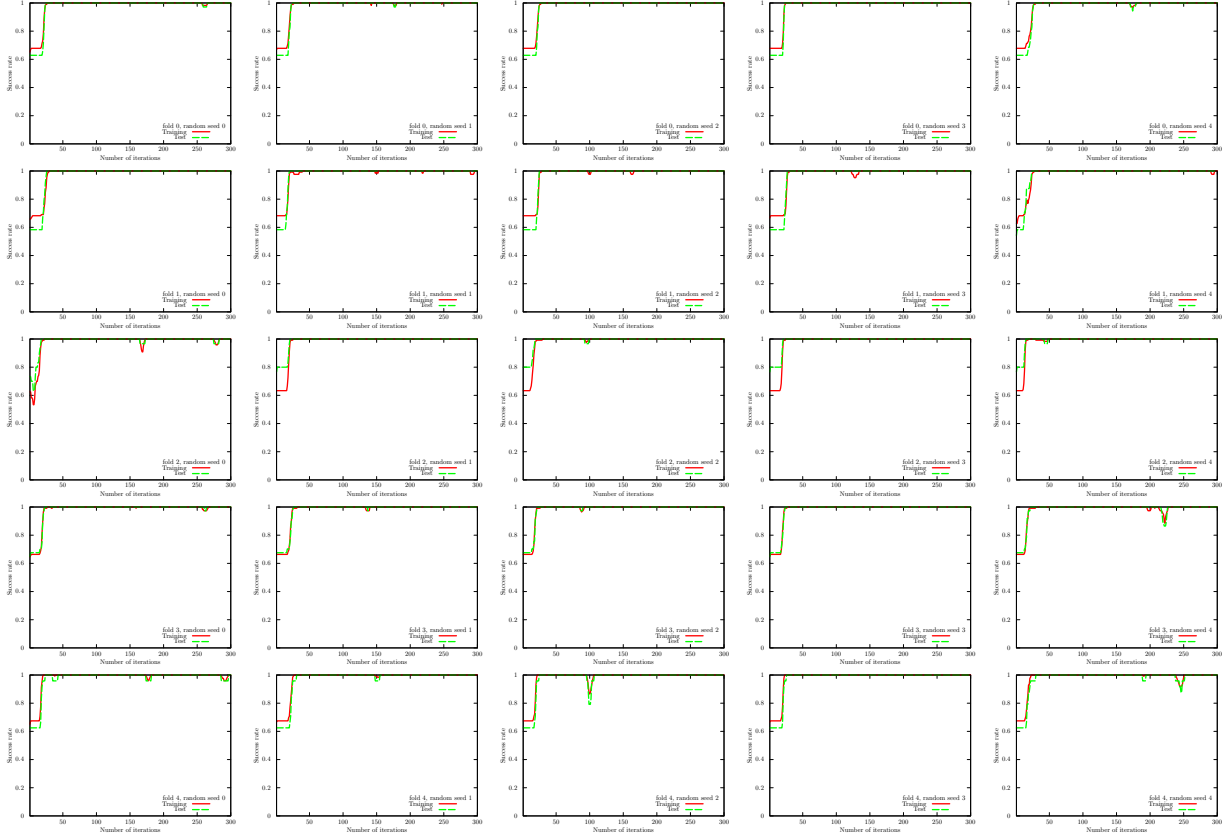


FIG. 16: Results of QCL on the 5-fold datasets with 5 different random seeds for the iris dataset (0 or non-0). We use the CNOT-based circuit and set $\theta_{\text{bias}} = 0$. The number of layers L is set to 5.

we show the numerical results of \hat{P} of the UKM for the 5-fold datasets with 5 different random seeds. In Fig. 18, we also show the numerical results of OU of \hat{X} of the UKM for the 5-fold datasets with 5 different random seeds.

We summarize the results of 5-fold CV with 5 different random seeds of QCL and the UKM in Tables X and XI. For QCL and the UKM, we select the best model for the training dataset over iterations to compute the performance.

In Fig. 19, we plot the data shown in Tables X and XI. We also summarize the results of 5-fold CV with 5 different

Algo.	Condition	Training	Test
QCL	CNOT-based, w/o bias	1.0	1.0
QCL	CNOT-based, w/ bias	1.0	1.0
QCL	CRot-based, w/o bias	1.0	1.0
QCL	CRot-based, w/ bias	1.0	1.0
QCL	1d Heisenberg, w/o bias	1.0	0.9957
QCL	1d Heisenberg, w/ bias	1.0	0.9920
QCL	FC Heisenberg, w/o bias	1.0	0.9957
QCL	FC Heisenberg, w/ bias	1.0	0.9920

TABLE X: Results of 5-fold CV with 5 different random seeds of QCL for the iris dataset (0 or non-0). The number of layers L is set to 5 and the number of iterations is set to 300.

random seeds of the kernel method in Table XII. More specifically, we use Ridge classification in Sec. G 2. We consider the linear functions and the second-order polynomial functions for $\phi(\cdot)$ in Eq. (G8) with and without normalization.

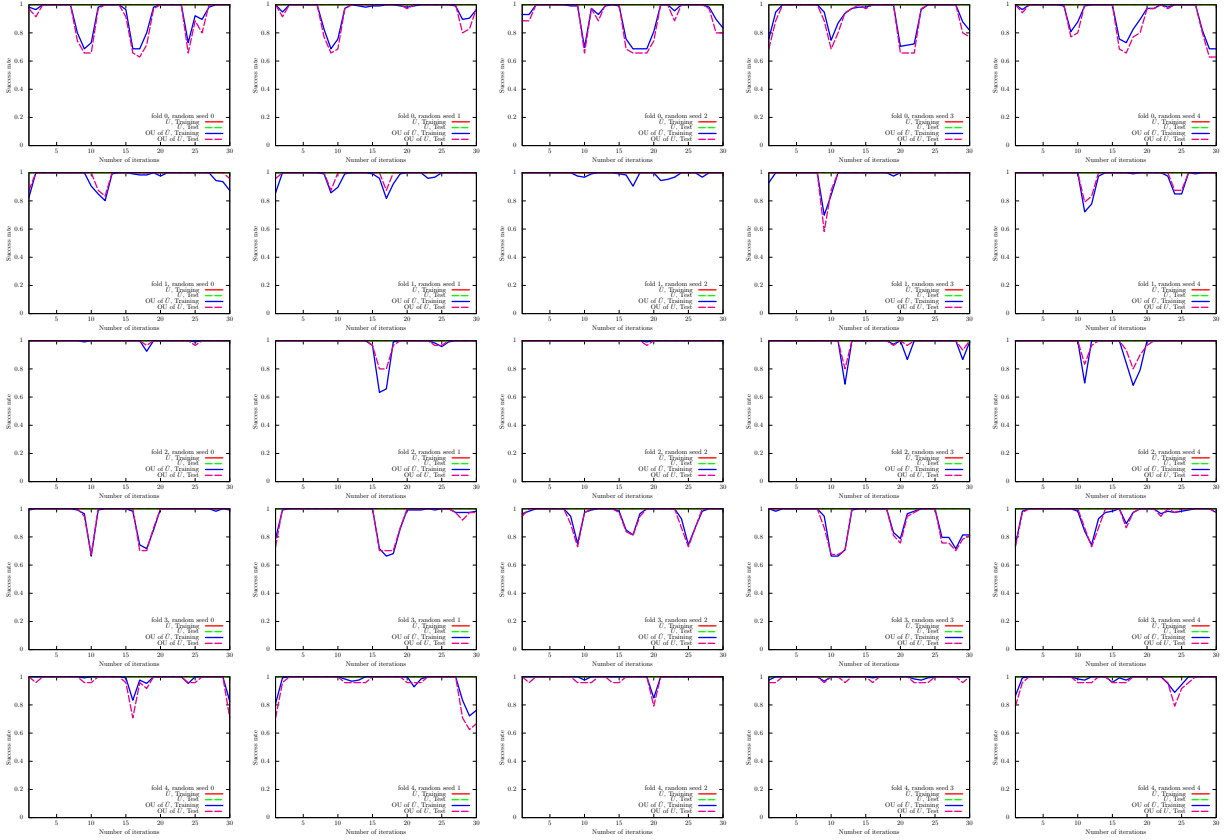


FIG. 17: Results of the UKM (\hat{X} and \hat{P}) on the 5-fold datasets with 5 different random seeds for the iris dataset (0 or non-0). We use complex matrices and set $\theta_{\text{bias}} = 0$. We set $r = 0.010$.

Algo.	Condition	Training	Test
UKM	\hat{X} , complex, w/o bias	1.0	1.0
UKM	\hat{P} , complex, w/o bias	1.0	0.9917
UKM	OU of \hat{X} , complex, w/o bias	1.0	1.0
UKM	\hat{X} , complex, w/ bias	1.0	1.0
UKM	\hat{P} , complex, w/ bias	1.0	0.9987
UKM	OU of \hat{X} , complex, w/ bias	1.0	0.9987
UKM	\hat{X} , real, w/o bias	1.0	1.0
UKM	\hat{P} , real, w/o bias	1.0	0.9917
UKM	OU of \hat{X} , real, w/o bias	1.0	1.0
UKM	\hat{X} , real, w/ bias	1.0	1.0
UKM	\hat{P} , real, w/ bias	1.0	0.9970
UKM	OU of \hat{X} , real, w/ bias	1.0	0.9970

TABLE XI: Results of 5-fold CV with 5 different random seeds of the UKM for the iris dataset (0 or non-0). We put $r = 0.010$ and set $K = 30$ and $K' = 10$.

We set $\lambda = 10^{-2}, 10^{-1}, 1$ where λ is the coefficient of the regularization term.

Next, we show the performance dependence of the three algorithms on their key parameters. We see the performance dependence of QCL on the number of layers L . The result is shown in Fig. 20. We then see the performance dependence of the UKM on r , which is the coefficient of the second term in the right-hand side of Eq. (J8). The result is shown in Fig. 21. In Fig. 22, we show the performance dependence of the kernel method on λ , which is the coefficient of the second term in the right-hand side of Eq. (G11).

So far, we have used the squared error function, Eq. (F22). In Fig. 23, we show the performance dependence of QCL on the number of layers L in the case of the hinge function, Eq. (F23). In Fig. 24, we show the performance

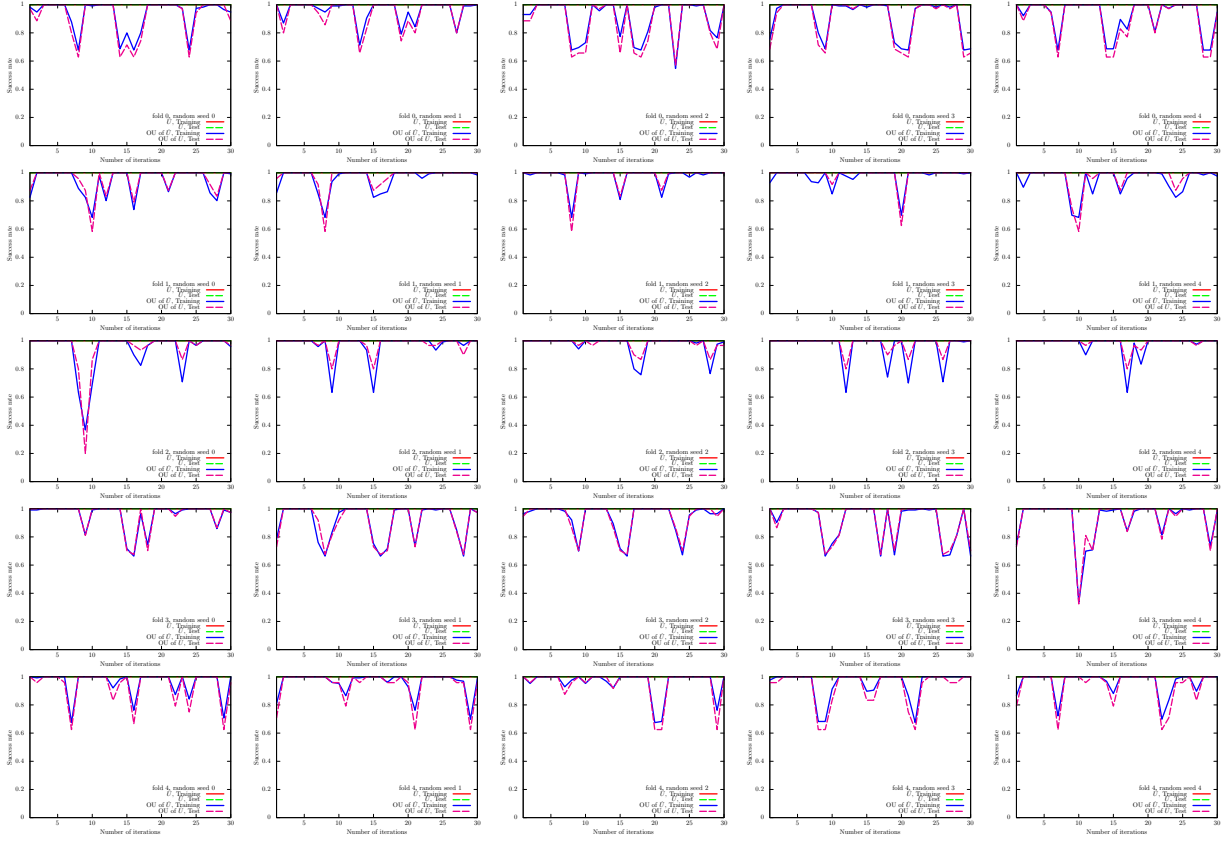


FIG. 18: Results of the UKM (\hat{X} and OU of \hat{X}) on the 5-fold datasets with 5 different random seeds for the iris dataset (0 or non-0). We use complex matrices and set $\theta_{\text{bias}} = 0$. We set $r = 0.010$.

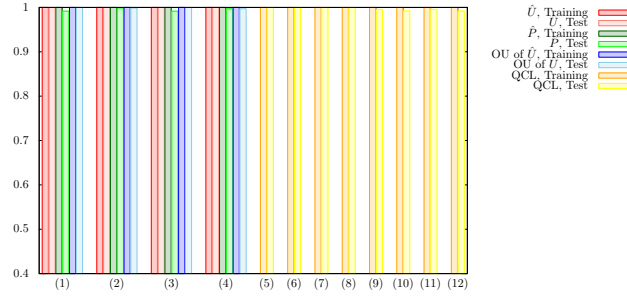


FIG. 19: Results of 5-fold CV with 5 different random seeds for the iris dataset (0 or non-0). For the UKM, we put $r = 0.010$ and set $K = 30$ and $K' = 10$. For QCL, the number of layers L is 5 and the number of iterations is 300. The numerical settings are as follows: (1) complex matrices without the bias term, (2) complex matrices with the bias term, (3) real matrices without the bias term, (4) real matrices with the bias term, (5) CNOT-based circuit without the bias term, (6) CNOT-based circuit with the bias term, (7) CRot-based circuit without the bias term, (8) CRot-based circuit with the bias term, (9) 1d Heisenberg circuit without the bias term, (10) 1d Heisenberg circuit with the bias term, (11) FC Heisenberg circuit without the bias term, and (12) FC Heisenberg circuit with the bias term.

dependence of the UKM on r , which is the coefficient of the second term in the right-hand side of Eq. (J8), in the case of the hinge function, Eq. (F23).

Algo.	Condition	Training	Test
Kernel method	Linear, w/o normalization, $\lambda = 10^{-2}$	1.0000	1.0000
Kernel method	Linear, w/o normalization, $\lambda = 10^{-1}$	1.0000	1.0000
Kernel method	Linear, w/o normalization, $\lambda = 1$	1.0000	1.0000
Kernel method	Linear, w/ normalization, $\lambda = 10^{-2}$	1.0000	1.0000
Kernel method	Linear, w/ normalization, $\lambda = 10^{-1}$	1.0000	1.0000
Kernel method	Linear, w/ normalization, $\lambda = 1$	1.0000	1.0000
Kernel method	Poly-2, w/o normalization, $\lambda = 10^{-2}$	1.0000	1.0000
Kernel method	Poly-2, w/o normalization, $\lambda = 10^{-1}$	1.0000	1.0000
Kernel method	Poly-2, w/o normalization, $\lambda = 1$	1.0000	1.0000
Kernel method	Poly-2, w/ normalization, $\lambda = 10^{-2}$	1.0000	1.0000
Kernel method	Poly-2, w/ normalization, $\lambda = 10^{-1}$	1.0000	1.0000
Kernel method	Poly-2, w/ normalization, $\lambda = 1$	1.0000	1.0000

TABLE XII: Results of 5-fold CV with 5 different random seeds of the kernel method for the iris dataset (0 or non-0).

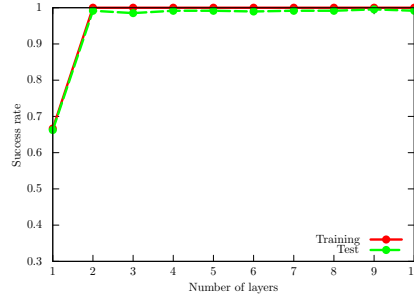


FIG. 20: Performance dependence of QCL on the number of layers L for the iris dataset (0 or non-0). We use the CNOT-based circuit geometry and set $\theta_{\text{bias}} = 0$. We iterate the computation 300 times.

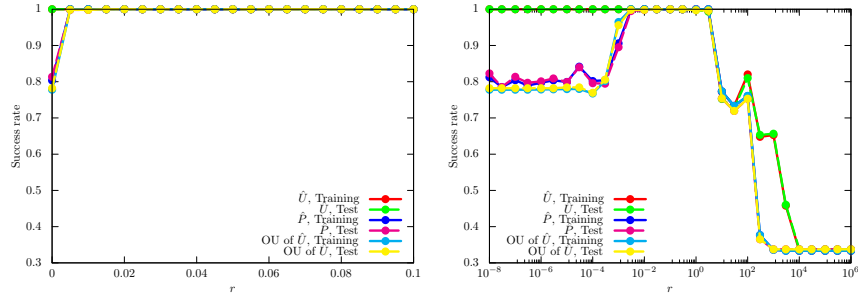


FIG. 21: Performance dependence of the UKM on r , which is the coefficient of the second term in the right-hand side of Eq. (J8) for the iris dataset (0 or non-0). We use complex matrices and set $\theta_{\text{bias}} = 0$. We set $K = 30$ and $K' = 10$.

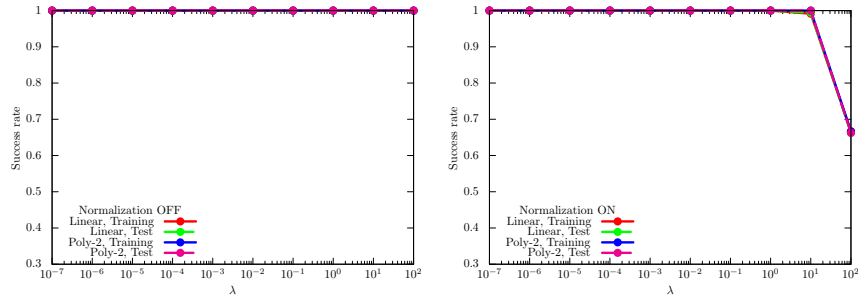


FIG. 22: Performance dependence of the kernel method on λ , which is the coefficient of the second term in the right-hand side of Eq. (G11) for the iris dataset (0 or non-0). For $\phi(\cdot)$ in Eq. (G8), we use the linear functions and the second-degree polynomial functions with and without normalization.

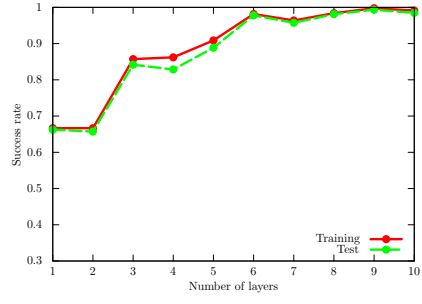


FIG. 23: Performance dependence of QCL on the number of layers L for the iris dataset (0 or non-0) in the case of the hinge function, Eq. (F23). We use the CNOT-based circuit geometry and set $\theta_{\text{bias}} = 0$. We iterate the computation 300 times.

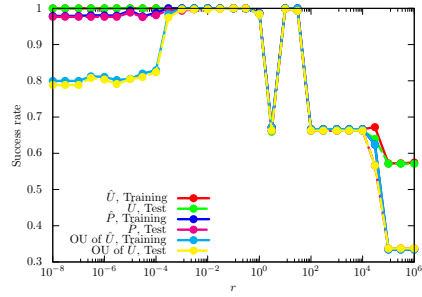


FIG. 24: Performance dependence of the UKM on r , which is the coefficient of the second term in the right-hand side of Eq. (J8) for the iris dataset (0 or non-0) in the case of the hinge function, Eq. (F23). We use complex matrices and set $\theta_{\text{bias}} = 0$. We set $K = 30$ and $K' = 10$.

5. Iris dataset (1 or non-1)

We here show the numerical result for the iris dataset (1 or non-1). For the UKM, we put $r = 0.010$ and set $K = 30$ and $K' = 10$ in Algo. 11. For QCL, we run iterations 300 times.

In Fig. 25, we show the numerical results of QCL for the 5-fold datasets with 5 different random seeds. In Fig. 26,

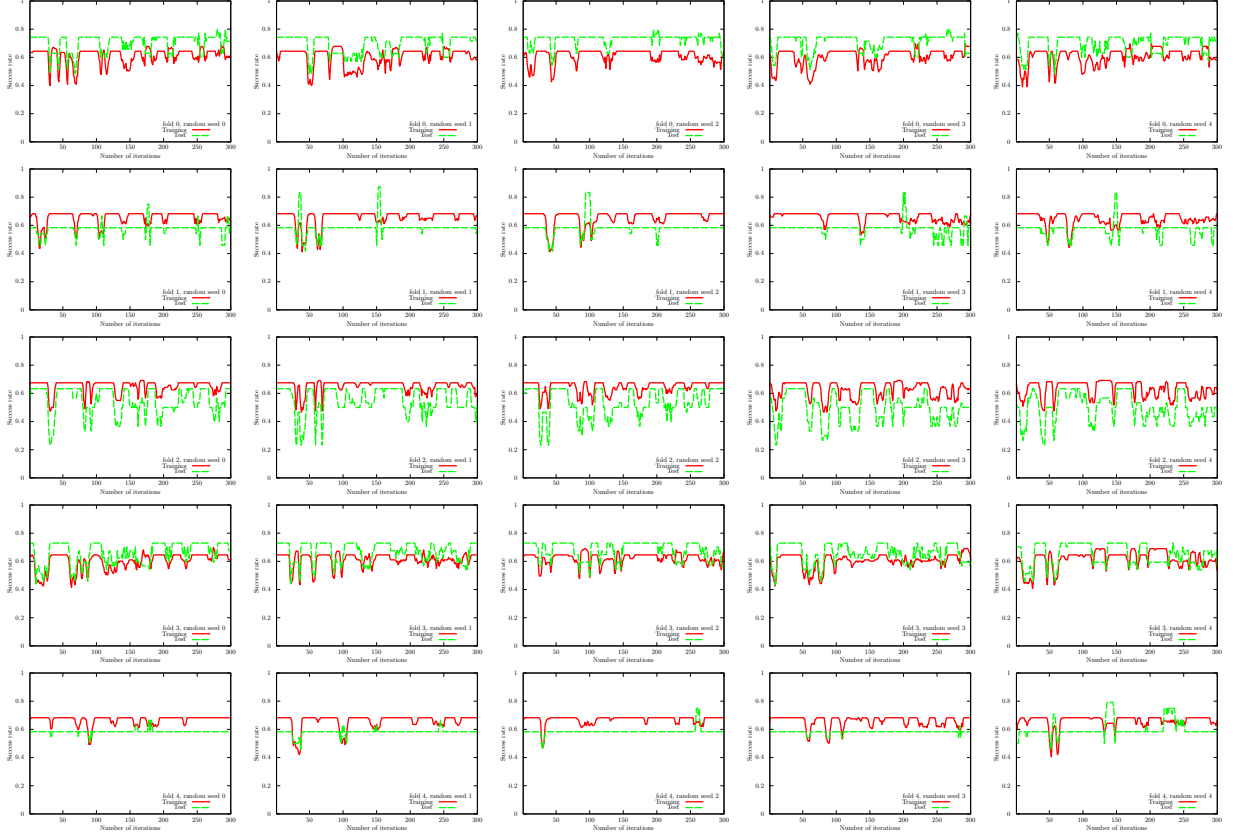


FIG. 25: Results of QCL on the 5-fold datasets with 5 different random seeds for the iris dataset (1 or non-1). We use the CNOT-based circuit and set $\theta_{\text{bias}} = 0$. The number of layers L is set to 5.

we show the numerical results of \hat{P} of the UKM for the 5-fold datasets with 5 different random seeds. In Fig. 27, we also show the numerical results of OU of \hat{X} of the UKM for the 5-fold datasets with 5 different random seeds.

We summarize the results of 5-fold CV with 5 different random seeds of QCL and the UKM in Tables XIII and XIV, respectively. For QCL and the UKM, we select the best model for the training dataset over iterations to compute the performance. In Fig. 28, we plot the data shown in Tables XIII and XIV. We also summarize the results of 5-fold

Algo.	Condition	Training	Test
QCL	CNOT-based, w/o bias	0.6851	0.5845
QCL	CNOT-based, w/ bias	0.6919	0.5854
QCL	CRot-based, w/o bias	0.6840	0.5793
QCL	CRot-based, w/ bias	0.6847	0.5793
QCL	1d Heisenberg, w/o bias	0.6760	0.6004
QCL	1d Heisenberg, w/ bias	0.6801	0.5872
QCL	FC Heisenberg, w/o bias	0.6760	0.6004
QCL	FC Heisenberg, w/ bias	0.6801	0.5872

TABLE XIII: Results of 5-fold CV with 5 different random seeds of QCL for the iris dataset (1 or non-1). The number of layers L is set to 5 and the number of iterations is set to 300.

CV with 5 different random seeds of the kernel method in Table XV. More specifically, we use Ridge classification in Sec. G2. We consider the linear functions and the second-order polynomial functions for $\phi(\cdot)$ in Eq. (G8) with and

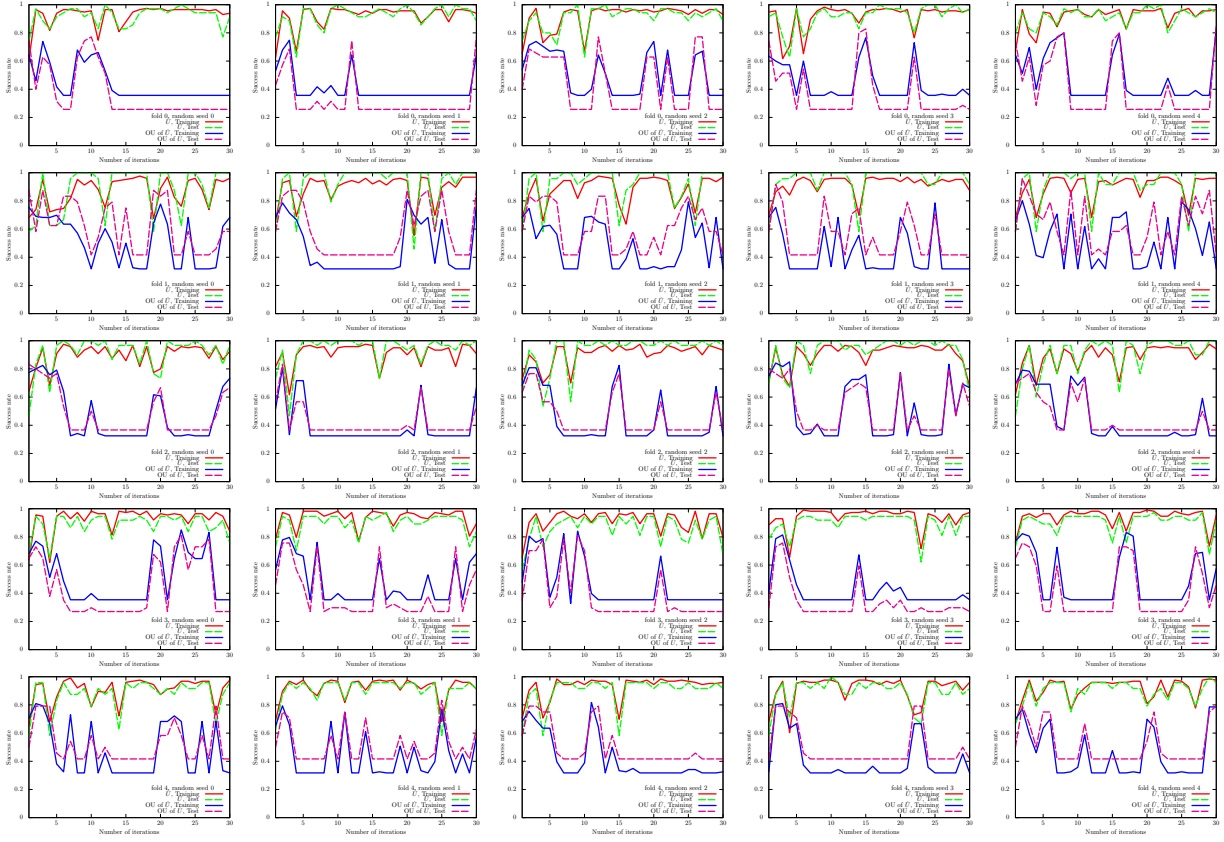


FIG. 26: Results of the UKM (\hat{X} and \hat{P}) on the 5-fold datasets with 5 different random seeds for the iris dataset (1 or non-1). We use complex matrices and set $\theta_{\text{bias}} = 0$. We set $r = 0.010$.

Algo.	Condition	Training	Test
UKM	\hat{X} , complex, w/o bias	0.9781	0.9618
UKM	\hat{P} , complex, w/o bias	0.7873	0.7781
UKM	OU of \hat{X} , complex, w/o bias	0.7953	0.7994
UKM	\hat{X} , complex, w/ bias	0.9712	0.9581
UKM	\hat{P} , complex, w/ bias	0.6744	0.6564
UKM	OU of \hat{X} , complex, w/ bias	0.6734	0.6507
UKM	\hat{X} , real, w/o bias	0.9778	0.9717
UKM	\hat{P} , real, w/o bias	0.7880	0.7789
UKM	OU of \hat{X} , real, w/o bias	0.7869	0.7713
UKM	\hat{X} , real, w/ bias	0.9702	0.9569
UKM	\hat{P} , real, w/ bias	0.6746	0.6568
UKM	OU of \hat{X} , real, w/ bias	0.6794	0.6640

TABLE XIV: Results of 5-fold CV with 5 different random seeds of the UKM for the iris dataset (1 or non-1). We put $r = 0.010$ and set $K = 30$ and $K' = 10$.

without normalization. We set $\lambda = 10^{-2}, 10^{-1}, 1$ where λ is the coefficient of the regularization term.

Next, we show the performance dependence of the three algorithms on their key parameters. We see the performance dependence of QCL on the number of layers L . The result is shown in Fig. 29. We then see the performance dependence of the UKM on r , which is the coefficient of the second term in the right-hand side of Eq. (J8). The result is shown in Fig. 30. In Fig. 31, we show the performance dependence of the kernel method on λ , which is the coefficient of the second term in the right-hand side of Eq. (G11).

So far, we have used the squared error function, Eq. (F22). In Fig. 32, we show the performance dependence of QCL on the number of layers L in the case of the hinge function, Eq. (F23). In Fig. 33, we show the performance

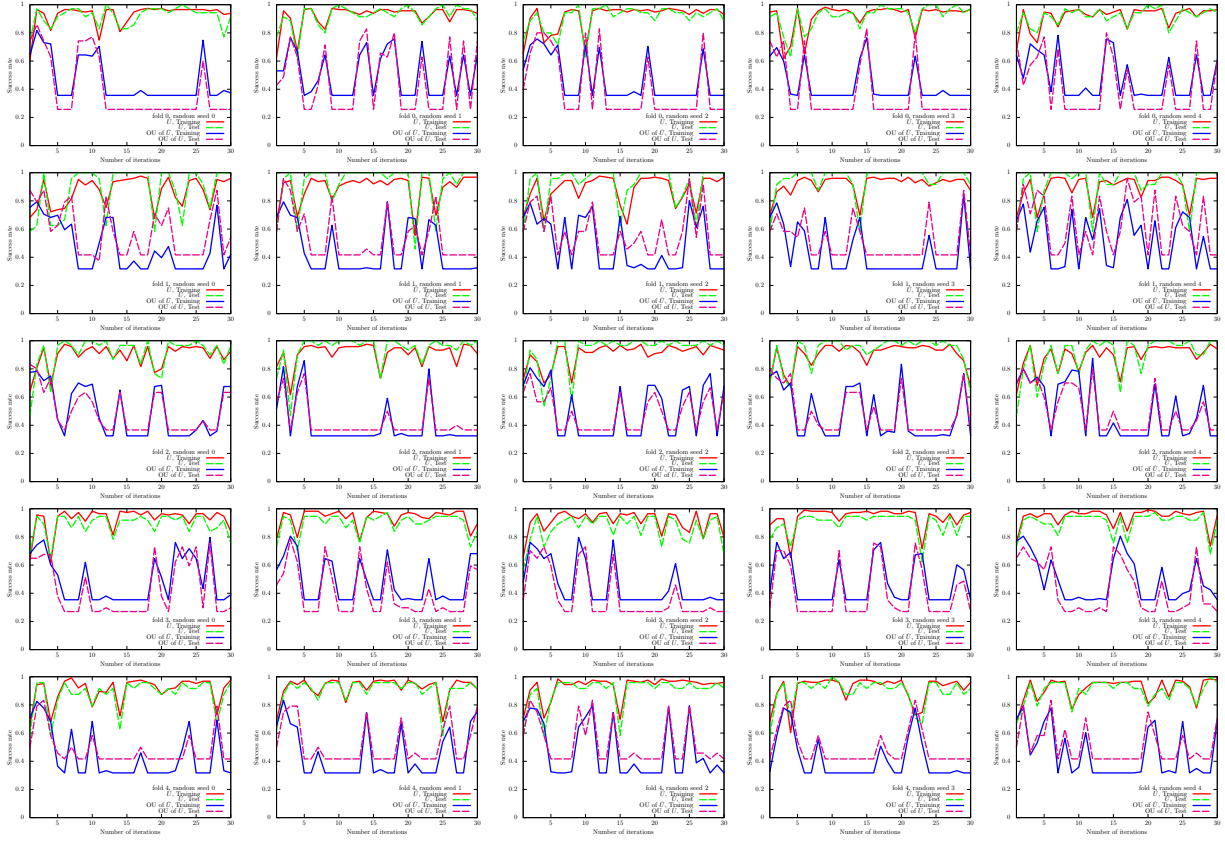


FIG. 27: Results of the UKM (\hat{X} and OU of \hat{X}) on the 5-fold datasets with 5 different random seeds for the iris dataset (1 or non-1). We use complex matrices and set $\theta_{\text{bias}} = 0$. We set $r = 0.010$.

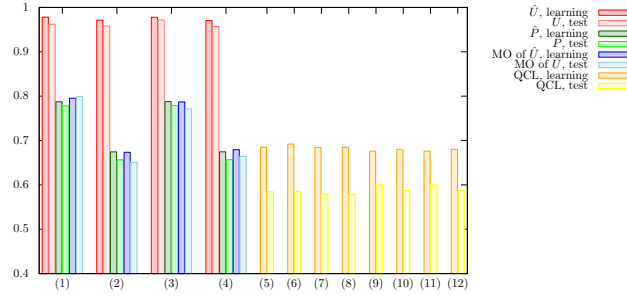


FIG. 28: Results of 5-fold CV with 5 different random seeds for the iris dataset (1 or non-1). For the UKM, we put $r = 0.010$ and set $K = 30$ and $K' = 10$. For QCL, the number of layers L is 5 and the number of iterations is 300. The numerical settings are as follows: (1) complex matrices without the bias term, (2) complex matrices with the bias term, (3) real matrices without the bias term, (4) real matrices with the bias term, (5) CNOT-based circuit without the bias term, (6) CNOT-based circuit with the bias term, (7) CRot-based circuit without the bias term, (8) CRot-based circuit with the bias term, (9) 1d Heisenberg circuit without the bias term, (10) 1d Heisenberg circuit with the bias term, (11) FC Heisenberg circuit without the bias term, and (12) FC Heisenberg circuit with the bias term.

dependence of the UKM on r , which is the coefficient of the second term in the right-hand side of Eq. (J8), in the case of the hinge function, Eq. (F23).

Algo.	Condition	Training	Test
Kernel method	Linear, w/o normalization, $\lambda = 10^{-2}$	0.7463	0.7378
Kernel method	Linear, w/o normalization, $\lambda = 10^{-1}$	0.7445	0.7324
Kernel method	Linear, w/o normalization, $\lambda = 1$	0.7426	0.7240
Kernel method	Linear, w/ normalization, $\lambda = 10^{-2}$	0.9401	0.9561
Kernel method	Linear, w/ normalization, $\lambda = 10^{-1}$	0.7697	0.7276
Kernel method	Linear, w/ normalization, $\lambda = 1$	0.6382	0.6113
Kernel method	Poly-2, w/o normalization, $\lambda = 10^{-2}$	0.9751	0.9666
Kernel method	Poly-2, w/o normalization, $\lambda = 10^{-1}$	0.9733	0.9558
Kernel method	Poly-2, w/o normalization, $\lambda = 1$	0.9684	0.9558
Kernel method	Poly-2, w/ normalization, $\lambda = 10^{-2}$	0.9601	0.9601
Kernel method	Poly-2, w/ normalization, $\lambda = 10^{-1}$	0.9253	0.9312
Kernel method	Poly-2, w/ normalization, $\lambda = 1$	0.6778	0.6475

TABLE XV: Results of 5-fold CV with 5 different random seeds of the kernel method for the iris dataset (1 or non-1).

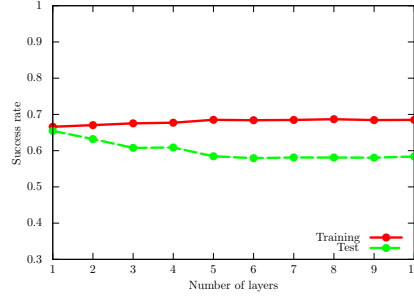


FIG. 29: Performance dependence of QCL on the number of layers L for the iris dataset (1 or non-1). We use the CNOT-based circuit geometry and set $\theta_{\text{bias}} = 0$. We iterate the computation 300 times.

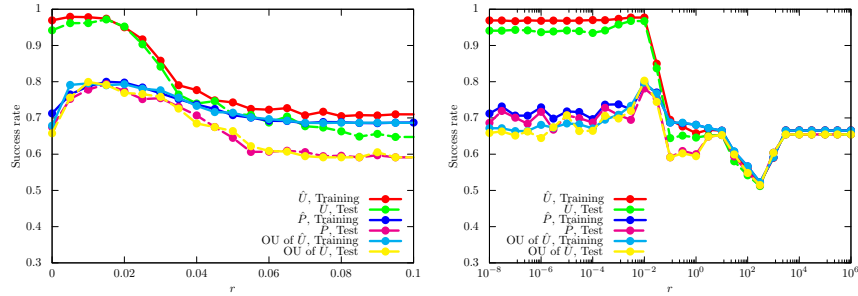


FIG. 30: Performance dependence of the UKM on r , which is the coefficient of the second term in the right-hand side of Eq. (J8) for the iris dataset (1 or non-1). We use complex matrices and set $\theta_{\text{bias}} = 0$. We set $K = 30$ and $K' = 10$.

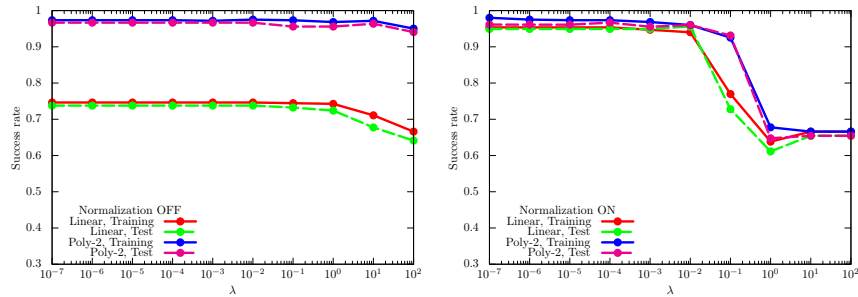


FIG. 31: Performance dependence of the kernel method on λ , which is the coefficient of the second term in the right-hand side of Eq. (G11) for the iris dataset (1 or non-1). For $\phi(\cdot)$ in Eq. (G8), we use the linear functions and the second-degree polynomial functions with and without normalization.

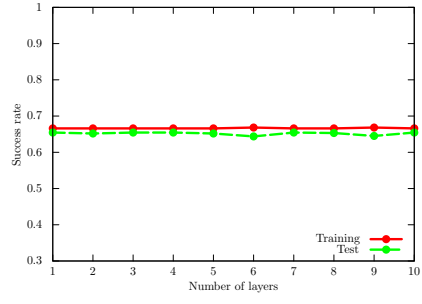


FIG. 32: Performance dependence of QCL on the number of layers L for the iris dataset (1 or non-1) in the case of the hinge function, Eq. (F23). We use the CNOT-based circuit geometry and set $\theta_{\text{bias}} = 0$. We iterate the computation 300 times.

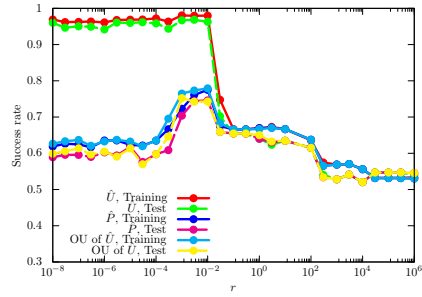


FIG. 33: Performance dependence of the UKM on r , which is the coefficient of the second term in the right-hand side of Eq. (J8) for the iris dataset (1 or non-1) in the case of the hinge function, Eq. (F23). We use complex matrices and set $\theta_{\text{bias}} = 0$. We set $K = 30$ and $K' = 10$.

6. Cancer dataset (0 or 1)

We here show the numerical result for the cancer dataset (0 or 1). For the UKM, we put $r = 0.010$ and set $K = 30$ and $K' = 10$ in Algo. 11. For QCL, we run iterations 300 times.

In Fig. 34, we show the numerical results of QCL for the 5-fold datasets with 5 different random seeds. In Fig. 35,

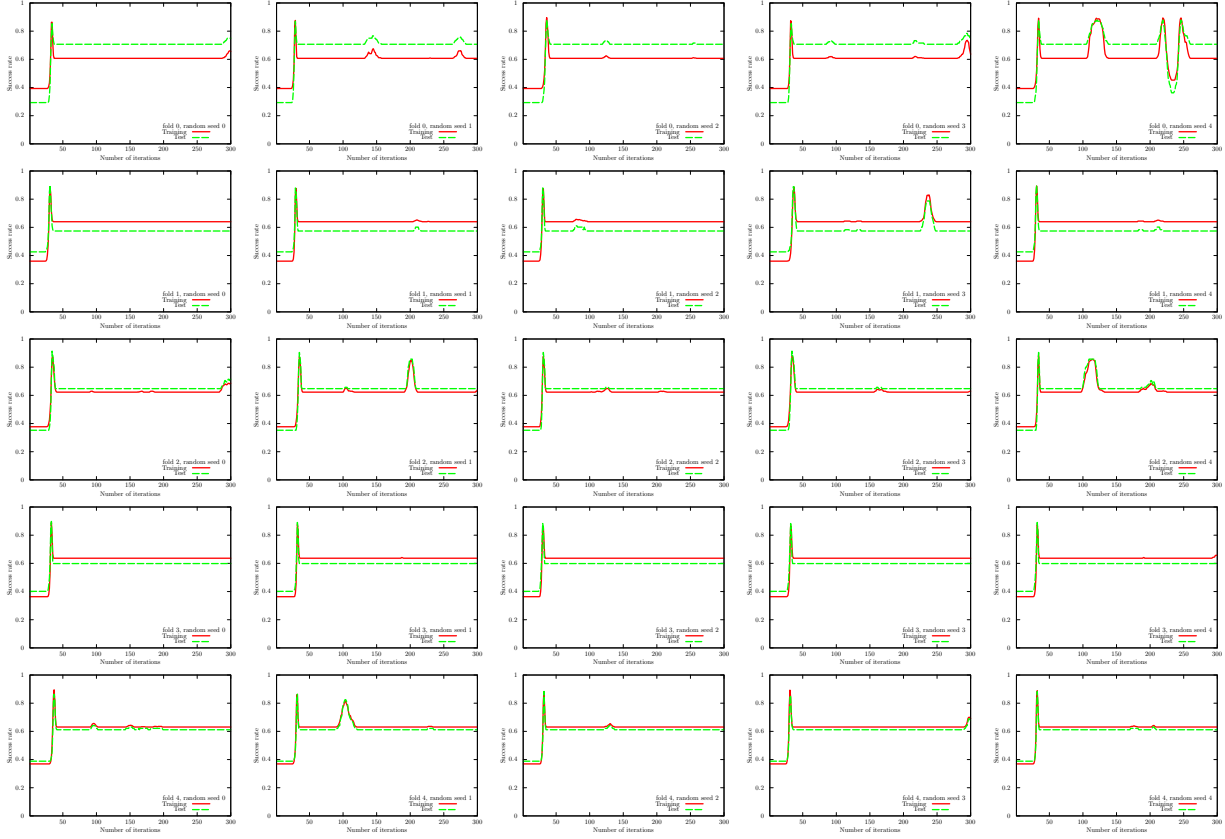


FIG. 34: Results of QCL on the 5-fold datasets with 5 different random seeds for the cancer dataset (0 or 1). We use the CNOT-based circuit and set $\theta_{\text{bias}} = 0$. The number of layers L is set to 5.

we show the numerical results of \hat{P} of the UKM for the 5-fold datasets with 5 different random seeds. In Fig. 36, we also show the numerical results of OU of \hat{X} of the UKM for the 5-fold datasets with 5 different random seeds.

We summarize the results of 5-fold CV with 5 different random seeds of QCL and the UKM in Tables XVI and XVII, respectively. For QCL and the UKM, we select the best model for the training dataset over iterations to compute the performance. In Fig. 37, we plot the data shown in Tables XVI and XVII. We also summarize the results of 5-fold

Algo.	Condition	Training	Test
QCL	CNOT-based, w/o bias	0.8797	0.8768
QCL	CNOT-based, w/ bias	0.8597	0.8577
QCL	CRot-based, w/o bias	0.7866	0.7752
QCL	CRot-based, w/ bias	0.8085	0.8052
QCL	1d Heisenberg, w/o bias	0.6568	0.6512
QCL	1d Heisenberg, w/ bias	0.7515	0.7427
QCL	FC Heisenberg, w/o bias	0.7435	0.7444
QCL	FC Heisenberg, w/ bias	0.7744	0.7789

TABLE XVI: Results of 5-fold CV with 5 different random seeds of QCL for the cancer dataset (0 or 1). The number of layers L is set to 5 and the number of iterations is set to 300.

CV with 5 different random seeds of the kernel method in Table XVIII. More specifically, we use Ridge classification in Sec. G 2. We consider the linear functions and the second-order polynomial functions for $\phi(\cdot)$ in Eq. (G8) with and

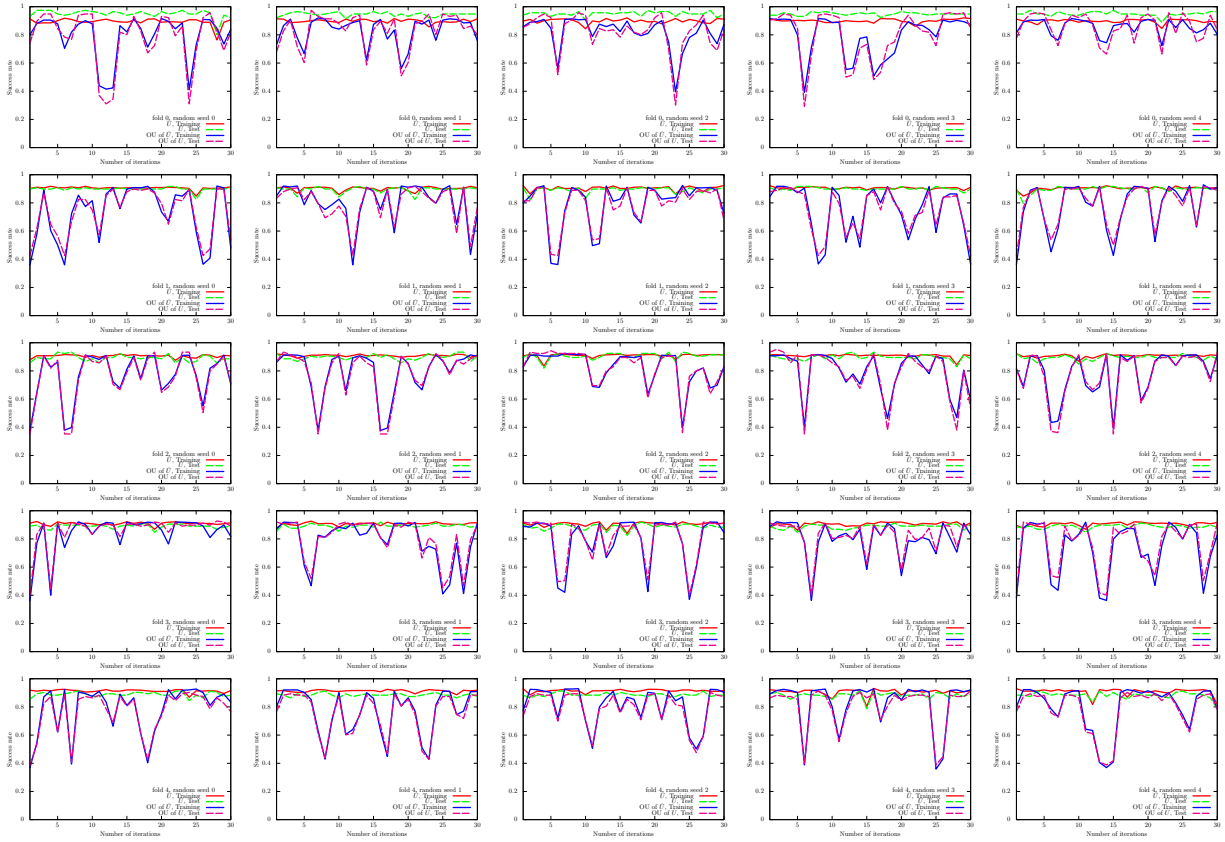


FIG. 35: Results of the UKM (\hat{X} and \hat{P}) on the 5-fold datasets with 5 different random seeds for the cancer dataset (0 or 1). We use complex matrices and set $\theta_{\text{bias}} = 0$. We set $r = 0.010$.

Algo.	Condition	Training	Test
UKM	\hat{X} , complex, w/o bias	0.9219	0.9143
UKM	\hat{P} , complex, w/o bias	0.9204	0.9093
UKM	OU of \hat{X} , complex, w/o bias	0.9184	0.9115
UKM	\hat{X} , complex, w/ bias	0.9207	0.9143
UKM	\hat{P} , complex, w/ bias	0.8870	0.8753
UKM	OU of \hat{X} , complex, w/ bias	0.8912	0.8805
UKM	\hat{X} , real, w/o bias	0.9213	0.9107
UKM	\hat{P} , real, w/o bias	0.9194	0.9131
UKM	OU of \hat{X} , real, w/o bias	0.9170	0.9112
UKM	\hat{X} , real, w/ bias	0.9218	0.9160
UKM	\hat{P} , real, w/ bias	0.7929	0.7879
UKM	OU of \hat{X} , real, w/ bias	0.8107	0.8014

TABLE XVII: Results of 5-fold CV with 5 different random seeds of the UKM for the cancer dataset (0 or 1). We put $r = 0.010$ and set $K = 30$ and $K' = 10$.

without normalization. We set $\lambda = 10^{-2}, 10^{-1}, 1$ where λ is the coefficient of the regularization term.

Next, we show the performance dependence of the three algorithms on their key parameters. We see the performance dependence of QCL on the number of layers L . The result is shown in Fig. 38. We then see the performance dependence of the UKM on r , which is the coefficient of the second term in the right-hand side of Eq. (J8). The result is shown in Fig. 39. In Fig. 40, we show the performance dependence of the kernel method on λ , which is the coefficient of the second term in the right-hand side of Eq. (G11).

So far, we have used the squared error function, Eq. (F22). In Fig. 41, we show the performance dependence of QCL on the number of layers L in the case of the hinge function, Eq. (F23). In Fig. 42, we show the performance

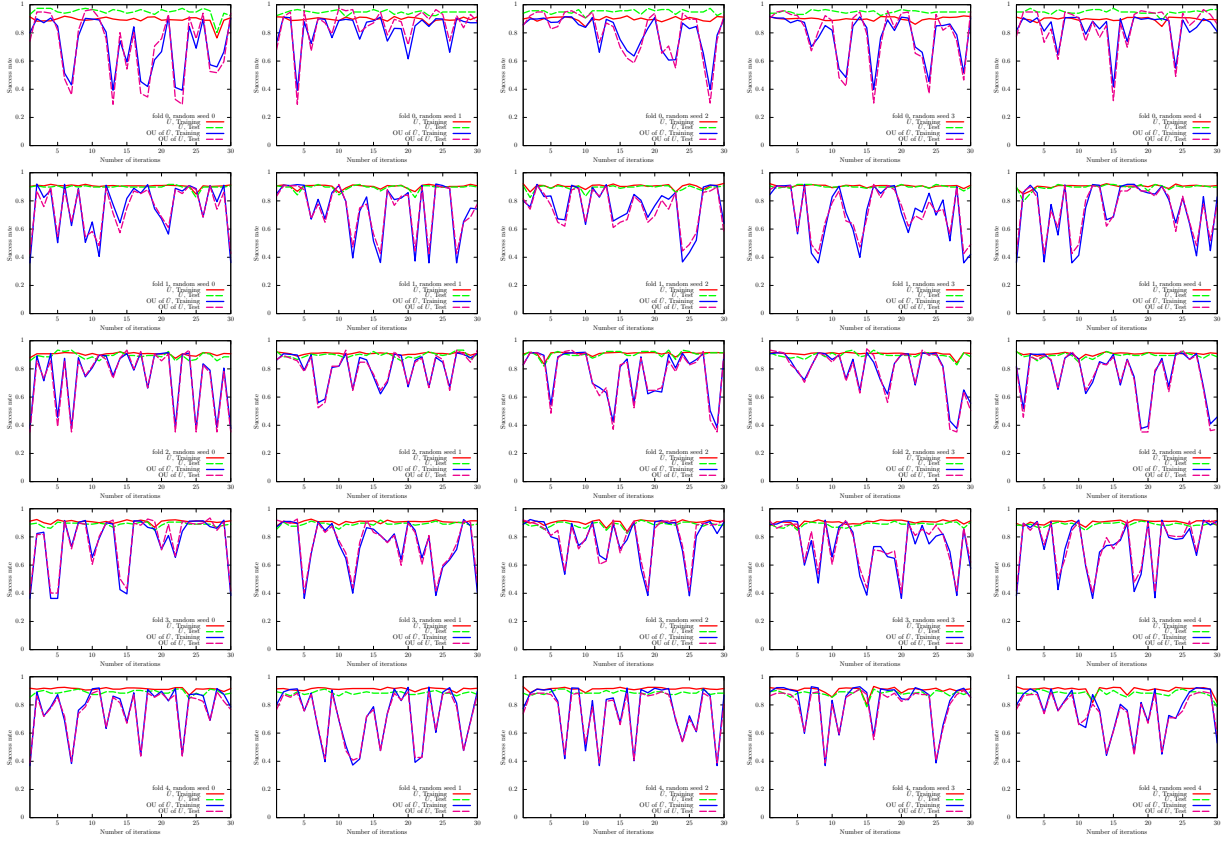


FIG. 36: Results of the UKM (\hat{X} and OU of \hat{X}) on the 5-fold datasets with 5 different random seeds for the cancer dataset (0 or 1). We use complex matrices and set $\theta_{\text{bias}} = 0$. We set $r = 0.010$.

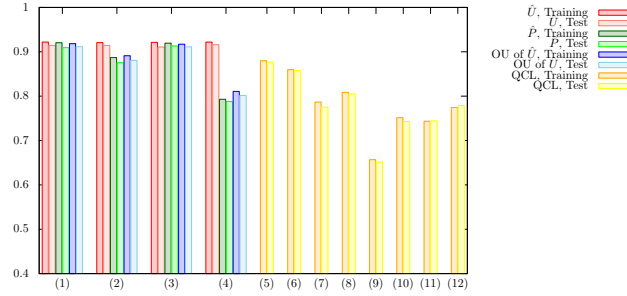


FIG. 37: Results of 5-fold CV with 5 different random seeds for the cancer dataset (0 or 1). For the UKM, we put $r = 0.010$ and set $K = 30$ and $K' = 10$. For QCL, the number of layers L is 5 and the number of iterations is 300. The numerical settings are as follows: (1) complex matrices without the bias term, (2) complex matrices with the bias term, (3) real matrices without the bias term, (4) real matrices with the bias term, (5) CNOT-based circuit without the bias term, (6) CNOT-based circuit with the bias term, (7) CRot-based circuit without the bias term, (8) CRot-based circuit with the bias term, (9) 1d Heisenberg circuit without the bias term, (10) 1d Heisenberg circuit with the bias term, (11) FC Heisenberg circuit without the bias term, and (12) FC Heisenberg circuit with the bias term.

dependence of the UKM on r , which is the coefficient of the second term in the right-hand side of Eq. (J8), in the case of the hinge function, Eq. (F23).

Algo.	Condition	Training	Test
Kernel method	Linear, w/o normalization, $\lambda = 10^{-2}$	0.9618	0.9568
Kernel method	Linear, w/o normalization, $\lambda = 10^{-1}$	0.9623	0.9549
Kernel method	Linear, w/o normalization, $\lambda = 1$	0.9591	0.9495
Kernel method	Linear, w/ normalization, $\lambda = 10^{-2}$	0.9262	0.9247
Kernel method	Linear, w/ normalization, $\lambda = 10^{-1}$	0.9205	0.9176
Kernel method	Linear, w/ normalization, $\lambda = 1$	0.8830	0.8812
Kernel method	Poly-2, w/o normalization, $\lambda = 10^{-2}$	0.9242	0.8491
Kernel method	Poly-2, w/o normalization, $\lambda = 10^{-1}$	0.9936	0.9361
Kernel method	Poly-2, w/o normalization, $\lambda = 1$	0.9907	0.9454
Kernel method	Poly-2, w/ normalization, $\lambda = 10^{-2}$	0.9298	0.9264
Kernel method	Poly-2, w/ normalization, $\lambda = 10^{-1}$	0.9210	0.9195
Kernel method	Poly-2, w/ normalization, $\lambda = 1$	0.9038	0.9052

TABLE XVIII: Results of 5-fold CV with 5 different random seeds of the kernel method for the cancer dataset (0 or 1).

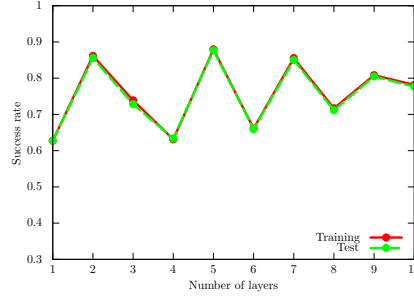


FIG. 38: Performance dependence of QCL on the number of layers L for the cancer dataset (0 or 1). We use the CNOT-based circuit geometry and set $\theta_{\text{bias}} = 0$. We iterate the computation 300 times.

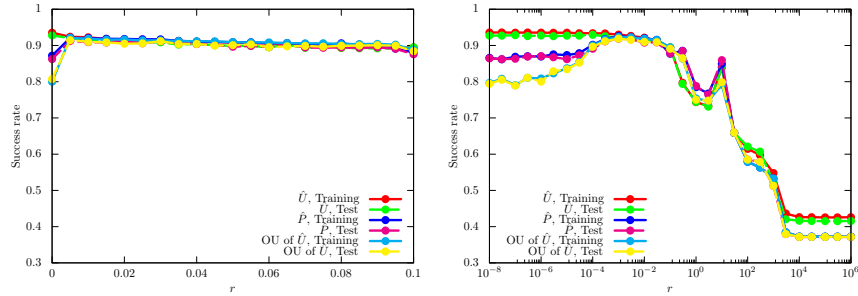


FIG. 39: Performance dependence of the UKM on r , which is the coefficient of the second term in the right-hand side of Eq. (J8) for the cancer dataset (0 or 1). We use complex matrices and set $\theta_{\text{bias}} = 0$. We set $K = 30$ and $K' = 10$.

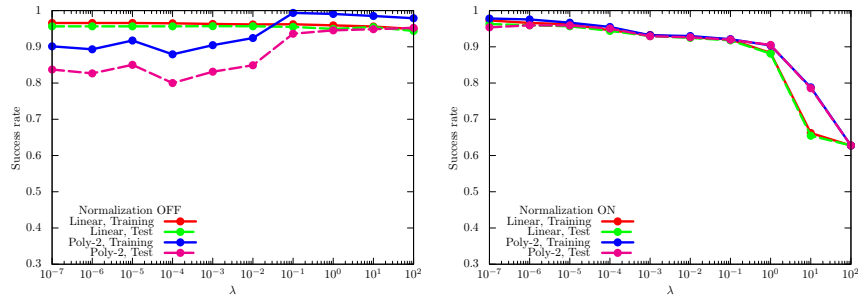


FIG. 40: Performance dependence of the kernel method on λ , which is the coefficient of the second term in the right-hand side of Eq. (G11) for the cancer dataset (0 or 1). For $\phi(\cdot)$ in Eq. (G8), we use the linear functions and the second-degree polynomial functions with and without normalization.

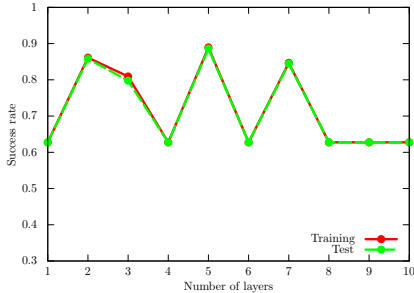


FIG. 41: Performance dependence of QCL on the number of layers L for the cancer dataset (0 or 1) in the case of the hinge function, Eq. (F23). We use the CNOT-based circuit geometry and set $\theta_{\text{bias}} = 0$. We iterate the computation 300 times.

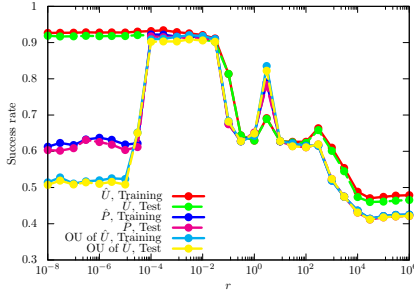


FIG. 42: Performance dependence of the UKM on r , which is the coefficient of the second term in the right-hand side of Eq. (J8) for the cancer dataset (0 or 1) in the case of the hinge function, Eq. (F23). We use complex matrices and set $\theta_{\text{bias}} = 0$. We set $K = 30$ and $K' = 10$.

7. Sonar dataset (0 or 1)

We here show the numerical result for the sonar dataset (0 or 1). For the UKM, we put $r = 0.010$ and set $K = 30$ and $K' = 10$ in Algo. 11. For QCL, we run iterations 300 times.

In Fig. 43, we show the numerical results of QCL for the 5-fold datasets with 5 different random seeds. In Fig. 44,

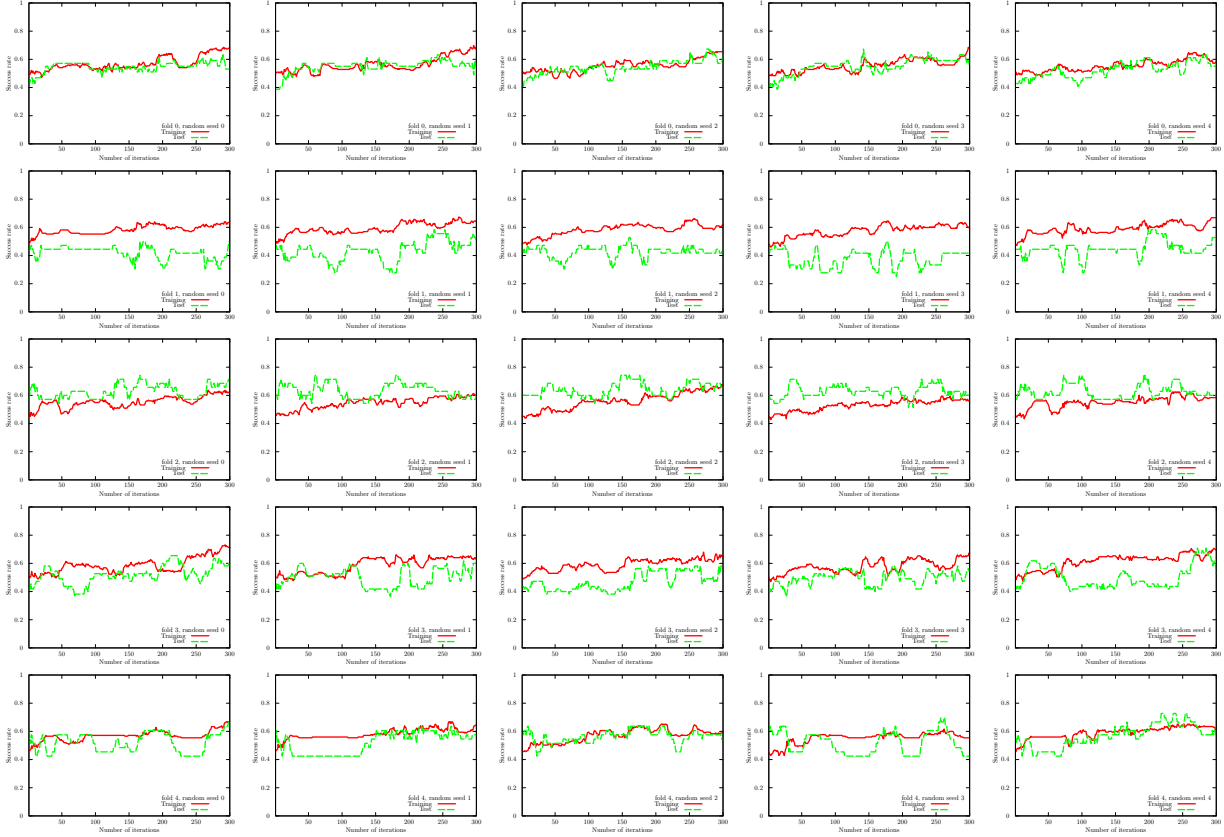


FIG. 43: Results of QCL on the 5-fold datasets with 5 different random seeds for the sonar dataset (0 or 1). We use the CNOT-based circuit and set $\theta_{\text{bias}} = 0$. The number of layers L is set to 5.

we show the numerical results of \hat{P} of the UKM for the 5-fold datasets with 5 different random seeds. In Fig. 45, we also show the numerical results of OU of \hat{X} of the UKM for the 5-fold datasets with 5 different random seeds.

We summarize the results of 5-fold CV with 5 different random seeds of QCL and the UKM in Tables XIX and XX, respectively. For QCL and the UKM, we select the best model for the training dataset over iterations to compute the performance. In Fig. 46, we plot the data shown in Tables XIX and XX. We also summarize the results of 5-fold

Algo.	Condition	Training	Test
QCL	CNOT-based, w/o bias	0.6606	0.5810
QCL	CNOT-based, w/ bias	0.6671	0.5739
QCL	CRot-based, w/o bias	0.6299	0.5703
QCL	CRot-based, w/ bias	0.7102	0.6468
QCL	1d Heisenberg, w/o bias	0.7320	0.6761
QCL	1d Heisenberg, w/ bias	0.7455	0.6924
QCL	FC Heisenberg, w/o bias	0.6653	0.6236
QCL	FC Heisenberg, w/ bias	0.6715	0.6285

TABLE XIX: Results of 5-fold CV with 5 different random seeds of QCL for the sonar dataset (0 or 1). The number of layers L is set to 5 and the number of iterations is set to 300.

CV with 5 different random seeds of the kernel method in Table XXI. More specifically, we use Ridge classification in Sec. G2. We consider the linear functions and the second-order polynomial functions for $\phi(\cdot)$ in Eq. (G8) with and

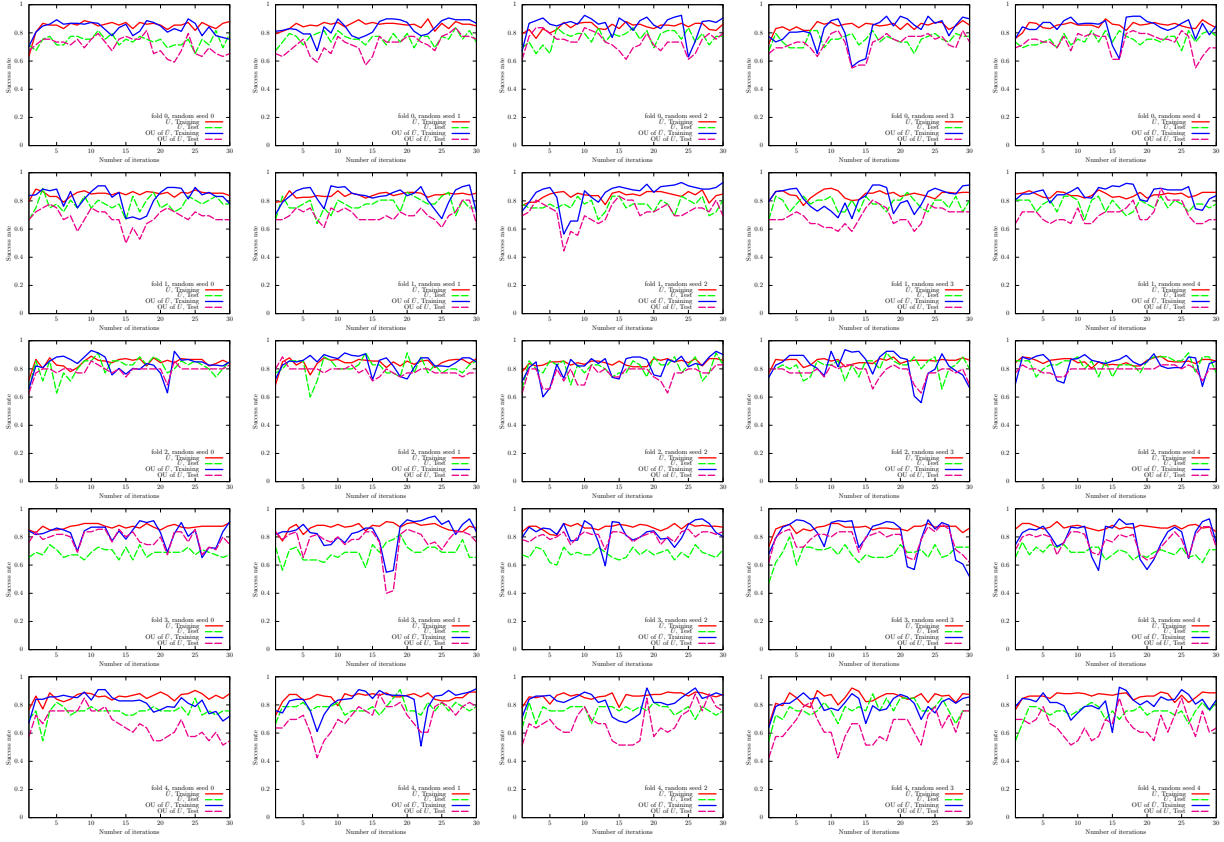


FIG. 44: Results of the UKM (\hat{X} and \hat{P}) on the 5-fold datasets with 5 different random seeds for the sonar dataset (0 or 1). We use complex matrices and set $\theta_{\text{bias}} = 0$. We set $r = 0.010$.

Algo.	Condition	Training	Test
UKM	\hat{X} , complex, w/o bias	0.8903	0.7774
UKM	\hat{P} , complex, w/o bias	0.9159	0.7985
UKM	OU of \hat{X} , complex, w/o bias	0.9175	0.7909
UKM	\hat{X} , complex, w/ bias	0.9027	0.7723
UKM	\hat{P} , complex, w/ bias	0.6621	0.6036
UKM	OU of \hat{X} , complex, w/ bias	0.6351	0.5795
UKM	\hat{X} , real, w/o bias	0.8899	0.7630
UKM	\hat{P} , real, w/o bias	0.9141	0.7842
UKM	OU of \hat{X} , real, w/o bias	0.9108	0.7818
UKM	\hat{X} , real, w/ bias	0.9014	0.7772
UKM	\hat{P} , real, w/ bias	0.6913	0.6391
UKM	OU of \hat{X} , real, w/ bias	0.6769	0.6288

TABLE XX: Results of 5-fold CV with 5 different random seeds of the UKM for the sonar dataset (0 or 1). We put $r = 0.010$ and set $K = 30$ and $K' = 10$.

without normalization. We set $\lambda = 10^{-2}, 10^{-1}, 1$ where λ is the coefficient of the regularization term.

Next, we show the performance dependence of the three algorithms on their key parameters. We see the performance dependence of QCL on the number of layers L . The result is shown in Fig. 47. We then see the performance dependence of the UKM on r , which is the coefficient of the second term in the right-hand side of Eq. (J8). The result is shown in Fig. 48. In Fig. 49, we show the performance dependence of the kernel method on λ , which is the coefficient of the second term in the right-hand side of Eq. (G11).

So far, we have used the squared error function, Eq. (F22). In Fig. 50, we show the performance dependence of QCL on the number of layers L in the case of the hinge function, Eq. (F23). In Fig. 51, we show the performance

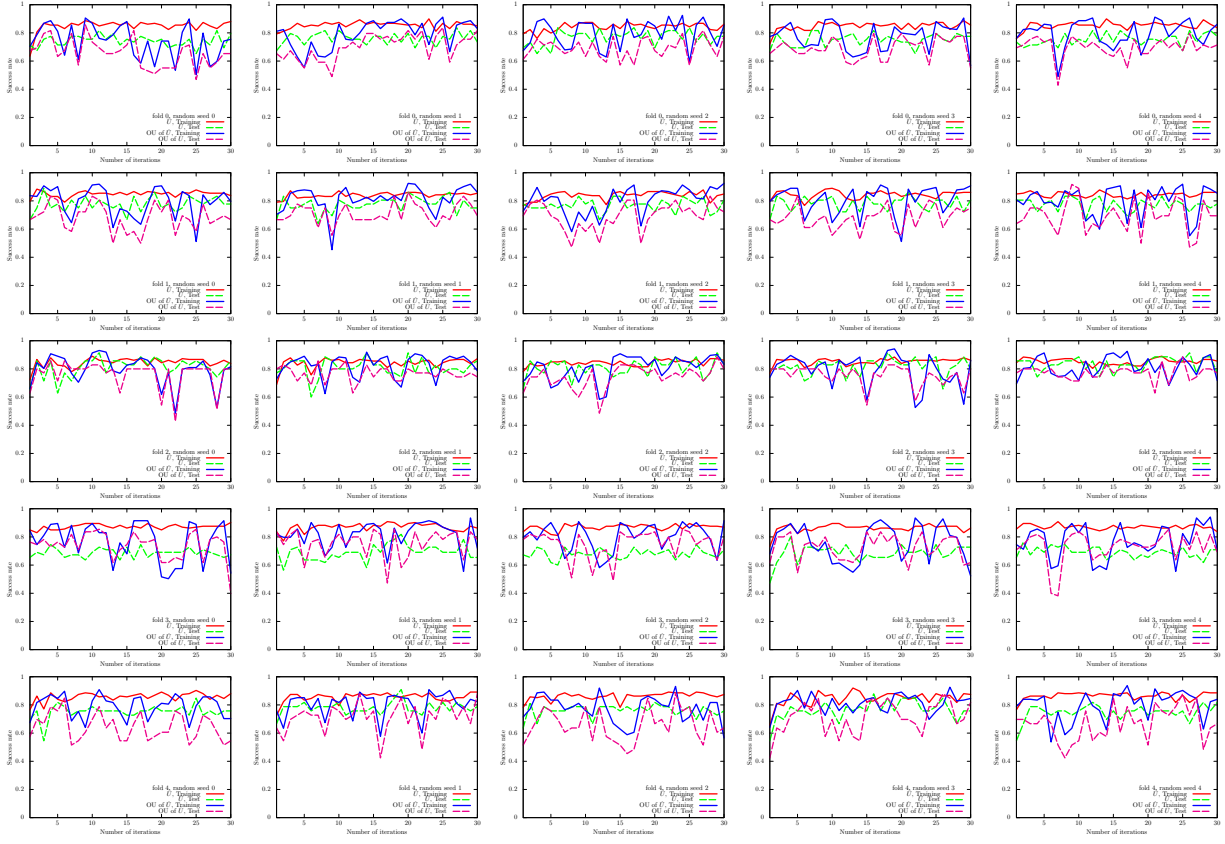


FIG. 45: Results of the UKM (\hat{X} and OU of \hat{X}) on the 5-fold datasets with 5 different random seeds for the sonar dataset (0 or 1). We use complex matrices and set $\theta_{\text{bias}} = 0$. We set $r = 0.010$.

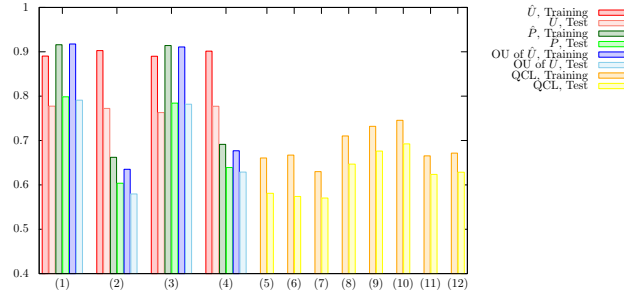


FIG. 46: Results of 5-fold CV with 5 different random seeds for the sonar dataset (0 or 1). For the UKM, we put $r = 0.010$ and set $K = 30$ and $K' = 10$. For QCL, the number of layers L is 5 and the number of iterations is 300. The numerical settings are as follows: (1) complex matrices without the bias term, (2) complex matrices with the bias term, (3) real matrices without the bias term, (4) real matrices with the bias term, (5) CNOT-based circuit without the bias term, (6) CNOT-based circuit with the bias term, (7) CRot-based circuit without the bias term, (8) CRot-based circuit with the bias term, (9) 1d Heisenberg circuit without the bias term, (10) 1d Heisenberg circuit with the bias term, (11) FC Heisenberg circuit without the bias term, and (12) FC Heisenberg circuit with the bias term.

dependence of the UKM on r , which is the coefficient of the second term in the right-hand side of Eq. (J8), in the case of the hinge function, Eq. (F23).

Algo.	Condition	Training	Test
Kernel method	Linear, w/o normalization, $\lambda = 10^{-2}$	0.9109	0.7574
Kernel method	Linear, w/o normalization, $\lambda = 10^{-1}$	0.8738	0.7717
Kernel method	Linear, w/o normalization, $\lambda = 1$	0.8667	0.7631
Kernel method	Linear, w/ normalization, $\lambda = 10^{-2}$	0.8806	0.7694
Kernel method	Linear, w/ normalization, $\lambda = 10^{-1}$	0.8522	0.7500
Kernel method	Linear, w/ normalization, $\lambda = 1$	0.8093	0.7076
Kernel method	Poly-2, w/o normalization, $\lambda = 10^{-2}$	1.0000	0.8198
Kernel method	Poly-2, w/o normalization, $\lambda = 10^{-1}$	1.0000	0.8084
Kernel method	Poly-2, w/o normalization, $\lambda = 1$	0.9865	0.8035
Kernel method	Poly-2, w/ normalization, $\lambda = 10^{-2}$	0.9901	0.7973
Kernel method	Poly-2, w/ normalization, $\lambda = 10^{-1}$	0.9297	0.8009
Kernel method	Poly-2, w/ normalization, $\lambda = 1$	0.8348	0.7374

TABLE XXI: Results of 5-fold CV with 5 different random seeds of the kernel method for the sonar dataset (0 or 1).

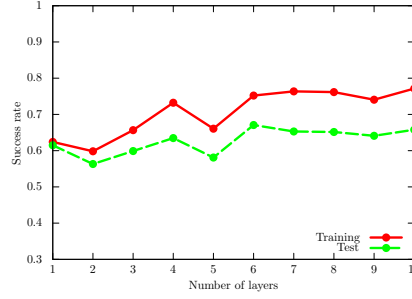


FIG. 47: Performance dependence of QCL on the number of layers L for the sonar dataset (0 or 1). We use the CNOT-based circuit geometry and set $\theta_{\text{bias}} = 0$. We iterate the computation 300 times.

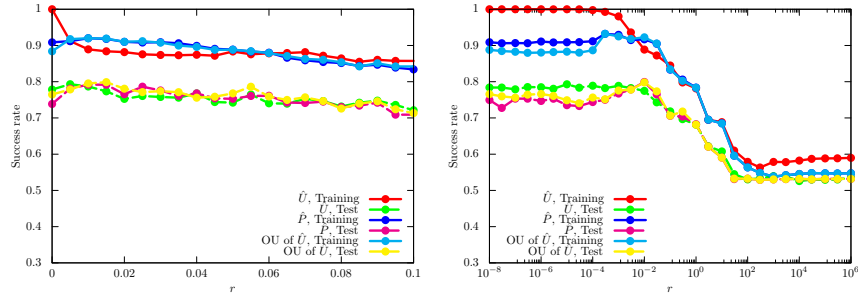


FIG. 48: Performance dependence of the UKM on r , which is the coefficient of the second term in the right-hand side of Eq. (J8) for the sonar dataset (0 or 1). We use complex matrices and set $\theta_{\text{bias}} = 0$. We set $K = 30$ and $K' = 10$.

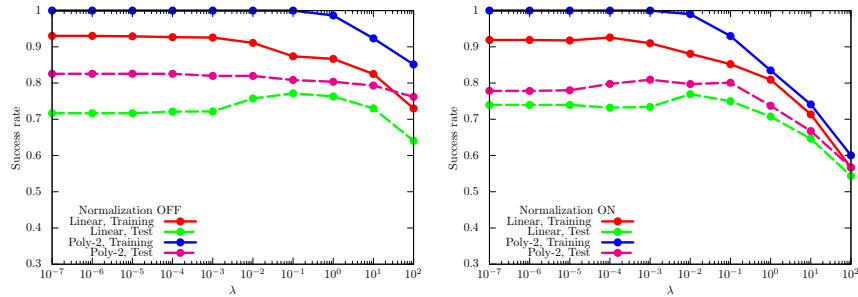


FIG. 49: Performance dependence of the kernel method on λ , which is the coefficient of the second term in the right-hand side of Eq. (G11) for the sonar dataset (0 or 1). For $\phi(\cdot)$ in Eq. (G8), we use the linear functions and the second-degree polynomial functions with and without normalization.

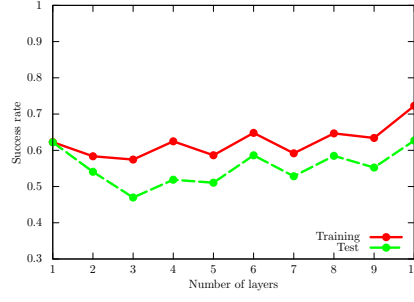


FIG. 50: Performance dependence of QCL on the number of layers L for the sonar dataset (0 or 1) in the case of the hinge function, Eq. (F23). We use the CNOT-based circuit geometry and set $\theta_{\text{bias}} = 0$. We iterate the computation 300 times.

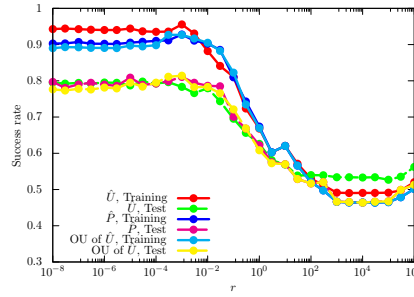


FIG. 51: Performance dependence of the UKM on r , which is the coefficient of the second term in the right-hand side of Eq. (J8) for the sonar dataset (0 or 1) in the case of the hinge function, Eq. (F23). We use complex matrices and set $\theta_{\text{bias}} = 0$. We set $K = 30$ and $K' = 10$.

8. Wine dataset (0 or non-0)

We here show the numerical result for the wine dataset (0 or non-0). For the UKM, we put $r = 0.010$ and set $K = 30$ and $K' = 10$ in Algo. 11. For QCL, we run iterations 300 times.

In Fig. 52, we show the numerical results of QCL for the 5-fold datasets with 5 different random seeds. In Fig. 53,

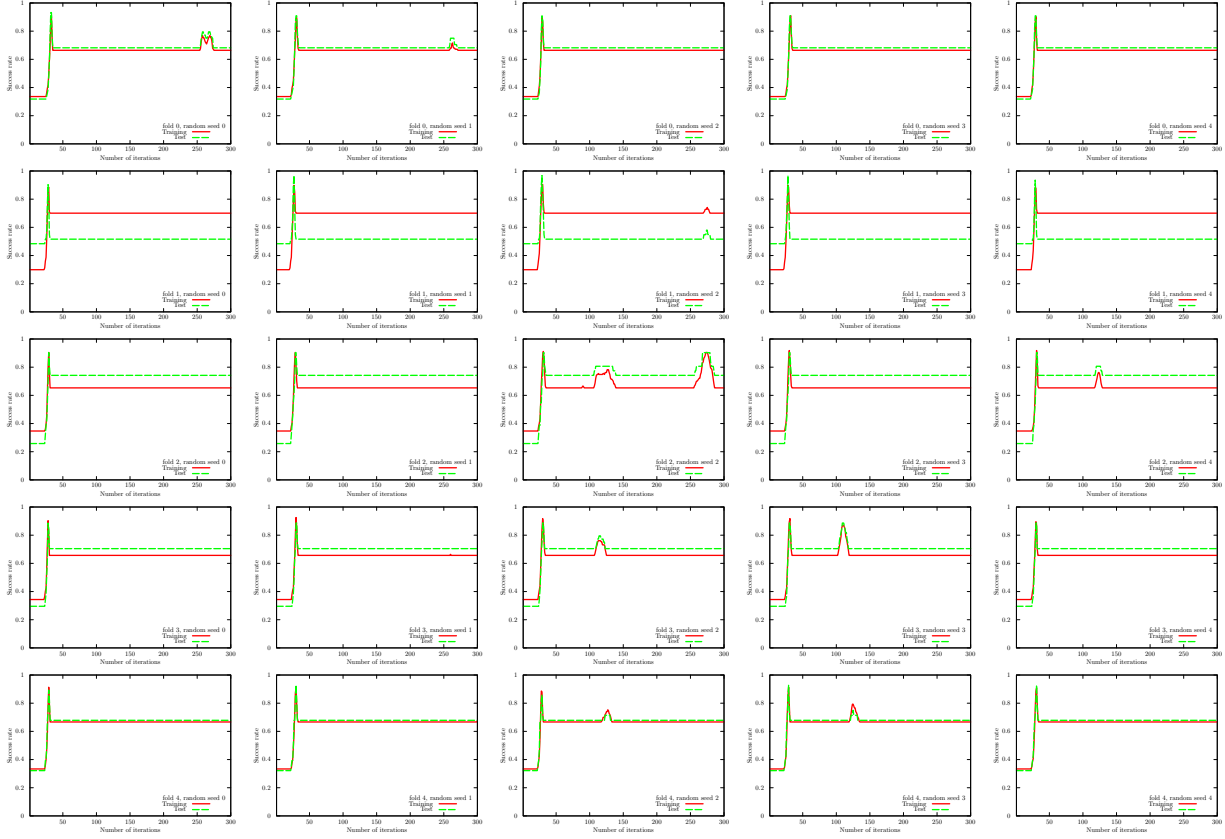


FIG. 52: Results of QCL on the 5-fold datasets with 5 different random seeds for the wine dataset (0 or non-0). We use the CNOT-based circuit and set $\theta_{\text{bias}} = 0$. The number of layers L is set to 5.

we show the numerical results of \hat{P} of the UKM for the 5-fold datasets with 5 different random seeds. In Fig. 54, we also show the numerical results of OU of \hat{X} of the UKM for the 5-fold datasets with 5 different random seeds.

We summarize the results of 5-fold CV with 5 different random seeds of QCL and the UKM in Tables XXII and XXIII, respectively. For QCL and the UKM, we select the best model for the training dataset over iterations to compute the performance. In Fig. 55, we plot the data shown in Tables XXII and XXIII. We also summarize the

Algo.	Condition	Training	Test
QCL	CNOT-based, w/o bias	0.9057	0.9052
QCL	CNOT-based, w/ bias	0.8665	0.8680
QCL	CRot-based, w/o bias	0.9151	0.9086
QCL	CRot-based, w/ bias	0.9145	0.9059
QCL	1d Heisenberg, w/o bias	0.9155	0.9126
QCL	1d Heisenberg, w/ bias	0.8547	0.8440
QCL	FC Heisenberg, w/o bias	0.9103	0.9052
QCL	FC Heisenberg, w/ bias	0.8390	0.8318

TABLE XXII: Results of 5-fold CV with 5 different random seeds of QCL for the wine dataset (0 or non-0). The number of layers L is set to 5 and the number of iterations is set to 300.

results of 5-fold CV with 5 different random seeds of the kernel method in Table XXIV. More specifically, we use Ridge classification in Sec. G 2. We consider the linear functions and the second-order polynomial functions for $\phi(\cdot)$

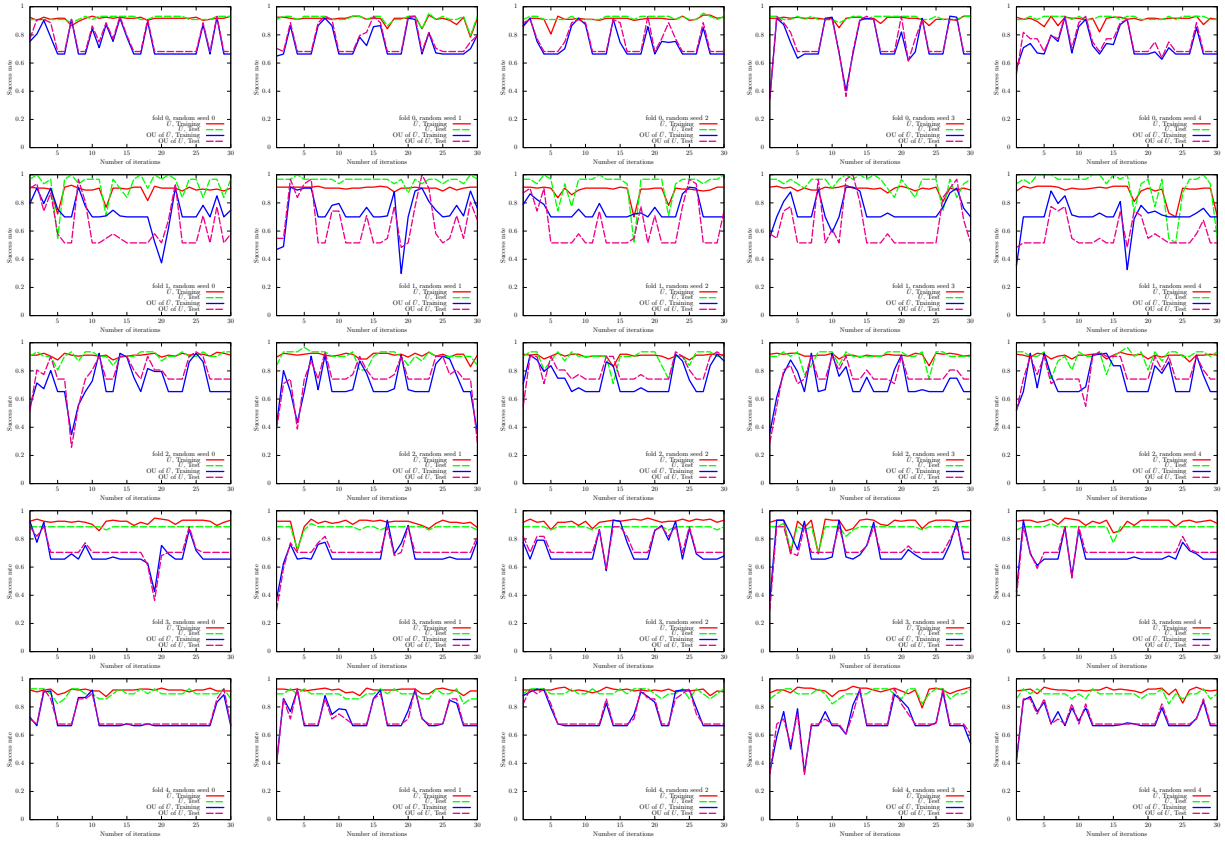


FIG. 53: Results of the UKM (\hat{X} and \hat{P}) on the 5-fold datasets with 5 different random seeds for the wine dataset (0 or non-0). We use complex matrices and set $\theta_{\text{bias}} = 0$. We set $r = 0.010$.

Algo.	Condition	Training	Test
UKM	\hat{X} , complex, w/o bias	0.9328	0.9243
UKM	\hat{P} , complex, w/o bias	0.9213	0.9116
UKM	OU of \hat{X} , complex, w/o bias	0.9215	0.9159
UKM	\hat{X} , complex, w/ bias	0.9364	0.9313
UKM	\hat{P} , complex, w/ bias	0.6420	0.6184
UKM	OU of \hat{X} , complex, w/ bias	0.6282	0.6128
UKM	\hat{X} , real, w/o bias	0.9359	0.9292
UKM	\hat{P} , real, w/o bias	0.9200	0.9185
UKM	OU of \hat{X} , real, w/o bias	0.9212	0.9171
UKM	\hat{X} , real, w/ bias	0.9345	0.9212
UKM	\hat{P} , real, w/ bias	0.6062	0.6055
UKM	OU of \hat{X} , real, w/ bias	0.5716	0.5708

TABLE XXIII: Results of 5-fold CV with 5 different random seeds of the UKM for the wine dataset (0 or non-0). We put $r = 0.010$ and set $K = 30$ and $K' = 10$.

in Eq. (G8) with and without normalization. We set $\lambda = 10^{-2}, 10^{-1}, 1$ where λ is the coefficient of the regularization term.

Next, we show the performance dependence of the three algorithms on their key parameters. We see the performance dependence of QCL on the number of layers L . The result is shown in Fig. 56. We then see the performance dependence of the UKM on r , which is the coefficient of the second term in the right-hand side of Eq. (J8). The result is shown in Fig. 57. In Fig. 58, we show the performance dependence of the kernel method on λ , which is the coefficient of the second term in the right-hand side of Eq. (G11).

So far, we have used the squared error function, Eq. (F22). In Fig. 59, we show the performance dependence of

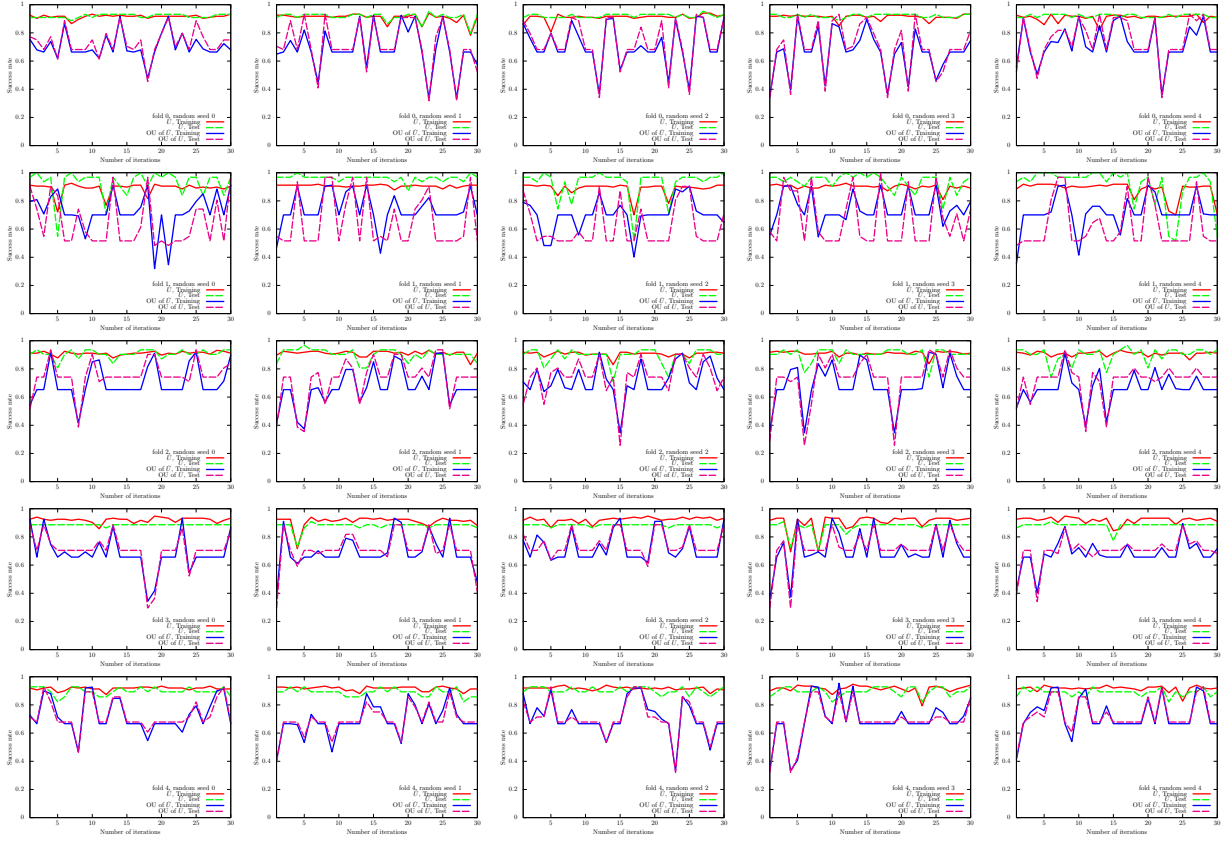


FIG. 54: Results of the UKM (\hat{X} and OU of \hat{X}) on the 5-fold datasets with 5 different random seeds for the wine dataset (0 or non-0). We use complex matrices and set $\theta_{\text{bias}} = 0$. We set $r = 0.010$.

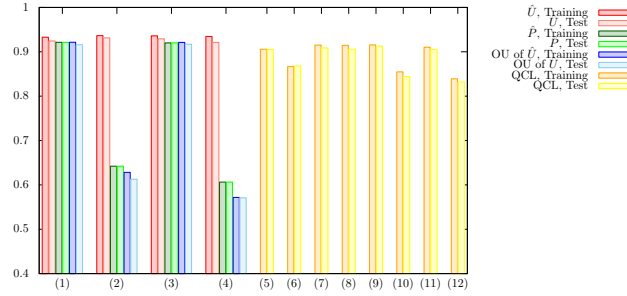


FIG. 55: Results of 5-fold CV with 5 different random seeds for the wine dataset (0 or non-0). For the UKM, we put $r = 0.010$ and set $K = 30$ and $K' = 10$. For QCL, the number of layers L is 5 and the number of iterations is 300. The numerical settings are as follows: (1) complex matrices without the bias term, (2) complex matrices with the bias term, (3) real matrices without the bias term, (4) real matrices with the bias term, (5) CNOT-based circuit without the bias term, (6) CNOT-based circuit with the bias term, (7) CRot-based circuit without the bias term, (8) CRot-based circuit with the bias term, (9) 1d Heisenberg circuit without the bias term, (10) 1d Heisenberg circuit with the bias term, (11) FC Heisenberg circuit without the bias term, and (12) FC Heisenberg circuit with the bias term.

QCL on the number of layers L in the case of the hinge function, Eq. (F23). In Fig. 60, we show the performance dependence of the UKM on r , which is the coefficient of the second term in the right-hand side of Eq. (J8), in the case of the hinge function, Eq. (F23).

Algo.	Condition	Training	Test
Kernel method	Linear, w/o normalization, $\lambda = 10^{-2}$	0.9987	0.9955
Kernel method	Linear, w/o normalization, $\lambda = 10^{-1}$	0.9987	0.9883
Kernel method	Linear, w/o normalization, $\lambda = 1$	0.9987	0.9883
Kernel method	Linear, w/ normalization, $\lambda = 10^{-2}$	0.9357	0.9474
Kernel method	Linear, w/ normalization, $\lambda = 10^{-1}$	0.9230	0.9183
Kernel method	Linear, w/ normalization, $\lambda = 1$	0.6807	0.6711
Kernel method	Poly-2, w/o normalization, $\lambda = 10^{-2}$	1.0000	0.9481
Kernel method	Poly-2, w/o normalization, $\lambda = 10^{-1}$	1.0000	0.9558
Kernel method	Poly-2, w/o normalization, $\lambda = 1$	1.0000	0.9683
Kernel method	Poly-2, w/ normalization, $\lambda = 10^{-2}$	0.9455	0.9520
Kernel method	Poly-2, w/ normalization, $\lambda = 10^{-1}$	0.9259	0.9293
Kernel method	Poly-2, w/ normalization, $\lambda = 1$	0.8413	0.8258

TABLE XXIV: Results of 5-fold CV with 5 different random seeds of the kernel method for the wine dataset (0 or non-0).

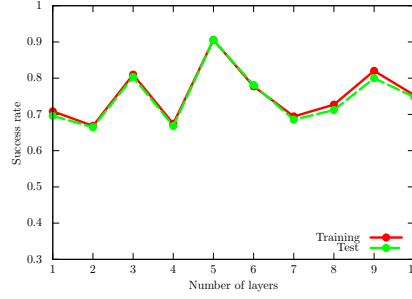


FIG. 56: Performance dependence of QCL on the number of layers L for the wine dataset (0 or non-0). We use the CNOT-based circuit geometry and set $\theta_{\text{bias}} = 0$. We iterate the computation 300 times.

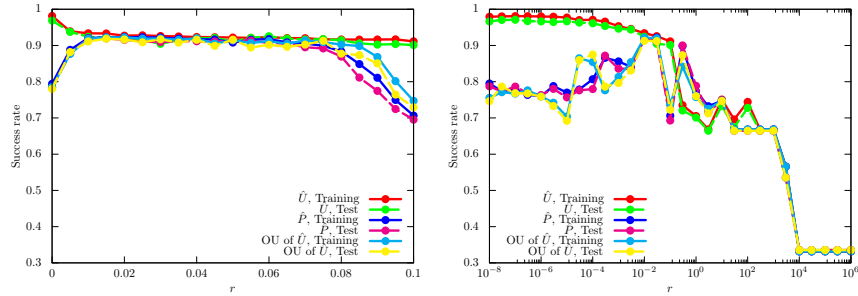


FIG. 57: Performance dependence of the UKM on r , which is the coefficient of the second term in the right-hand side of Eq. (J8) for the wine dataset (0 or non-0). We use complex matrices and set $\theta_{\text{bias}} = 0$. We set $K = 30$ and $K' = 10$.

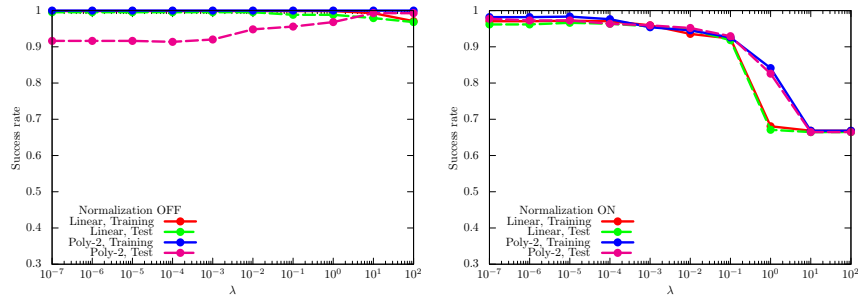


FIG. 58: Performance dependence of the kernel method on λ , which is the coefficient of the second term in the right-hand side of Eq. (G11) for the wine dataset (0 or non-0). For $\phi(\cdot)$ in Eq. (G8), we use the linear functions and the second-degree polynomial functions with and without normalization.

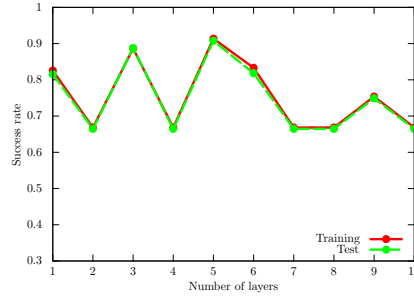


FIG. 59: Performance dependence of QCL on the number of layers L for the wine dataset (0 or non-0) in the case of the hinge function, Eq. (F23). We use the CNOT-based circuit geometry and set $\theta_{\text{bias}} = 0$. We iterate the computation 300 times.

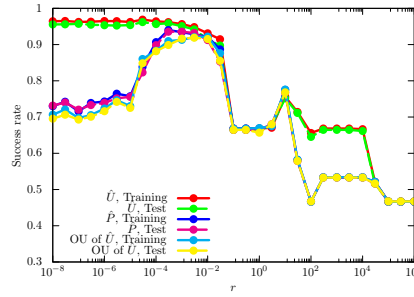


FIG. 60: Performance dependence of the UKM on r , which is the coefficient of the second term in the right-hand side of Eq. (J8) for the wine dataset (0 or non-0) in the case of the hinge function, Eq. (F23). We use complex matrices and set $\theta_{\text{bias}} = 0$. We set $K = 30$ and $K' = 10$.

9. Semeion dataset (0 or 1)

We here show the numerical result for the semeion dataset (0 or 1). For the UKM, we put $r = 0.010$ and set $K = 20$ and $K' = 10$ in Algo. 11. For QCL, we run iterations 100 times.

In Fig. 61, we show the numerical results of QCL for the 5-fold datasets with 5 different random seeds. In Fig. 62,

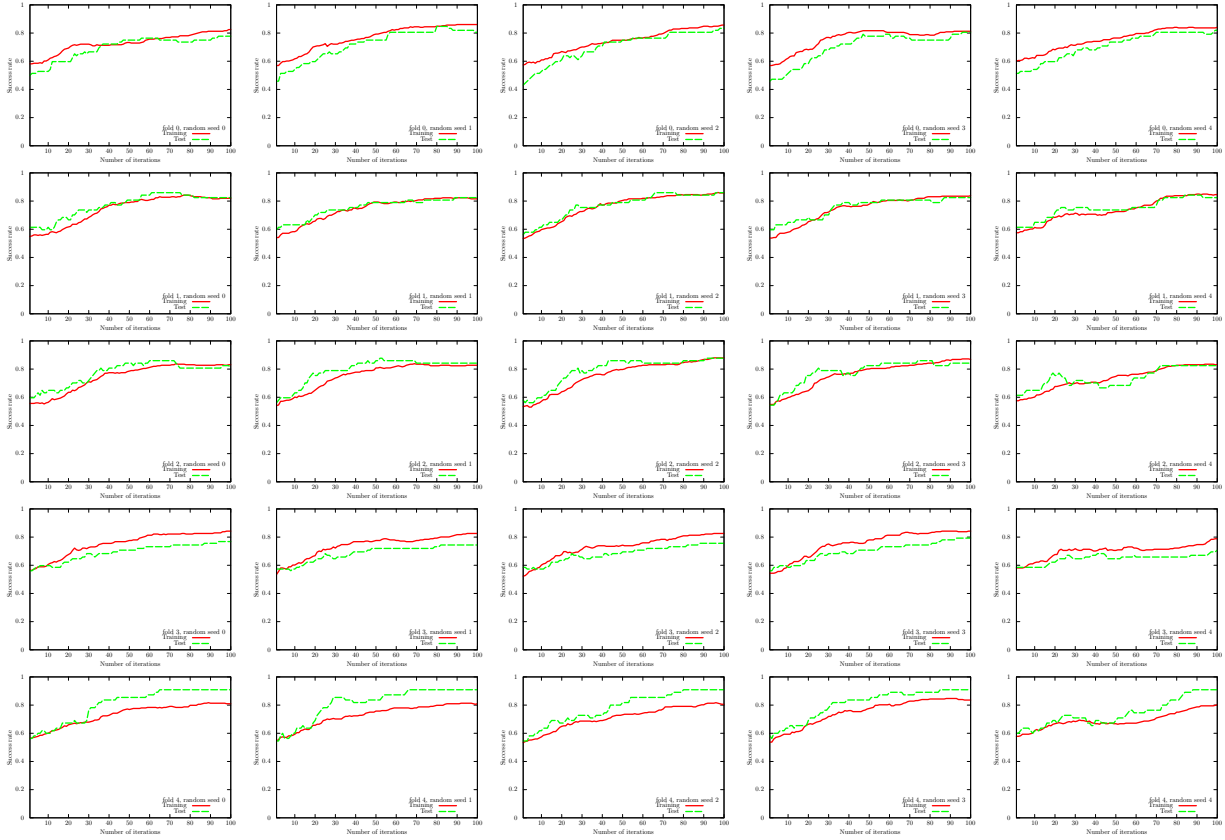


FIG. 61: Results of QCL on the 5-fold datasets with 5 different random seeds for the semeion dataset (0 or 1). We use the CNOT-based circuit and set $\theta_{\text{bias}} = 0$. The number of layers L is set to 5.

we show the numerical results of \hat{P} of the UKM for the 5-fold datasets with 5 different random seeds. In Fig. 63, we also show the numerical results of OU of \hat{X} of the UKM for the 5-fold datasets with 5 different random seeds.

We summarize the results of 5-fold CV with 5 different random seeds of QCL and the UKM in Tables XXV and XXVI, respectively. For QCL and the UKM, we select the best model for the training dataset over iterations to compute the performance. In Fig. 64, we plot the data shown in Tables XXV and XXVI. We also summarize the

Algo.	Condition	Training	Test
QCL	CNOT-based, w/o bias	0.8356	0.8288
QCL	CNOT-based, w/ bias	0.9210	0.9099
QCL	CRot-based, w/o bias	0.4867	0.4566
QCL	CRot-based, w/ bias	0.7222	0.7162

TABLE XXV: Results of 5-fold CV with 5 different random seeds of QCL for the semeion dataset (0 or 1). The number of layers L is 5 and the number of iterations is 100.

results of 5-fold CV with 5 different random seeds of the kernel method in Table XXVII. More specifically, we use Ridge classification in Sec. G 2. We consider the linear functions and the second-order polynomial functions for $\phi(\cdot)$ in Eq. (G8) with and without normalization. We set $\lambda = 10^{-2}, 10^{-1}, 1$ where λ is the coefficient of the regularization term.

Next, we show the performance dependence of the three algorithms on their key parameters. We see the performance dependence of QCL on the number of layers L . The result is shown in Fig. 65. We then see the performance dependence

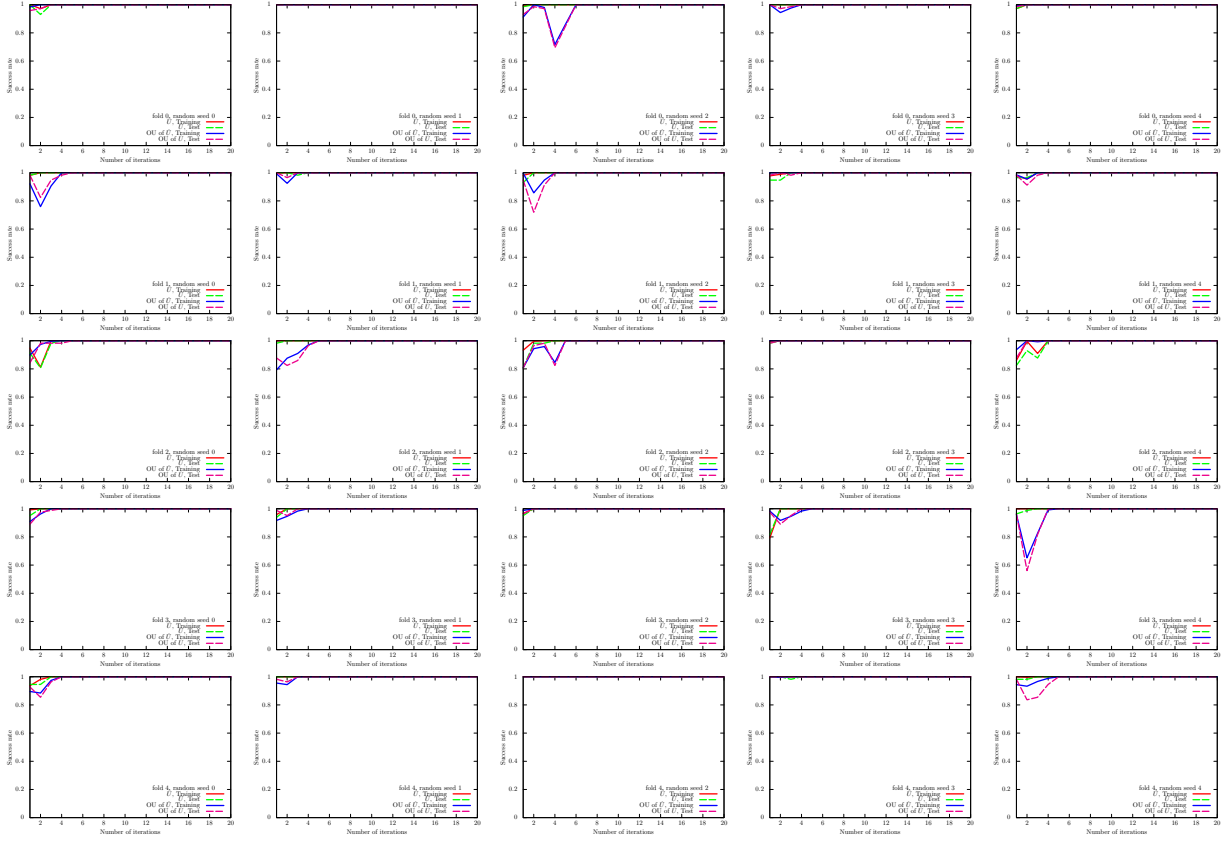


FIG. 62: Results of the UKM (\hat{X} and \hat{P}) on the 5-fold datasets with 5 different random seeds for the semeion dataset (0 or 1). We use complex matrices and set $\theta_{\text{bias}} = 0$. We set $r = 0.010$.

Algo.	Condition	Training	Test
UKM	\hat{X} , complex, w/o bias	1.0	0.9957
UKM	\hat{P} , complex, w/o bias	1.0	0.9943
UKM	OU of \hat{X} , complex, w/o bias	1.0	0.9941
UKM	\hat{X} , complex, w/ bias	1.0	0.9922
UKM	\hat{P} , complex, w/ bias	1.0	0.9735
UKM	OU of \hat{X} , complex, w/ bias	1.0	0.9755
UKM	\hat{X} , real, w/o bias	1.0	0.9939
UKM	\hat{P} , real, w/o bias	1.0	0.9939
UKM	OU of \hat{X} , real, w/o bias	1.0	0.9945
UKM	\hat{X} , real, w/ bias	1.0	0.9941
UKM	\hat{P} , real, w/ bias	1.0	0.9814
UKM	OU of \hat{X} , real, w/ bias	1.0	0.9865

TABLE XXVI: Results of 5-fold CV with 5 different random seeds of the UKM for the semeion dataset (0 or 1). We put $r = 0.010$ and set $K = 20$ and $K = 10$.

of the UKM on r , which is the coefficient of the second term in the right-hand side of Eq. (J8). The result is shown in Fig. 66. In Fig. 67, we show the performance dependence of the kernel method on λ , which is the coefficient of the second term in the right-hand side of Eq. (G11).

So far, we have used the squared error function, Eq. (F22). In Fig. 68, we show the performance dependence of QCL on the number of layers L in the case of the hinge function, Eq. (F23). In Fig. 69, we show the performance dependence of the UKM on r , which is the coefficient of the second term in the right-hand side of Eq. (J8), in the case of the hinge function, Eq. (F23).

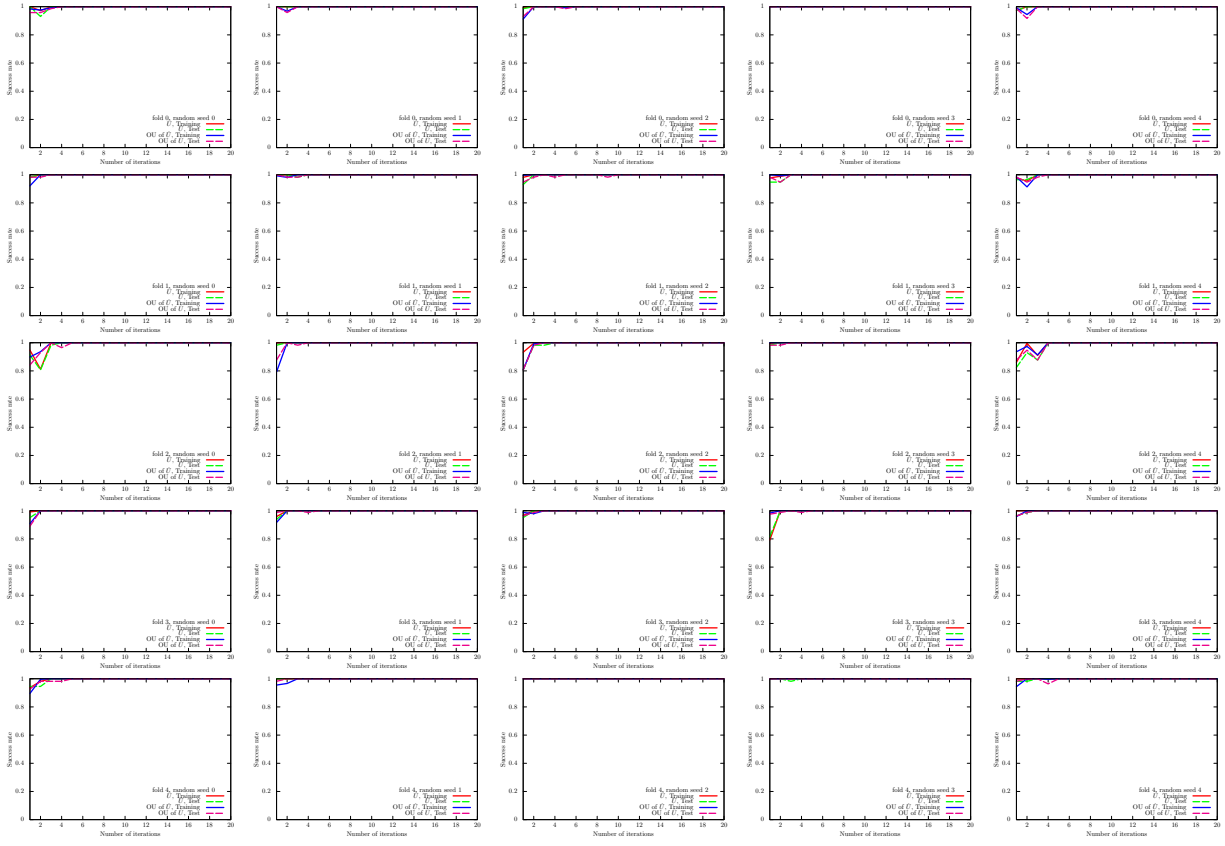


FIG. 63: Results of the UKM (\hat{X} and OU of \hat{X}) on the 5-fold datasets with 5 different random seeds for the semeion dataset (0 or 1). We use complex matrices and set $\theta_{\text{bias}} = 0$. We set $r = 0.010$.

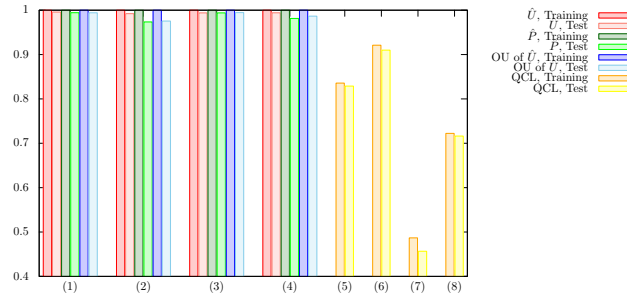


FIG. 64: Results of 5-fold CV with 5 different random seeds for the semeion dataset (0 or 1). For the UKM, we put $r = 0.010$ and set $K = 20$ and $K' = 10$. For QCL, the number of layers L is 5 and the number of iterations is 100. The numerical settings are as follows: (1) complex matrices without the bias term, (2) complex matrices with the bias term, (3) real matrices without the bias term, (4) real matrices with the bias term, (5) CNOT-based circuit without the bias term, (6) CNOT-based circuit with the bias term, (7) CRot-based circuit without the bias term, (8) CRot-based circuit with the bias term, (9) 1d Heisenberg circuit without the bias term, (10) 1d Heisenberg circuit with the bias term, (11) FC Heisenberg circuit without the bias term, and (12) FC Heisenberg circuit with the bias term.

Algo.	Condition	Training	Test
Kernel method	Linear, w/o normalization, $\lambda = 10^{-2}$	1.0000	0.8688
Kernel method	Linear, w/o normalization, $\lambda = 10^{-1}$	1.0000	0.9413
Kernel method	Linear, w/o normalization, $\lambda = 1$	1.0000	0.9822
Kernel method	Linear, w/ normalization, $\lambda = 10^{-2}$	1.0000	0.9858
Kernel method	Linear, w/ normalization, $\lambda = 10^{-1}$	1.0000	0.9965
Kernel method	Linear, w/ normalization, $\lambda = 1$	1.0000	1.0000
Kernel method	Poly-2, w/o normalization, $\lambda = 10^{-2}$	1.0000	0.9895
Kernel method	Poly-2, w/o normalization, $\lambda = 10^{-1}$	1.0000	0.9895
Kernel method	Poly-2, w/o normalization, $\lambda = 1$	1.0000	0.9895
Kernel method	Poly-2, w/ normalization, $\lambda = 10^{-2}$	1.0000	0.9965
Kernel method	Poly-2, w/ normalization, $\lambda = 10^{-1}$	1.0000	0.9965
Kernel method	Poly-2, w/ normalization, $\lambda = 1$	1.0000	1.0000

TABLE XXVII: Results of 5-fold CV with 5 different random seeds of the kernel method for the semeion dataset (0 or 1).

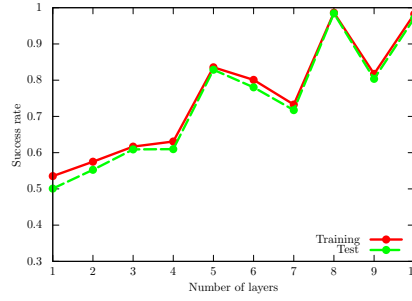


FIG. 65: Performance dependence of QCL on the number of layers L for the semeion dataset (0 or 1). We use the CNOT-based circuit geometry and set $\theta_{\text{bias}} = 0$. We iterate the computation 100 times.

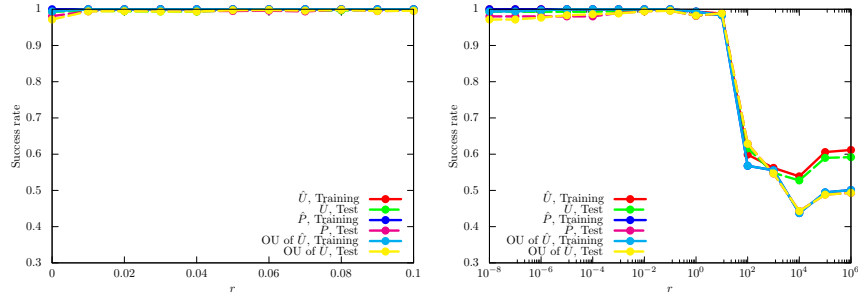


FIG. 66: Performance dependence of the UKM on r , which is the coefficient of the second term in the right-hand side of Eq. (J8) for the semeion dataset (0 or 1). We use complex matrices and set $\theta_{\text{bias}} = 0$. We set $K = 20$ and $K' = 10$.

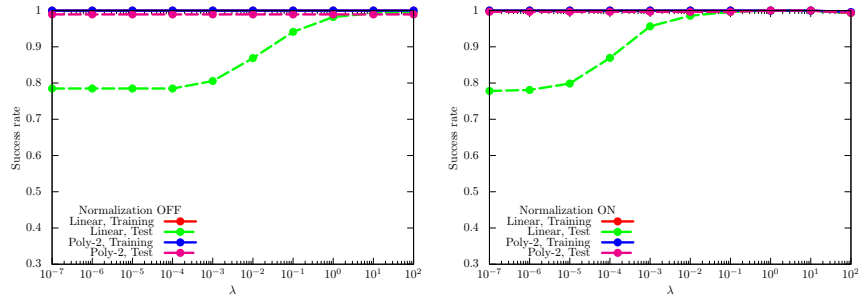


FIG. 67: Performance dependence of the kernel method on λ , which is the coefficient of the second term in the right-hand side of Eq. (G11) for the semeion dataset (0 or 1). For $\phi(\cdot)$ in Eq. (G8), we use the linear functions and the second-degree polynomial functions with and without normalization.

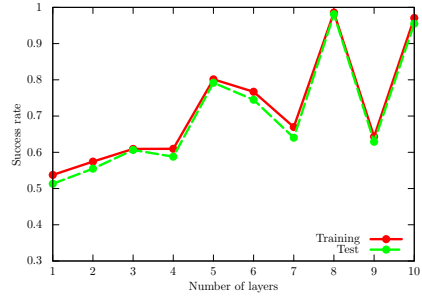


FIG. 68: Performance dependence of QCL on the number of layers L for the semeion dataset (0 or 1) in the case of the hinge function, Eq. (F23). We use the CNOT-based circuit geometry and set $\theta_{\text{bias}} = 0$. We iterate the computation 300 times.

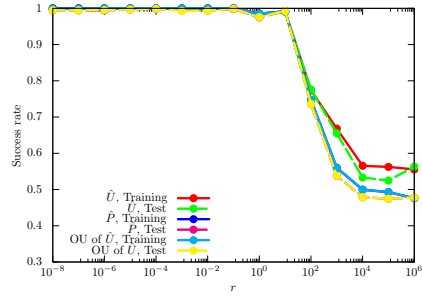


FIG. 69: Performance dependence of the UKM on r , which is the coefficient of the second term in the right-hand side of Eq. (J8) for the semeion dataset (0 or 1) in the case of the hinge function, Eq. (F23). We use complex matrices and set $\theta_{\text{bias}} = 0$. We set $K = 30$ and $K' = 10$.

10. Semeion dataset (0 or non-0)

We here show the numerical result for the semeion dataset (0 or non-0). For the UKM, we put $r = 0.010$ and set $K = 10$ and $K' = 5$ in Algo. 11. For QCL, we run iterations 50 times.

In Fig. 70, we show the numerical results of QCL for the 5-fold datasets with 5 different random seeds. In Fig. 71,

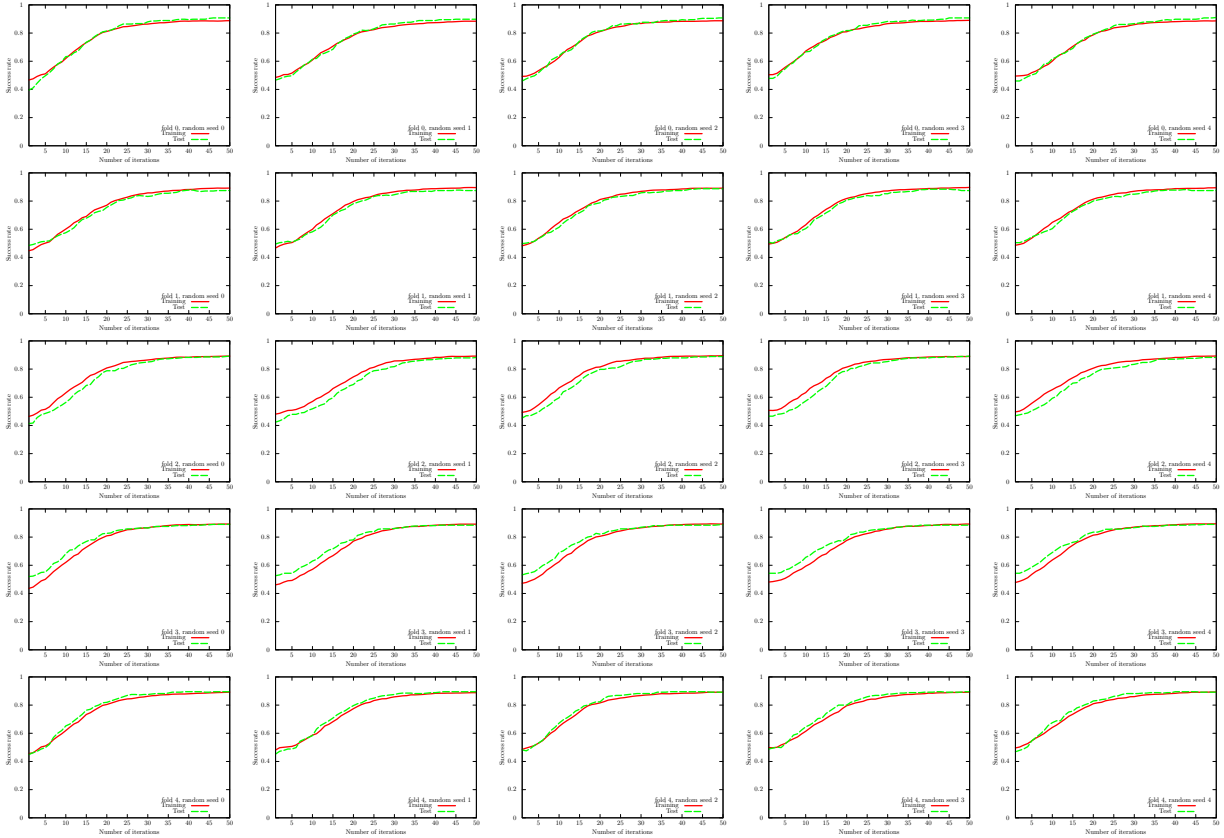


FIG. 70: Results of QCL on the 5-fold datasets with 5 different random seeds for the semeion dataset (0 or non-0). We use the CNOT-based circuit and set $\theta_{\text{bias}} = 0$. The number of layers L is set to 5.

we show the numerical results of \hat{P} of the UKM for the 5-fold datasets with 5 different random seeds. In Fig. 72, we also show the numerical results of OU of \hat{X} of the UKM for the 5-fold datasets with 5 different random seeds.

We summarize the results of 5-fold CV with 5 different random seeds of QCL and the UKM in Tables XXVIII and XXIX, respectively. For QCL and the UKM, we select the best model for the training dataset over iterations to compute the performance. In Fig. 73, we plot the data shown in Tables XXVIII and XXIX. We also summarize

Algo.	Condition	Training	Test
QCL	CNOT-based, w/o bias	0.8913	0.8896
QCL	CNOT-based, w/ bias	0.8989	0.8987
QCL	CRot-based, w/o bias	0.8959	0.8957
QCL	CRot-based, w/ bias	0.8989	0.8982

TABLE XXVIII: Results of 5-fold CV with 5 different random seeds of QCL for the semeion dataset (0 or non-0). The number of layers L is 5 and the number of iterations is 50.

the results of 5-fold CV with 5 different random seeds of the kernel method in Table XXX. More specifically, we use Ridge classification in Sec. G 2. We consider the linear functions and the second-order polynomial functions for $\phi(\cdot)$ in Eq. (G8) with and without normalization. We set $\lambda = 10^{-2}, 10^{-1}, 1$ where λ is the coefficient of the regularization term.

Next, we show the performance dependence of the three algorithms on their key parameters. We see the performance dependence of QCL on the number of layers L . The result is shown in Fig. 74. We then see the performance dependence

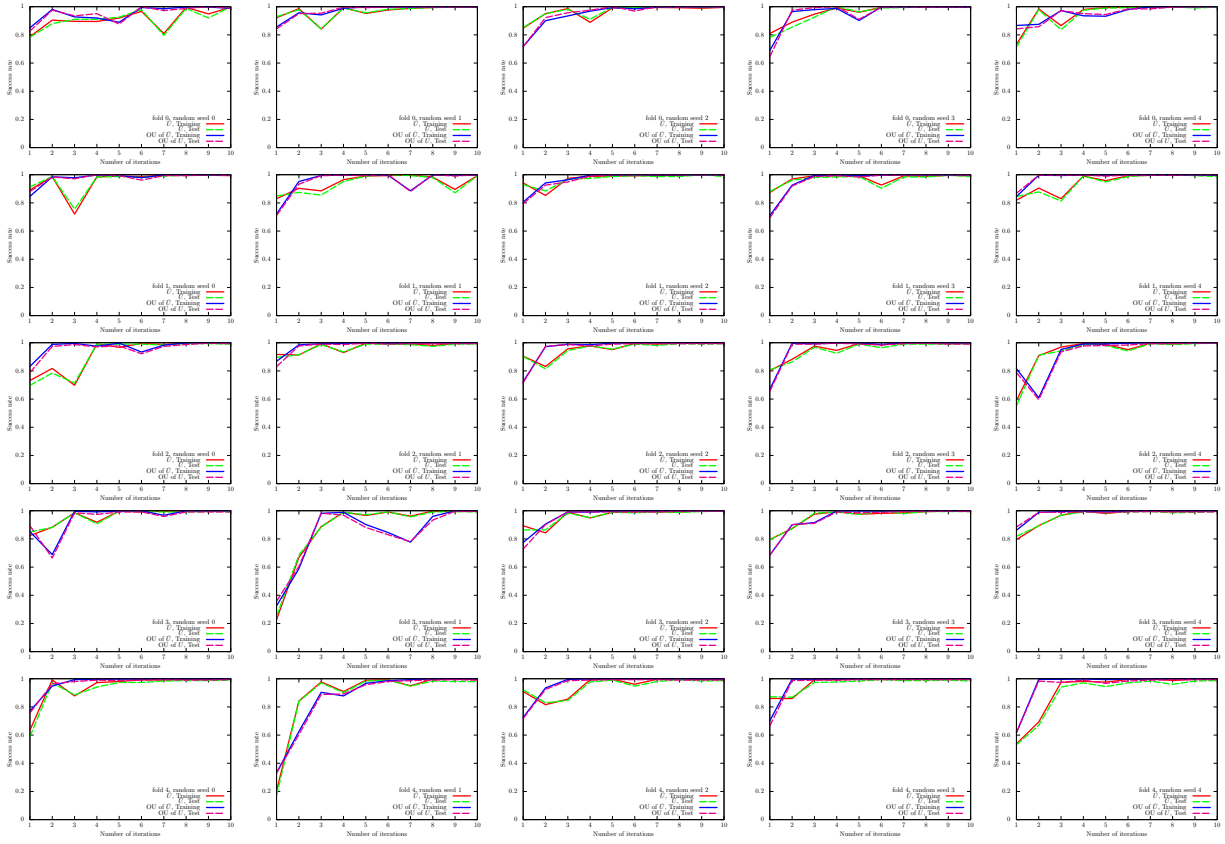


FIG. 71: Results of the UKM (\hat{X} and \hat{P}) on the 5-fold datasets with 5 different random seeds for the semeion dataset (0 or non-0). We use complex matrices and set $\theta_{\text{bias}} = 0$. We set $r = 0.010$.

Algo.	Condition	Training	Test
UKM	\hat{X} , complex, w/o bias	0.9969	0.9925
UKM	\hat{P} , complex, w/o bias	0.9989	0.9945
UKM	OU of \hat{X} , complex, w/o bias	0.9990	0.9953
UKM	\hat{X} , complex, w/ bias	0.9968	0.9921
UKM	\hat{P} , complex, w/ bias	0.9127	0.9094
UKM	OU of \hat{X} , complex, w/ bias	0.9113	0.9071
UKM	\hat{X} , real, w/o bias	0.9961	0.9920
UKM	\hat{P} , real, w/o bias	0.9988	0.9949
UKM	OU of \hat{X} , real, w/o bias	0.9985	0.9938
UKM	\hat{X} , real, w/ bias	0.9969	0.9912
UKM	\hat{P} , real, w/ bias	0.9263	0.9214
UKM	OU of \hat{X} , real, w/ bias	0.9251	0.9213

TABLE XXIX: Results of 5-fold CV with 5 different random seeds of the UKM for the semeion dataset (0 or non-0). We put $r = 0.010$ and set $K = 10$ and $K' = 5$.

of the UKM on r , which is the coefficient of the second term in the right-hand side of Eq. (J8). The result is shown in Fig. 75. In Fig. 76, we show the performance dependence of the kernel method on λ , which is the coefficient of the second term in the right-hand side of Eq. (G11).

So far, we have used the squared error function, Eq. (F22). In Fig. 77, we show the performance dependence of QCL on the number of layers L in the case of the hinge function, Eq. (F23). In Fig. 78, we show the performance dependence of the UKM on r , which is the coefficient of the second term in the right-hand side of Eq. (J8), in the case of the hinge function, Eq. (F23).

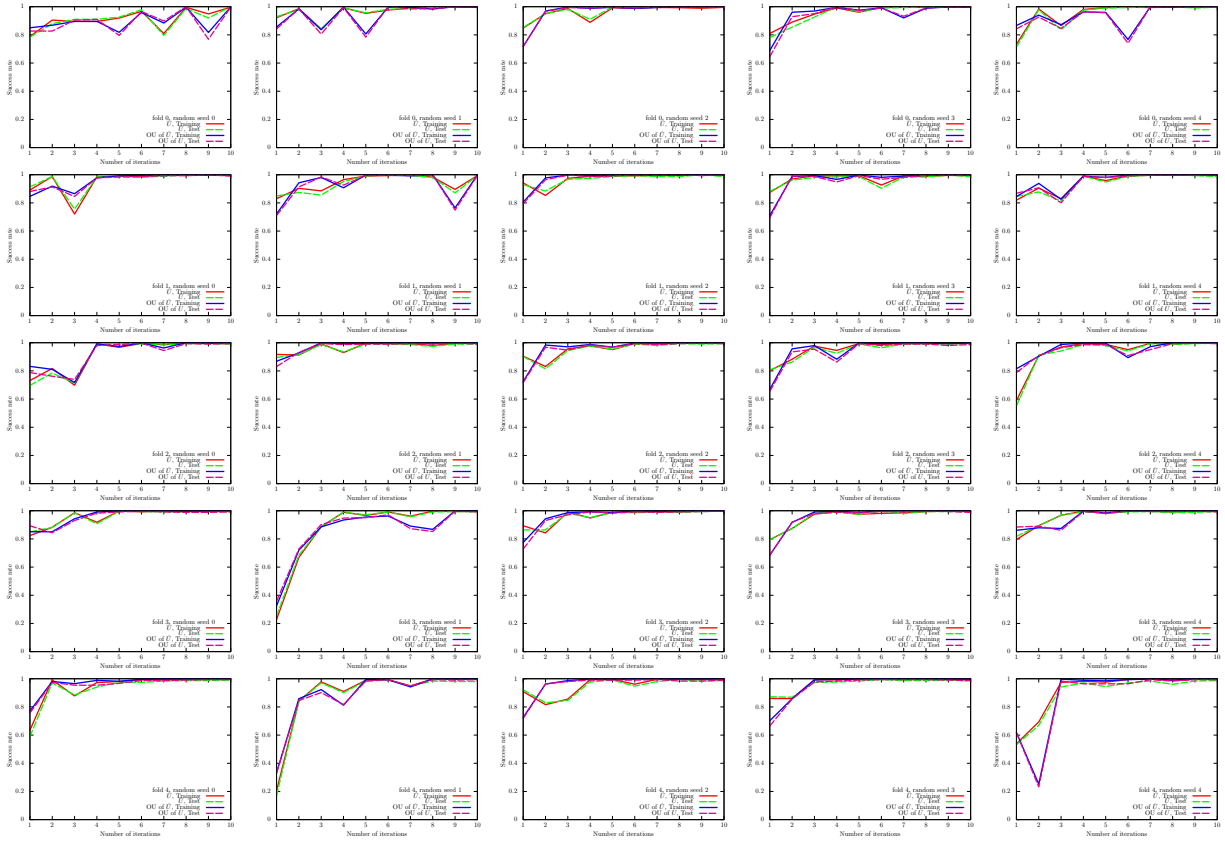


FIG. 72: Results of the UKM (\hat{X} and OU of \hat{X}) on the 5-fold datasets with 5 different random seeds for the semeion dataset (0 or non-0). We use complex matrices and set $\theta_{\text{bias}} = 0$. We set $r = 0.010$.

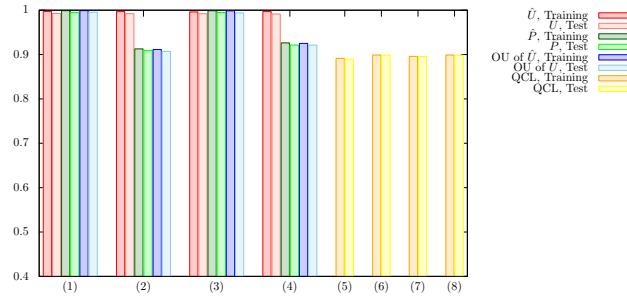


FIG. 73: Results of 5-fold CV with 5 different random seeds for the semeion dataset (0 or non-0). For the UKM, we put $r = 0.010$ and set $K = 10$ and $K' = 5$. For QCL, the number of layers L is 5 and the number of iterations is 50. The numerical settings are as follows: (1) complex matrices without the bias term, (2) complex matrices with the bias term, (3) real matrices without the bias term, (4) real matrices with the bias term, (5) CNOT-based circuit without the bias term, (6) CNOT-based circuit with the bias term, (7) CRot-based circuit without the bias term, (8) CRot-based circuit with the bias term, (9) 1d Heisenberg circuit without the bias term, (10) 1d Heisenberg circuit with the bias term, (11) FC Heisenberg circuit without the bias term, and (12) FC Heisenberg circuit with the bias term.

Algo.	Condition	Training	Test
Kernel method	Linear, w/o normalization, $\lambda = 10^{-2}$	0.9937	0.9887
Kernel method	Linear, w/o normalization, $\lambda = 10^{-1}$	0.9937	0.9887
Kernel method	Linear, w/o normalization, $\lambda = 1$	0.9937	0.9887
Kernel method	Linear, w/ normalization, $\lambda = 10^{-2}$	0.9936	0.9873
Kernel method	Linear, w/ normalization, $\lambda = 10^{-1}$	0.9934	0.9892
Kernel method	Linear, w/ normalization, $\lambda = 1$	0.9931	0.9898
Kernel method	Poly-2, w/o normalization, $\lambda = 10^{-2}$	1.0000	0.9956
Kernel method	Poly-2, w/o normalization, $\lambda = 10^{-1}$	1.0000	0.9956
Kernel method	Poly-2, w/o normalization, $\lambda = 1$	1.0000	0.9956
Kernel method	Poly-2, w/ normalization, $\lambda = 10^{-2}$	1.0000	0.9955
Kernel method	Poly-2, w/ normalization, $\lambda = 10^{-1}$	1.0000	0.9955
Kernel method	Poly-2, w/ normalization, $\lambda = 1$	0.9980	0.9949

TABLE XXX: Results of 5-fold CV with 5 different random seeds of the kernel method for the semeion dataset (0 or non-0).

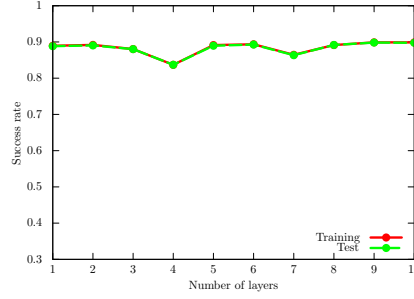


FIG. 74: Performance dependence of QCL on the number of layers L for the semeion dataset (0 or non-0). We use the CNOT-based circuit geometry and set $\theta_{\text{bias}} = 0$. We iterate the computation 50 times.

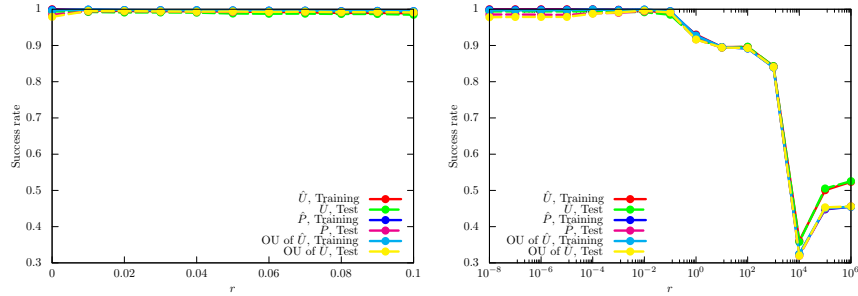


FIG. 75: Performance dependence of the UKM on r , which is the coefficient of the second term in the right-hand side of Eq. (J8) for the semeion dataset (0 or non-0). We use complex matrices and set $\theta_{\text{bias}} = 0$. We set $K = 10$ and $K' = 5$.

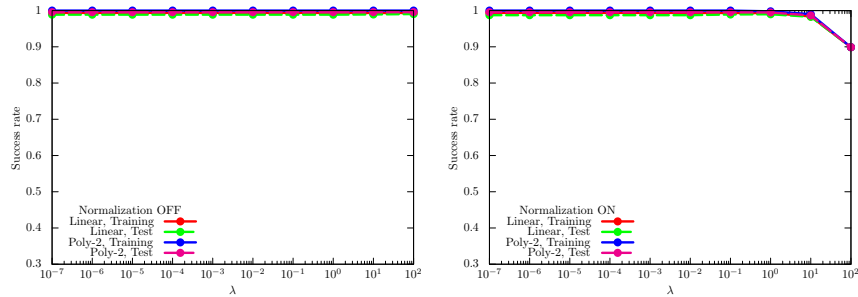


FIG. 76: Performance dependence of the kernel method on λ , which is the coefficient of the second term in the right-hand side of Eq. (G11) for the semeion dataset (0 or non-0). For $\phi(\cdot)$ in Eq. (G8), we use the linear functions and the second-degree polynomial functions with and without normalization.

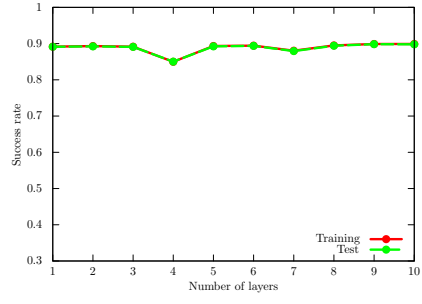


FIG. 77: Performance dependence of QCL on the number of layers L for the semeion dataset (0 or non-0) in the case of the hinge function, Eq. (F23). We use the CNOT-based circuit geometry and set $\theta_{\text{bias}} = 0$. We iterate the computation 300 times.

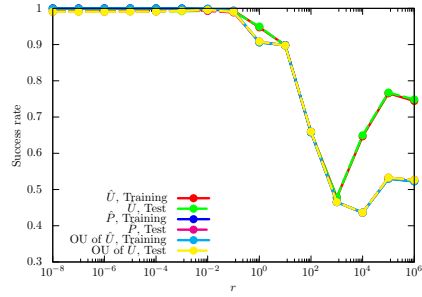


FIG. 78: Performance dependence of the UKM on r , which is the coefficient of the second term in the right-hand side of Eq. (J8) for the semeion dataset (0 or non-0) in the case of the hinge function, Eq. (F23). We use complex matrices and set $\theta_{\text{bias}} = 0$. We set $K = 30$ and $K' = 10$.

11. MNIST256 dataset (0 or 1)

We here show the numerical result for the MNIST256 dataset (0 or 1). For the UKM, we put $r = 0.010$ and set $K = 20$ and $K' = 10$ in Algo. 11. For QCL, we run iterations 100 times.

In Fig. 79, we show the numerical results of QCL for the 5-fold datasets with 5 different random seeds. In Fig. 80,

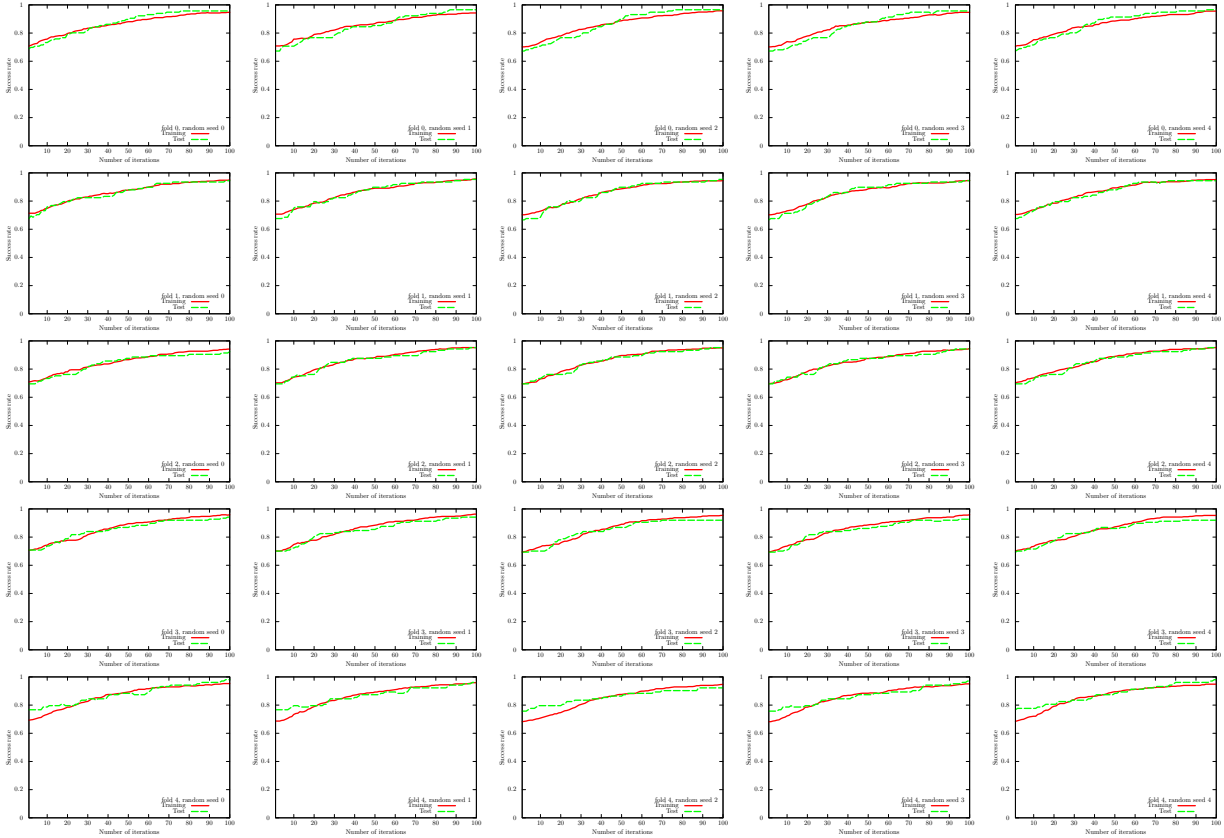


FIG. 79: Results of QCL on the 5-fold datasets with 5 different random seeds for the MNIST256 dataset (0 or 1). We use the CNOT-based circuit and set $\theta_{\text{bias}} = 0$. The number of layers L is set to 5.

we show the numerical results of \hat{P} of the UKM for the 5-fold datasets with 5 different random seeds. In Fig. 81, we also show the numerical results of OU of \hat{X} of the UKM for the 5-fold datasets with 5 different random seeds.

We summarize the results of 5-fold CV with 5 different random seeds of QCL and the UKM in Tables XXXI and XXXII, respectively. For QCL and the UKM, we select the best model for the training dataset over iterations to compute the performance. In Fig. 82, we plot the data shown in Tables XXXI and XXXII. We also summarize the

Algo.	Condition	Training	Test
QCL	CNOT-based, w/o bias	0.9511	0.9459
QCL	CNOT-based, w/ bias	0.9452	0.9413
QCL	CRot-based, w/o bias	0.7372	0.7326
QCL	CRot-based, w/ bias	0.7383	0.7273

TABLE XXXI: Results of 5-fold CV with 5 different random seeds of QCL for the MNIST256 dataset (0 or 1). The number of layers L is 5 and the number of iterations is 100.

results of 5-fold CV with 5 different random seeds of the kernel method in Table XXXIII. More specifically, we use Ridge classification in Sec. G 2. We consider the linear functions and the second-order polynomial functions for $\phi(\cdot)$ in Eq. (G8) with and without normalization. We set $\lambda = 10^{-2}, 10^{-1}, 1$ where λ is the coefficient of the regularization term.

Next, we show the performance dependence of the three algorithms on their key parameters. We see the performance dependence of QCL on the number of layers L . The result is shown in Fig. 83. We then see the performance dependence

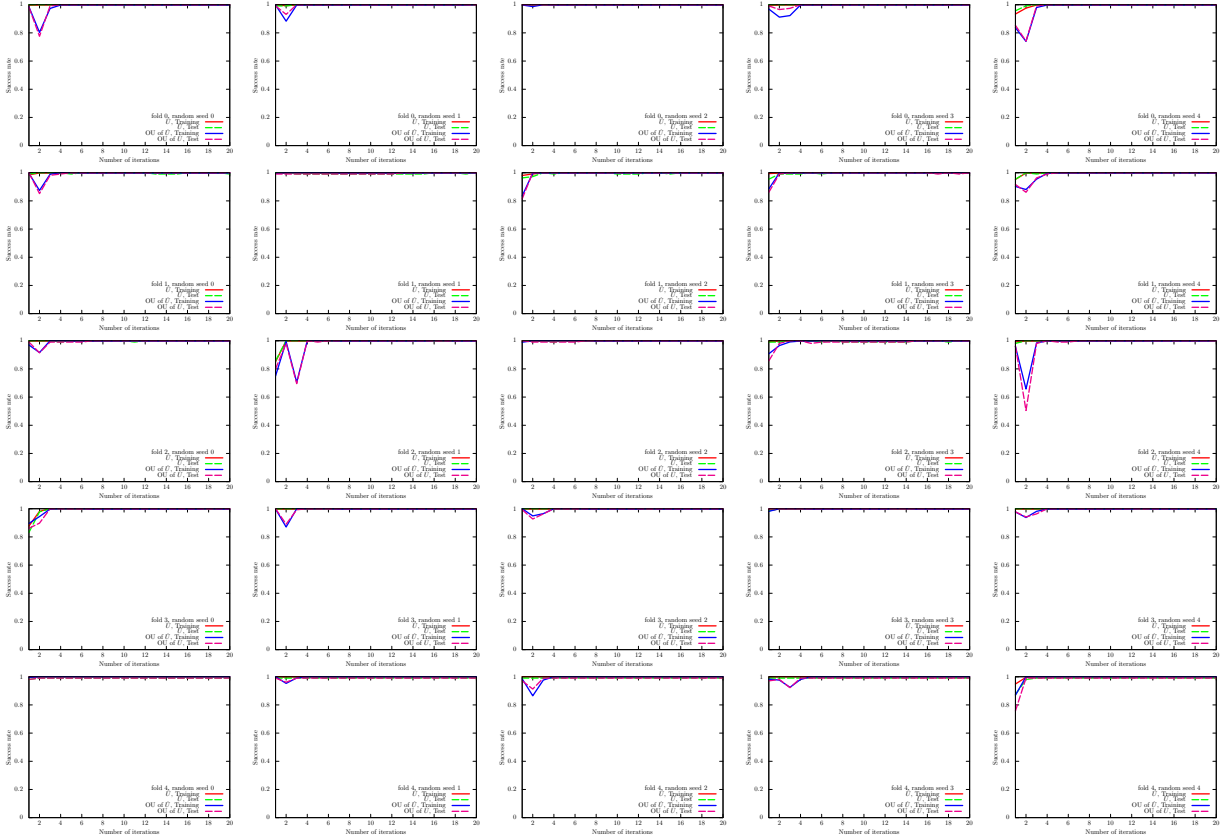


FIG. 80: Results of the UKM (\hat{X} and \hat{P}) on the 5-fold datasets with 5 different random seeds for the MNIST256 dataset (0 or 1). We use complex matrices and set $\theta_{\text{bias}} = 0$. We set $r = 0.010$.

Algo.	Condition	Training	Test
UKM	\hat{X} , complex, w/o bias	0.9985	0.9966
UKM	\hat{P} , complex, w/o bias	0.9992	0.9949
UKM	OU of \hat{X} , complex, w/o bias	1.0	0.9951
UKM	\hat{X} , complex, w/ bias	0.9984	0.9951
UKM	\hat{P} , complex, w/ bias	1.0	0.9945
UKM	OU of \hat{X} , complex, w/ bias	1.0	0.9927
UKM	\hat{X} , real, w/o bias	0.9987	0.9954
UKM	\hat{P} , real, w/o bias	0.9991	0.9969
UKM	OU of \hat{X} , real, w/o bias	0.9997	0.9950
UKM	\hat{X} , real, w/ bias	0.9987	0.9962
UKM	\hat{P} , real, w/ bias	0.9997	0.9944
UKM	OU of \hat{X} , real, w/ bias	0.9997	0.9947

TABLE XXXII: Results of 5-fold CV with 5 different random seeds of the UKM for the MNIST256 dataset (0 or 1). We put $r = 0.010$ and set $K = 20$ and $K' = 10$.

of the UKM on r , which is the coefficient of the second term in the right-hand side of Eq. (J8). The result is shown in Fig. 84. In Fig. 85, we show the performance dependence of the kernel method on λ , which is the coefficient of the second term in the right-hand side of Eq. (G11).

So far, we have used the squared error function, Eq. (F22). In Fig. 86, we show the performance dependence of QCL on the number of layers L in the case of the hinge function, Eq. (F23). In Fig. 87, we show the performance dependence of the UKM on r , which is the coefficient of the second term in the right-hand side of Eq. (J8), in the case of the hinge function, Eq. (F23).

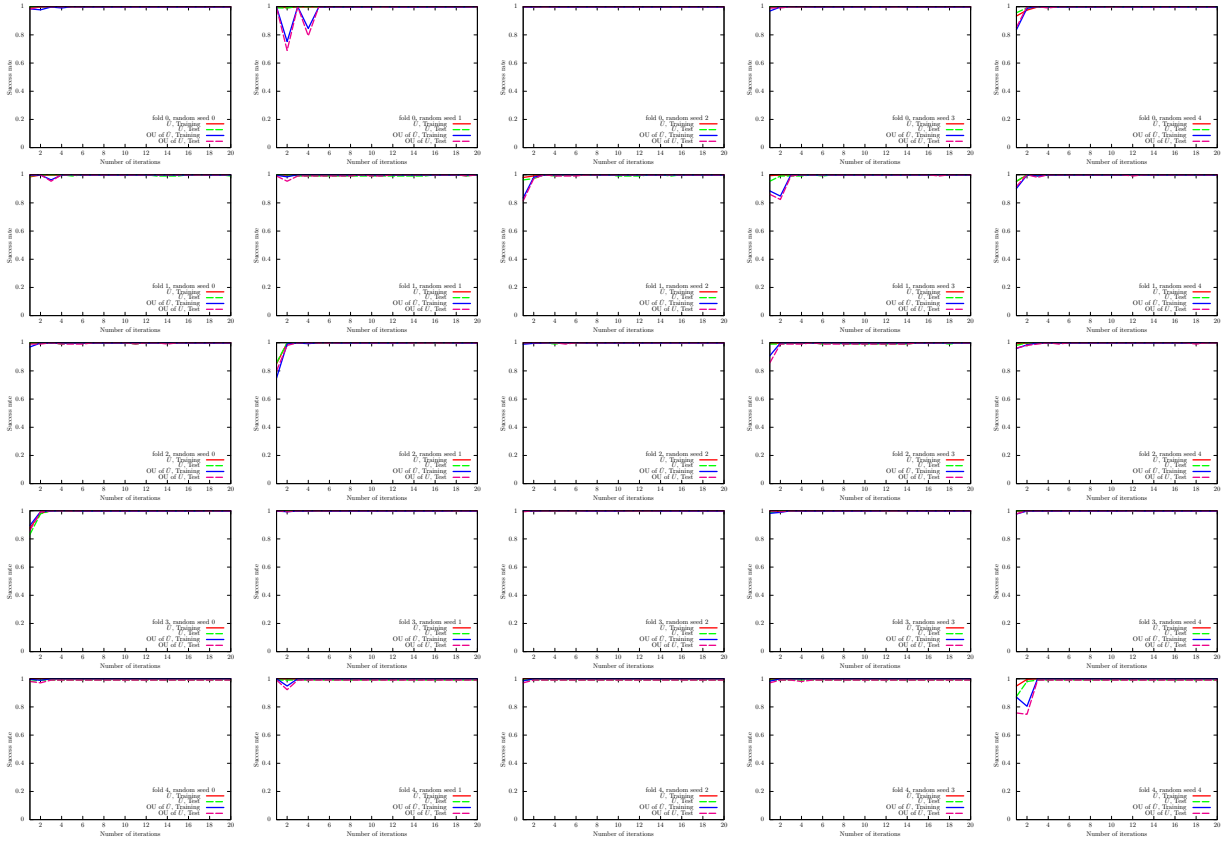


FIG. 81: Results of the UKM (\hat{X} and OU of \hat{X}) on the 5-fold datasets with 5 different random seeds for the MNIST256 dataset (0 or 1). We use complex matrices and set $\theta_{\text{bias}} = 0$. We set $r = 0.010$.

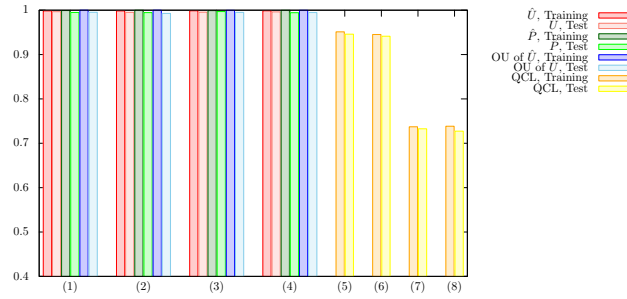


FIG. 82: Results of 5-fold CV with 5 different random seeds for the MNIST256 dataset (0 or 1). For the UKM, we put $r = 0.010$ and set $K = 20$ and $K' = 10$. For QCL, the number of layers L is 5 and the number of iterations is 100. The numerical settings are as follows: (1) complex matrices without the bias term, (2) complex matrices with the bias term, (3) real matrices without the bias term, (4) real matrices with the bias term, (5) CNOT-based circuit without the bias term, (6) CNOT-based circuit with the bias term, (7) CRot-based circuit without the bias term, (8) CRot-based circuit with the bias term, (9) 1d Heisenberg circuit without the bias term, (10) 1d Heisenberg circuit with the bias term, (11) FC Heisenberg circuit without the bias term, and (12) FC Heisenberg circuit with the bias term.

Algo.	Condition	Training	Test
Kernel method	Linear, w/o normalization, $\lambda = 10^{-2}$	1.0000	1.0000
Kernel method	Linear, w/o normalization, $\lambda = 10^{-1}$	1.0000	1.0000
Kernel method	Linear, w/o normalization, $\lambda = 1$	1.0000	1.0000
Kernel method	Linear, w/ normalization, $\lambda = 10^{-2}$	0.9991	0.9981
Kernel method	Linear, w/ normalization, $\lambda = 10^{-1}$	0.9982	0.9981
Kernel method	Linear, w/ normalization, $\lambda = 1$	0.9982	0.9981
Kernel method	Poly-2, w/o normalization, $\lambda = 10^{-2}$	1.0000	0.9897
Kernel method	Poly-2, w/o normalization, $\lambda = 10^{-1}$	1.0000	0.9897
Kernel method	Poly-2, w/o normalization, $\lambda = 1$	1.0000	0.9897
Kernel method	Poly-2, w/ normalization, $\lambda = 10^{-2}$	1.0000	0.9962
Kernel method	Poly-2, w/ normalization, $\lambda = 10^{-1}$	1.0000	0.9981
Kernel method	Poly-2, w/ normalization, $\lambda = 1$	0.9982	0.9981

TABLE XXXIII: Results of 5-fold CV with 5 different random seeds of the kernel method for the MNIST256 dataset (0 or 1).

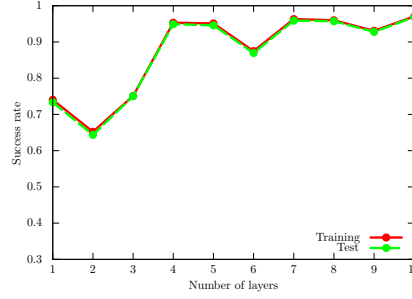


FIG. 83: Performance dependence of QCL on the number of layers L for the MNIST256 dataset (0 or 1). We use the CNOT-based circuit geometry and set $\theta_{\text{bias}} = 0$. We iterate the computation 100 times.

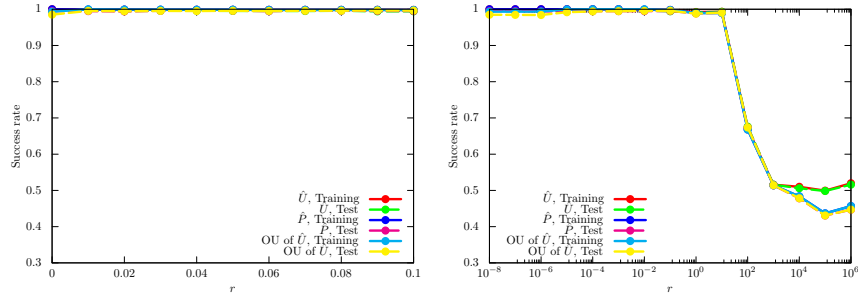


FIG. 84: Performance dependence of the UKM on r , which is the coefficient of the second term in the right-hand side of Eq. (J8) for the MNIST256 dataset (0 or 1). We use complex matrices and set $\theta_{\text{bias}} = 0$. We set $K = 20$ and $K' = 10$.

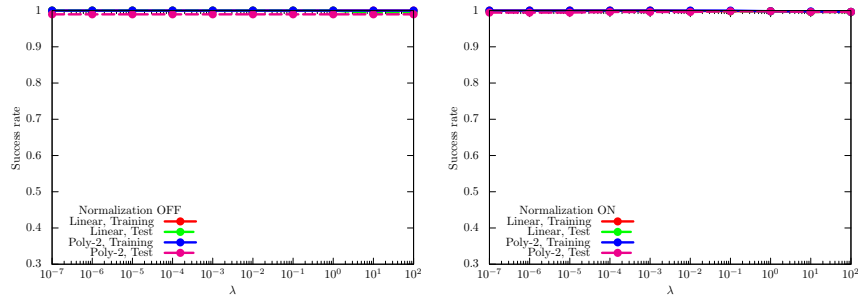


FIG. 85: Performance dependence of the kernel method on λ , which is the coefficient of the second term in the right-hand side of Eq. (G11) for the MNIST256 dataset (0 or 1). For $\phi(\cdot)$ in Eq. (G8), we use the linear functions and the second-degree polynomial functions with and without normalization.

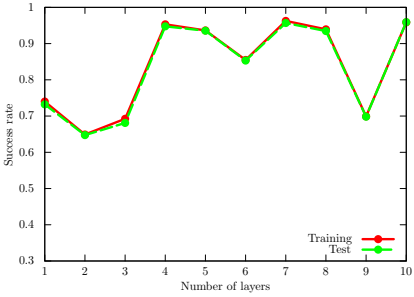


FIG. 86: Performance dependence of QCL on the number of layers L for the MNIST256 dataset (0 or 1) in the case of the hinge function, Eq. (F23). We use the CNOT-based circuit geometry and set $\theta_{\text{bias}} = 0$. We iterate the computation 300 times.

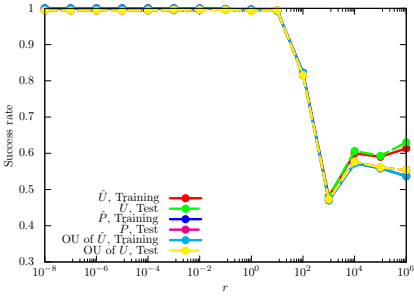


FIG. 87: Performance dependence of the UKM on r , which is the coefficient of the second term in the right-hand side of Eq. (J8) for the MNIST256 dataset (0 or 1) in the case of the hinge function, Eq. (F23). We use complex matrices and set $\theta_{\text{bias}} = 0$. We set $K = 30$ and $K' = 10$.

12. MNIST256 dataset (0 or non-0)

We here show the numerical result for the MNIST256 dataset (0 or non-0). For the UKM, we put $r = 0.010$ and set $K = 10$ and $K' = 5$ in Algo. 11. For QCL, we run iterations 50 times.

In Fig. 88, we show the numerical results of QCL for the 5-fold datasets with 5 different random seeds. In Fig. 89,

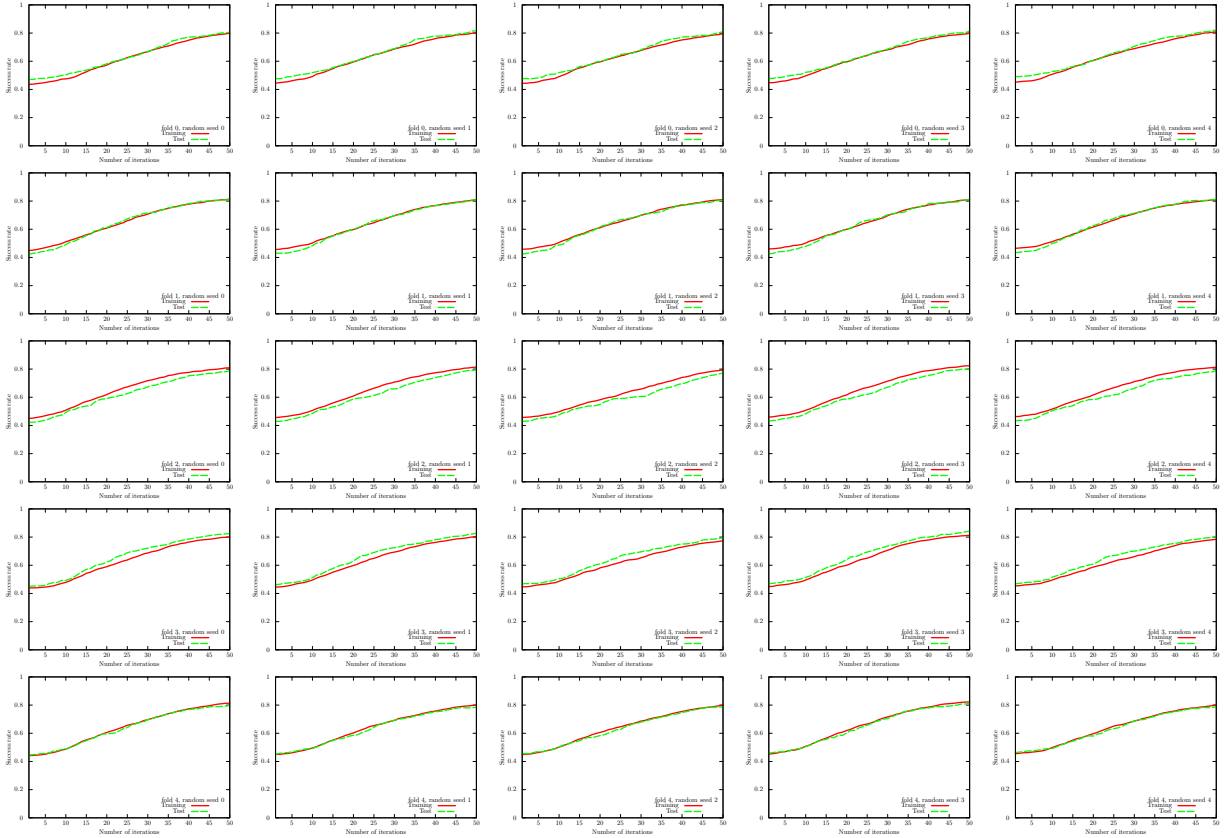


FIG. 88: Results of QCL on the 5-fold datasets with 5 different random seeds for the MNIST256 dataset (0 or non-0). We use the CNOT-based circuit and set $\theta_{\text{bias}} = 0$. The number of layers L is set to 5.

we show the numerical results of \hat{P} of the UKM for the 5-fold datasets with 5 different random seeds. In Fig. 90, we also show the numerical results of OU of \hat{X} of the UKM for the 5-fold datasets with 5 different random seeds.

We summarize the results of 5-fold CV with 5 different random seeds of QCL and the UKM in Tables XXXIV and XXXV, respectively. For QCL and the UKM, we select the best model for the training dataset over iterations to compute the performance. In Fig. 91, we plot the data shown in Tables XXXIV and XXXV. We also summarize the

Algo.	Condition	Training	Test
QCL	CNOT-based, w/o bias	0.8018	0.8006
QCL	CNOT-based, w/ bias	0.9053	0.9050
QCL	CRot-based, w/o bias	0.9010	0.9002
QCL	CRot-based, w/ bias	0.9053	0.9048

TABLE XXXIV: Results of 5-fold CV with 5 different random seeds of QCL for the MNIST256 dataset (0 or non-0). The number of layers L is 5 and the number of iterations is 50.

results of 5-fold CV with 5 different random seeds of the kernel method in Table XXXVI. More specifically, we use Ridge classification in Sec. G 2. We consider the linear functions and the second-order polynomial functions for $\phi(\cdot)$ in Eq. (G8) with and without normalization. We set $\lambda = 10^{-2}, 10^{-1}, 1$ where λ is the coefficient of the regularization term.

Next, we show the performance dependence of the three algorithms on their key parameters. We see the performance dependence of QCL on the number of layers L . The result is shown in Fig. 92. We then see the performance dependence

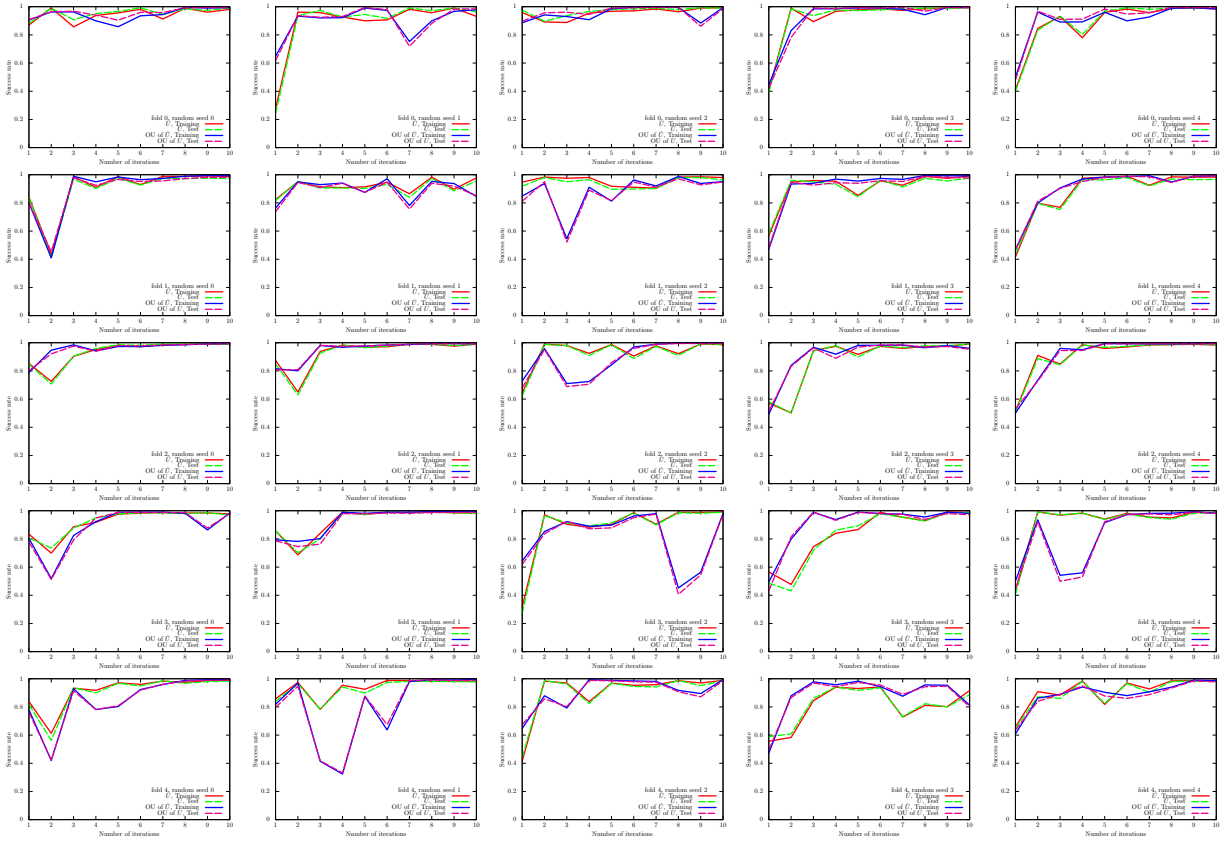


FIG. 89: Results of the UKM (\hat{X} and \hat{P}) on the 5-fold datasets with 5 different random seeds for the MNIST256 dataset (0 or non-0). We use complex matrices and set $\theta_{\text{bias}} = 0$. We set $r = 0.010$.

Algo.	Condition	Training	Test
UKM	\hat{X} , complex, w/o bias	0.9868	0.9829
UKM	\hat{P} , complex, w/o bias	0.9911	0.9870
UKM	OU of \hat{X} , complex, w/o bias	0.9915	0.9848
UKM	\hat{X} , complex, w/ bias	0.9902	0.9856
UKM	\hat{P} , complex, w/ bias	0.9238	0.9199
UKM	OU of \hat{X} , complex, w/ bias	0.9264	0.9244
UKM	\hat{X} , real, w/o bias	0.9886	0.9836
UKM	\hat{P} , real, w/o bias	0.9922	0.9871
UKM	OU of \hat{X} , real, w/o bias	0.9927	0.9889
UKM	\hat{X} , real, w/ bias	0.9894	0.9859
UKM	\hat{P} , real, w/ bias	0.9213	0.9188
UKM	OU of \hat{X} , real, w/ bias	0.9208	0.9205

TABLE XXXV: Results of 5-fold CV with 5 different random seeds of the UKM for the MNIST256 dataset (0 or non-0). We put $r = 0.010$ and set $K = 10$ and $K' = 5$.

of the UKM on r , which is the coefficient of the second term in the right-hand side of Eq. (J8). The result is shown in Fig. 93. In Fig. 94, we show the performance dependence of the kernel method on λ , which is the coefficient of the second term in the right-hand side of Eq. (G11).

So far, we have used the squared error function, Eq. (F22). In Fig. 95, we show the performance dependence of QCL on the number of layers L in the case of the hinge function, Eq. (F23). In Fig. 96, we show the performance dependence of the UKM on r , which is the coefficient of the second term in the right-hand side of Eq. (J8), in the case of the hinge function, Eq. (F23).

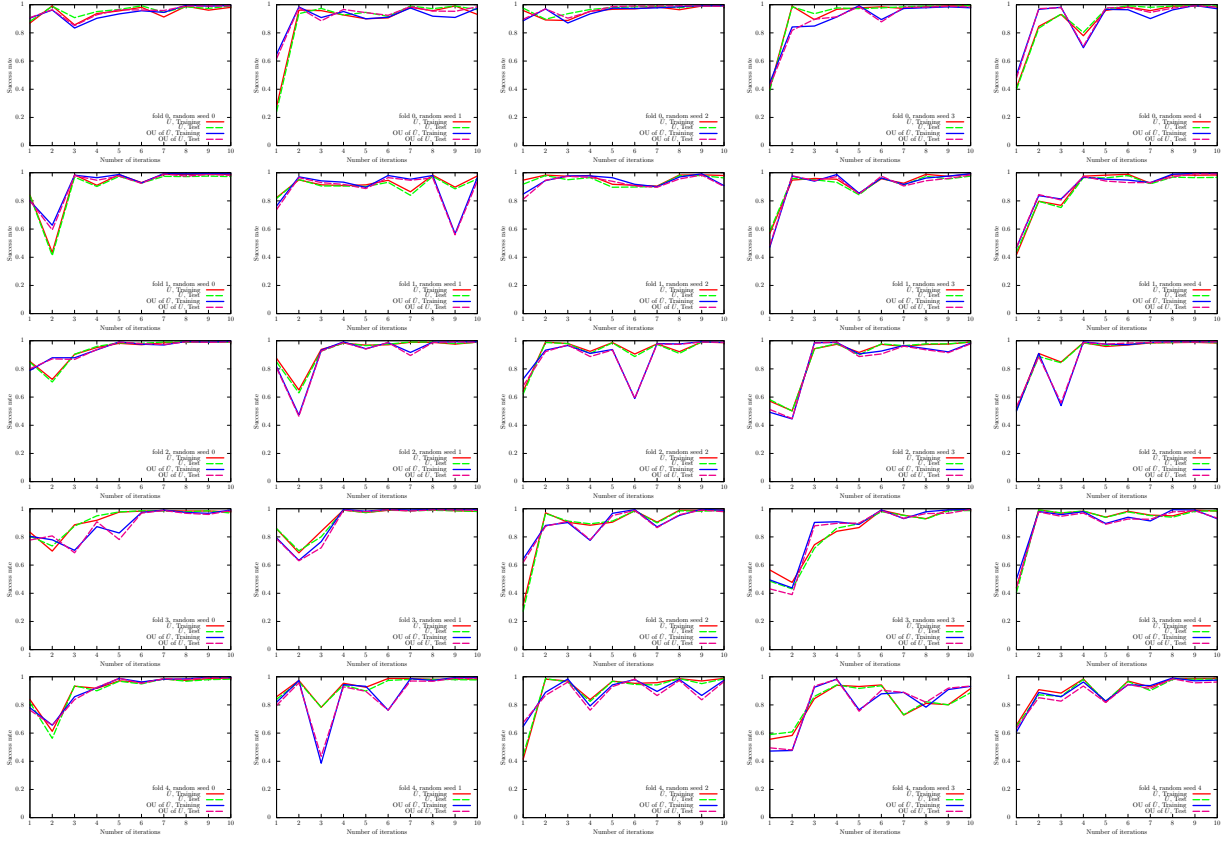


FIG. 90: Results of the UKM (\hat{X} and OU of \hat{X}) on the 5-fold datasets with 5 different random seeds for the MNIST256 dataset (0 or non-0). We use complex matrices and set $\theta_{\text{bias}} = 0$. We set $r = 0.010$.

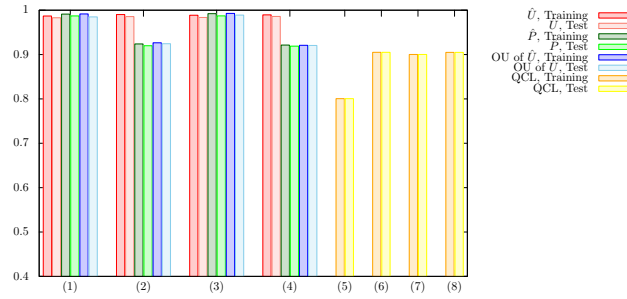


FIG. 91: Results of 5-fold CV with 5 different random seeds for the MNIST256 dataset (0 or non-0). For the UKM, we put $r = 0.010$ and set $K = 10$ and $K' = 5$. For QCL, the number of layers L is 5 and the number of iterations is 50. The numerical settings are as follows: (1) complex matrices without the bias term, (2) complex matrices with the bias term, (3) real matrices without the bias term, (4) real matrices with the bias term, (5) CNOT-based circuit without the bias term, (6) CNOT-based circuit with the bias term, (7) CRot-based circuit without the bias term, (8) CRot-based circuit with the bias term, (9) 1d Heisenberg circuit without the bias term, (10) 1d Heisenberg circuit with the bias term, (11) FC Heisenberg circuit without the bias term, and (12) FC Heisenberg circuit with the bias term.

Algo.	Condition	Training	Test
Kernel method	Linear, w/o normalization, $\lambda = 10^{-2}$	0.9963	0.9921
Kernel method	Linear, w/o normalization, $\lambda = 10^{-1}$	0.9963	0.9921
Kernel method	Linear, w/o normalization, $\lambda = 1$	0.9963	0.9921
Kernel method	Linear, w/ normalization, $\lambda = 10^{-2}$	0.9893	0.98189
Kernel method	Linear, w/ normalization, $\lambda = 10^{-1}$	0.9856	0.9792
Kernel method	Linear, w/ normalization, $\lambda = 1$	0.9843	0.9787
Kernel method	Poly-2, w/o normalization, $\lambda = 10^{-2}$	1.0000	0.9906
Kernel method	Poly-2, w/o normalization, $\lambda = 10^{-1}$	1.0000	0.9906
Kernel method	Poly-2, w/o normalization, $\lambda = 1$	1.0000	0.9906
Kernel method	Poly-2, w/ normalization, $\lambda = 10^{-2}$	0.9997	0.9949
Kernel method	Poly-2, w/ normalization, $\lambda = 10^{-1}$	0.9992	0.9953
Kernel method	Poly-2, w/ normalization, $\lambda = 1$	0.9946	0.9916

TABLE XXXVI: Results of 5-fold CV with 5 different random seeds of the kernel method for the MNIST256 dataset (0 or non-0).

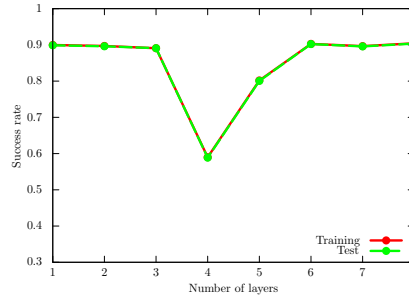


FIG. 92: Performance dependence of QCL on the number of layers L for the MNIST256 dataset (0 or non-0). We use the CNOT-based circuit geometry and set $\theta_{\text{bias}} = 0$. We iterate the computation 50 times.

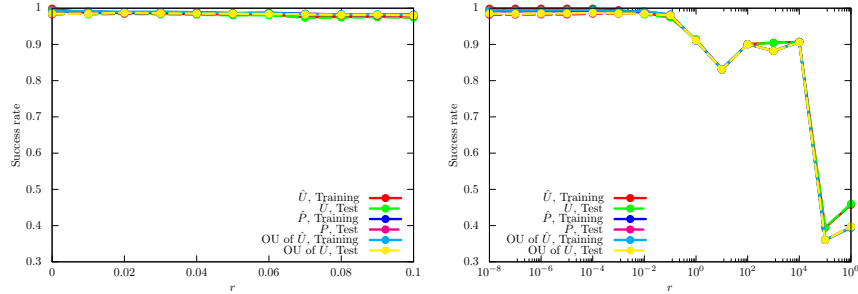


FIG. 93: Performance dependence of the UKM on r , which is the coefficient of the second term in the right-hand side of Eq. (J8) for the MNIST256 dataset (0 or non-0). We use complex matrices and set $\theta_{\text{bias}} = 0$. We set $K = 10$ and $K' = 5$.

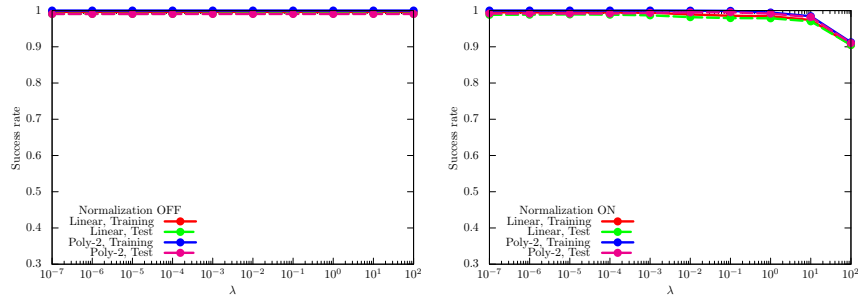


FIG. 94: Performance dependence of the kernel method on λ , which is the coefficient of the second term in the right-hand side of Eq. (G11) for the MNIST256 dataset (0 or non-0). For $\phi(\cdot)$ in Eq. (G8), we use the linear functions and the second-degree polynomial functions with and without normalization.

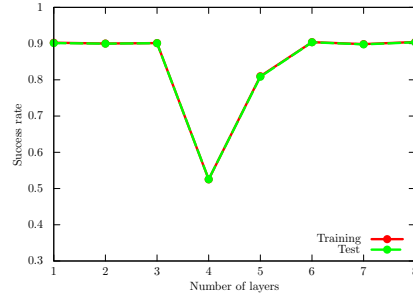


FIG. 95: Performance dependence of QCL on the number of layers L for the MNIST256 dataset (0 or non-0) in the case of the hinge function, Eq. (F23). We use the CNOT-based circuit geometry and set $\theta_{\text{bias}} = 0$. We iterate the computation 300 times.

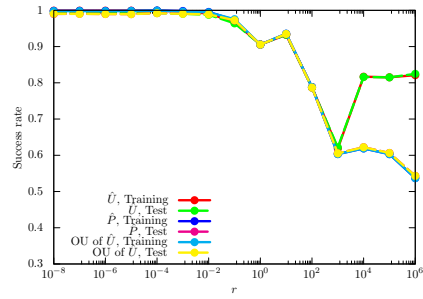


FIG. 96: Performance dependence of the UKM on r , which is the coefficient of the second term in the right-hand side of Eq. (J8) for the MNIST256 dataset (0 or non-0) in the case of the hinge function, Eq. (F23). We use complex matrices and set $\theta_{\text{bias}} = 0$. We set $K = 30$ and $K' = 10$.

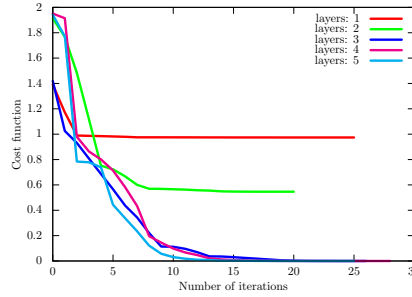


FIG. 97: Values of the cost function $\mathcal{J}_{\text{cost}}(\theta, \lambda; L, 2, \hat{U})$, Eq. (K6) with $p = 2$, for the iris dataset (1 or non-1).

13. Discussions

In the main text, we give the discussions on the numerical results. The results shown in this section are basically consistent with the results shown in the main text and support the statement.

Appendix M: Numerical simulation of the VCR

In this section, we show numerical simulation on the VCR. For $\hat{U}_c(\theta)$, we use the CNOT-based circuit geometry (F9).

1. Numerical setting

In this section, we use Eq. (K6) with $p = 2$ as the optimization function of the VCR. For $\hat{U}_c(\theta)$, we use the CNOT-based circuit.

2. Datasets

In this section, we consider the iris dataset (1 or non-1), the cancer dataset (0 or 1), and the wine dataset (0 or non-0) described in Sec. L2. Refer to Sec. L2 for the details.

3. Iris dataset (1 or non-1)

Let us consider the iris dataset (1 or non-1) and minimizing Eq. (K6) with $p = 2$. As \hat{U} , we use \hat{P} computed by the UKM under the condition of real matrices, $r = 0.010$, and $\theta_b = 0$ that gives the success rate for the training dataset 0.7565 and that for the test dataset 0.8286. In Fig. 97, we show the values of the cost function $\mathcal{J}_{\text{cost}}(\theta, \lambda; L, 2, \hat{U})$, Eq. (K6) with $p = 2$. We vary the number of layers L . In Table XXXVII, we summarize the performance of the input unitary operator, QCL, and the circuit geometry computed by the VCR. We have $L_{0.001} = 3$.

4. Cancer dataset (0 or 1)

Let us consider the cancer dataset (0 or 1) and minimizing Eq. (K6) with $p = 2$. As \hat{U} , we use \hat{P} computed by the UKM under the condition of real matrices, $r = 0.010$, and $\theta_b = 0$ that gives the success rate for the training dataset 0.9139 and that for the test dataset 0.9483. In Fig. 98, we show the values of the cost function $\mathcal{J}_{\text{cost}}(\theta, \lambda; L, 2, \hat{U})$, Eq. (K6) with $p = 2$. We vary the number of layers L . In Table XXXVIII, we summarize the performance of the input unitary operator, QCL, and the circuit geometry computed by the VCR. We have $L_{0.001} = 80$.

Algo.	Condition	Cost	Training	Test
Input UKM, \hat{P} , real, w/o bias		—	0.7565	0.8286
VCR	# of layers: 1	0.9740	0.3565	0.2571
VCR	# of layers: 2	0.5465	0.3565	0.2571
VCR	# of layers: 3	0.0000	0.7565	0.8286
VCR	# of layers: 4	0.0000	0.7565	0.8286
VCR	# of layers: 5	0.0000	0.7565	0.8286
UKM	\hat{P} , real, w/o bias	—	0.7880	0.7789
QCL	# of layers: 5	—	0.6851	0.5845

TABLE XXXVII: Performance of the VCR for the iris dataset (1 or non-1). We show the success rates for the training and test datasets and the values of the cost function $\mathcal{J}_{\text{cost}}(\theta, \lambda; L, 2, \hat{U})$, Eq. (K6) with $p = 2$. The input for the VCR is \hat{P} created by the UKM under the condition of real matrices, $r = 0.010$, and $\theta_b = 0$. For reference, we add the last two rows that show the results of 5-fold CV.

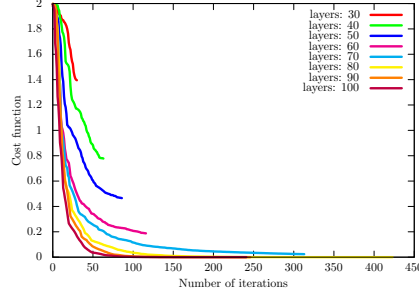


FIG. 98: Values of the cost function $\mathcal{J}_{\text{cost}}(\theta, \lambda; L, 2, \hat{U})$, Eq. (K6) with $p = 2$, for the cancer dataset (0 or 1).

5. Wine dataset (0 or non-0)

Let us consider the wine dataset (0 or non-0) and minimizing Eq. (K6) with $p = 2$. As \hat{U} , we use \hat{P} computed by the UKM under the condition of real matrices, $r = 0.010$, and $\theta_b = 0$ that gives the success rate for the training dataset 0.9179 and that for the test dataset 0.9091. In Fig. 99, we show the values of the cost function $\mathcal{J}_{\text{cost}}(\theta, \lambda; L, 2, \hat{U})$, Eq. (K6) with $p = 2$. We vary the number of layers L . In Table XXXIX, we summarize the performance of the input unitary operator, QCL, and the circuit geometry computed by the VCR. We have $L_{0.001} = 25$.

Algo.	Condition	Cost	Training	Test
Input UKM, \hat{P} , real, w/o bias		—	0.9139	0.9483
VCR	# of layers: 10	1.9694	0.3929	0.2931
VCR	# of layers: 20	1.9734	0.6071	0.7069
VCR	# of layers: 30	1.3950	0.6071	0.7069
VCR	# of layers: 40	0.7777	0.6909	0.7586
VCR	# of layers: 50	0.4657	0.8499	0.9224
VCR	# of layers: 60	0.1877	0.9073	0.9483
VCR	# of layers: 70	0.0236	0.9073	0.9483
VCR	# of layers: 80	0.0000	0.9139	0.9483
VCR	# of layers: 90	0.0000	0.9139	0.9483
VCR	# of layers: 100	0.0000	0.9139	0.9483
UKM	\hat{P} , real, w/o bias	—	0.9194	0.9131
QCL	# of layers: 5	—	0.8798	0.8768
QCL	# of layers: 10	—	0.7814	0.7767

TABLE XXXVIII: Performance of the VCR for the cancer dataset (0 or 1). We show the success rates for the training and test datasets and the values of the cost function $\mathcal{J}_{\text{cost}}(\theta, \lambda; L, 2, \hat{U})$, Eq. (K6) with $p = 2$. The input for the VCR is \hat{P} created by the UKM under the condition of real matrices, $r = 0.010$, and $\theta_b = 0$. For reference, we add the last three rows that show the results of 5-fold CV.

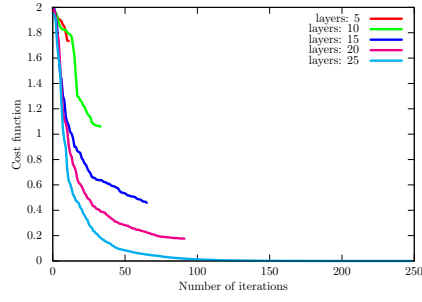


FIG. 99: Values of the cost function $\mathcal{J}_{\text{cost}}(\theta, \lambda; L, 2, \hat{U})$, Eq. (K6) with $p = 2$, for the wine dataset (0 or non-0).

Algo.	Condition	Cost	Training	Test
Input	UKM, \hat{P} , real, w/o bias	—	0.9179	0.9091
VCR	# of layers: 5	1.7343	0.6642	0.6818
VCR	# of layers: 10	1.0591	0.4254	0.4091
VCR	# of layers: 15	0.4588	0.6791	0.7045
VCR	# of layers: 20	0.1765	0.7836	0.8864
VCR	# of layers: 25	0.0000	0.9179	0.9091
UKM	\hat{P} , real, w/o bias	—	0.9200	0.9185
QCL	# of layers: 5	—	0.9057	0.9052

TABLE XXXIX: Performance of the VCR for the wine dataset (0 or non-0). We show the success rates for the training and test datasets and the values of the cost function $\mathcal{J}_{\text{cost}}(\theta, \lambda; L, 2, \hat{U})$, Eq. (K6) with $p = 2$. The input for the VCR is \hat{P} created by the UKM under the condition of real matrices, $r = 0.010$, and $\theta_b = 0$. For reference, we add the last two rows that show the results of 5-fold CV.

6. Discussions

The discussions on the VCR is given in the main text. In this section, we give the results of the VCR on three different datasets: the iris dataset (1 or non-1), the cancer dataset (0 or 1), and the wine dataset (0 or non-0). The results shown in this section support the statement in the main text.

Appendix N: Conclusion

In the SI, we have provided supplemental information on "Ansatz-Independent Variational Quantum Classifier."